TECHNISCHE UNIVERSITÄT MÜNCHEN

TUM School of Engineering and Design

High Fidelity Modeling and Simulations for Uncertainty Quantification and Risk-averse Optimization of Structures Under Natural Wind Conditions

Anoop Kodakkal

Vollständiger Abdruck der von der TUM School of Engineering and Design der Technischen Universität München zur Erlangung eines

Doktors der Ingenieurwissenschaften (Dr.-Ing.)

genehmigten Dissertation.

Vorsitz:

Prof. Dr.-Ing. habil. Fabian Duddeck

Prüfende der Dissertation:

1. Prof. Dr.-Ing. Kai-Uwe Bletzinger
2. Jun.-Prof. Dr.-Ing. Ulrich Römer
3. Prof. Dr.-Ing. habil. Roland Wüchner

Die Dissertation wurde am 28.04.2023 bei der Technischen Universität München eingereicht und durch die TUM School of Engineering and Design am 29.01.2024 angenommen.

Schriftenreihe des Lehrstuhls für Statik
TU München

Band 62

Anoop Kodakkal

High Fidelity Modeling and Simulations for Uncertainty Quantification and Risk-averse Optimization of Structures Under Natural Wind Conditions

München 2024

Veröffentlicht durch

Kai-Uwe Bletzinger
Lehrstuhl für Statik
Technische Universität München
Arcisstr. 21
80333 München

Telefon: +49(0)89 289 22422
Telefax: +49(0)89 289 22421
E-Mail: kub@tum.de
Internet: www.cee.ed.tum.de/st/startseite/

ISBN: 978-3-943683-73-8

Abstract

Recent developments in computational wind engineering, numerical methods, and high-performance computing have matured to model and compute wind effects on structures accurately and efficiently. However, modeling real-world problems is always associated with uncertainties, and an engineering decision-maker must be aware of and consider these uncertainties. In this context, this thesis explores uncertainty quantification (UQ) and optimization under uncertainty (OUU) for uncertain structures under uncertain wind conditions.

The uncertainties of the wind parameters, wind direction, and the inherent randomness of the wind flow are considered in the uncertainty quantification problem. The uncertain damping and eigen frequency of the structure are also modeled in the UQ analysis. The uncertainty propagation is investigated by Polynomial Chaos, Monte Carlo, Multi-level Monte Carlo, and Neural network surrogates. The efficacy of the methods is demonstrated and compared for the practical computational wind engineering problem.The UQ workflow is demonstrated for the benchmark Commonwealth Advisory Aeronautical Council (CAARC) building B under uncertain wind conditions. Conditional value at risk (CVaR) as a risk measure is introduced and proposed as a superior measure for decision-making under uncertainties of wind flow. The thesis also demonstrates the benefit of CVaR for design selection of tall buildings.

Aerodynamic shape modification is a common strategy to reduce the wind effects on tall buildings. This thesis proposes a novel approach to risk-averse shape optimization of tall buildings that incorporates location-specific uncertainties in wind conditions. The bending moment of the building is minimized, resulting in a building with lower construction and maintenance costs, lower material use, and a reduced carbon footprint. CVaR of the quantity of interest (QoI) is minimized for the high-consequence events in the worst 10% of the wind conditions. A gradient-based optimization pipeline with an adaptive sampling strategy to reduce computational cost is proposed. The improved performance of the final risk-averse building demonstrates the significance of the novel risk-averse design workflow. By performing UQ and OUU tasks for structures under uncertain wind conditions, a safer and superior-performing structure in the real world is achieved.

Zusammenfassung

Die jüngsten Entwicklungen im Bereich des computergestützten Windingenieurwesens, der numerischen Methoden und des Hochleistungsrechnens erlauben es, Windwirkungen auf Strukturen realitätsnäher und effizient zu modellieren und zu berechnen. Die Modellierung von realen Problemen ist jedoch immer mit Unsicherheiten verbunden, und ein technischer Entscheidungsträger muss sich dieser Unsicherheiten bewusst sein und sie berücksichtigen. In diesem Zusammenhang untersucht und entwickelt diese Arbeit Methoden zur Unsicherheitsquantifizierung (UQ) und zur Optimierung unter Unsicherheit (OUU) für windbelastete Strukturen unter Berücksichtigung der für das Problem charakteristischen unsicheren Parameter.

Die Unsicherheiten der Windparameter, der Windrichtung und die inhärente Zufälligkeit der Windströmung werden in dem Unsicherheitsquantifizierungsproblem berücksichtigt. Die unsichere Dämpfung und Eigenfrequenz der Struktur werden ebenfalls in der UQ-Analyse modelliert. Die Unsicherheitsübertragung wird mit Hilfe von Polynomial Chaos, Monte Carlo, Multi-level Monte Carlo und Neural Network Surrogates untersucht. Die Wirksamkeit der Methoden wird für ein praktisches Problem im Windingenieurwesen demonstriert und verglichen. Der vorgeschlagene UQ-Arbeitsablauf wird für das Referenzgebäude CAARC unter unsicheren Windbedingungen demonstriert. Der Conditional Value at Risk (CVaR) wird als Risikomaß eingeführt und als überlegenes Maß für die Entscheidungsfindung bei unsicheren Windverhältnissen vorgeschlagen. In dieser Arbeit wird auch eine Studie vorgestellt, die den Nutzen des Conditional Value at Risk für die Entwurfsauswahl demonstriert.

Die Veränderung der aerodynamischen Form ist eine gängige Strategie zur Verringerung der Windauswirkungen auf hohe Gebäude. In dieser Arbeit wird ein neuartiger Ansatz zur risikoaversen Formoptimierung von hohen Gebäuden vorgeschlagen, der standortspezifische Unsicherheiten bei den Windbedingungen berücksichtigt. Das Biegemoment des Gebäudes wird minimiert, was zu einem Gebäude mit geringeren Bau- und Instandhaltungskosten, einem geringeren Materialverbrauch, einer besseren CO2-Bilanz und einem höheren Komfort für die Bewohner führt. Der bedingte Risikowert der interessierenden Größe (Quantity of Interest, QoI) wird für die folgenschweren Ereignisse unter den schlechtesten 10% der Windbedingungen minimiert.

In dieser Arbeit wird eine gradientenbasierte Optimierungsmethodik mit einer adaptiven Sampling-Strategie vorgeschlagen, um den Berechnungsaufwand zu reduzieren. Die verbesserte Performanz des final resultierenden risikoaversen Gebäudes demonstriert die Leistungsfähigkeit des neuartigen risikoaversen Entwurfsprozesses. Durch die Umsetzung von UQ- und OUU-Prozeduren für Bauwerke unter unsicheren Windbedingungen wird ein sichereres und leistungsfähigeres Bauwerk in der realen Welt erreicht.

Dedicated to my parents

Acknowledgments

Throughout this dissertation, I have received enormous support and assistance from a number of wonderful people and organizations, and I would like to express my gratitude toward each one of them. I want to extend my heartfelt appreciation to my supervisor Prof. Dr.-Ing. Kai-Uwe Bletzinger for his expertise, friendly discussions, and hosting me at his chair of structural analysis. I would also like to thank Prof. Dr.-Ing. habil. Roland Wüchner for the fruitful discussions and constructive feedback during various stages of my dissertation. The help of these two professors was invaluable in sharpening and widening my thinking. I am grateful to Prof. Vasant Matsagar for his help and support before the start of my thesis.

I would also like to thank my colleagues Andreas Apostalatos, Aditya Ghandasala, Michael Andre, Rishith Ellath Meethal, and Máté Péntak for the productive collaboration. I extend my gratitude to Prof. Brendan Keith and Prof. Dr. Barbara Wohlmuth for their extensive help with the OUU tasks. I want to convey my gratitude to Deutscher Akademischer Austauschdienst (DAAD) for the funding support. I would like to voice my appreciation to the European Union (EU) for funding the ExaQUte project and the computational resources provided.

I would like to thank the teachers from PAUPS, AVSGHSS, NITC and IITD who have knowingly or unknowingly contributed to developing my abilities as a scientist.

I owe a debt of gratitude to my partner, Amore, Dr. rer. nat. Vidya Padmanabhan Nair, whose support, love, and encouragement have been invaluable through various stages of my Ph.D. I am grateful to my sister, aliyan, and Adwait, who have been there for me. I can not thank my parents enough for all they have done for my education and professional success throughout the past three decades. I thank members of JGM for making my life in Munich a delight. I would also like to express my gratitude to my buddies in Munich - Luttu, 6μ, Sebu, Ponnu, Marar, Rishi, and Pranav (in no specific order), without whom I could have finished this thesis as well. I would also like to thank the support from my friends Archith, Naseef, Nikhil, Nikhiljith, Nitasha and Shibu, to name a few. I would also like to thank my students for their discussions and help. To all those who have helped me along the way, I extend my heartfelt appreciation.

Anoop Kodakkal

CONTENTS

In theory, there's no difference between theory and practice. But in practice, there is

Benjamin Brewster

CHAPTER 1

INTRODUCTION

Structures in civil engineering are conceptualized, analyzed, designed, and built from the results and predictions of computational models in recent decades. In structural engineering practice, it so happens that the structure to be designed is unique, and no information or measurement data is available about the responses of structures under dynamic loads, such as wind loads, during the analysis and design phase. In some cases, the situation continues even after constructing the structure. This scenario is unlike machine components or other design scenarios, where multiple entities of the same structure will be manufactured. An approach followed in structural wind engineering practice is performing scaled-down testing. The scaled-down test results may be associated with measurement and modeling errors. A full-scale test is impossible prior to the construction of the structure. This forces structural engineers and researchers to rely more on computational modeling.

Equally crucial to modeling structural behavior is load modeling. It is vital to estimate the load scenarios that may happen in the lifetime of the structure to make a realistic and reliable prediction of responses.

When it comes to simulating and predicting real-world behavior, nothing is uncertainty-free. Structural analysis and design are no exception since they involve structures built by humans and acted upon by a variety of actions that are natural and/or man-made. Both natural and man-made actions on structures (not yet built) are not known with certainty during the analysis and design phase.

What precautions and considerations are needed if some of the parameters of computational models are not known with certainty? This thesis primarily explores this question in the context of structures subjected to wind loads.

1.1 Background

The design of structures is realized in practice by obeying the design codes. In modern design codes, such as the Euro code [1], a reliability-based approach is adopted. The codes estimate and try to minimize the uncertainties through safety factors. Uncertainties in the loading are considered in the design codes by considering a load factor (> 1). The value of the load factor is higher for load cases with more significant variability. This is the reason for having a low load factor for dead load compared to wind or earthquake loads in load combinations in design codes. Similarly, the calculated strength of structure is divided by a factor for resistance (< 1). Considering the uncertainty of the material properties and the connections, the factors of resistance are determined. The resistance factor is low for materials with larger variability and is closer to 1 for materials with lower variation and higher quality control. Hence, a higher resistance factor for steel and a lower resistance factor for concrete in design codes is adopted. The considerations of uncertainty and variability are done in the codes in the background, and an intelligent user should be aware of the consideration given to the variability and these hidden considerations.

The lack of such understanding may lead to the collapse of structures due to underestimating unfortunate events of enormous wind, snow, earthquakes, etc., or by overestimating the strength of a given structure. Figure 1.1 shows some failures due to structural mishaps in the past. Many of these catastrophic events could have been prevented with a better understanding of structural behaviors. These unfortunate events may lead to immense economic loss or irreplaceable loss of human lives. It is the re-

Figure 1.1 : Structural failures have had catastrophic consequences in the past, such as Collapse of the Tacoma Narrow Bridge [2] (left); the tragic collapse of a walkway at the Hyatt Regency in Kansas City in 1981, causing human casualties [3] (middle); and the failure of AquaDom aquarium at hotel Radisson in Berlin 2022 causing around 1500 aquatic life casualties [4] (right).

sponsibility of a structural engineer to be aware of such risks and minimize errors, including uncertainty in the analysis and design.

The considerations of variability or lack of certainty in load and strength become exceedingly crucial for structures where exact code recommendations are not available. For example, in the case of structures with a height of more than 250m, Euro Code [1] recommendations for wind are not well defined. When the geometry of the building is of unusual shape due to architectural requirements, the drag coefficient values, dynamic factors ($C_s.C_d$), etc., may not be available in the design codes. It is the responsibility of the design engineer to make realistic design decisions in these cases.

1.2 Motivation

With increasing storm events and changing climate due to human interference, the importance of wind effects on structures is of great concern in recent times [5]. Traditionally, wind tunnels and reduced scale testing are employed to understand the wind effects on structures [6]. Complementary to these traditional approaches, Computational Wind Engineering (CWE) has gained attention in application to flow problems, including structural wind engineering, in the past 50 years [6]. This has shifted the attention of researchers from the traditional approach of wind tunnels. Numerical wind tunnels based on CWE offer various advantages over traditional wind tunnels and have been employed in various studies [7–10]. CWE may be de-

fined as the use of computational approaches, specifically Computational Fluid Dynamcis (CFD) for wind engineering applications. The basic idea of CWE is to determine the velocity and pressure fields around the building and further analysis of the same. There have been several studies that utilized CWE tools to determine the pressure and velocity fields around the structure [11–15]. Even though huge advancements are happening in CWE, the simulation using CWE tools for the wind effects of structures still faces challenges. Murakami et al. [9] indicates these challenges to include the high Reynolds number in wind engineering application, complex 3D flow around the structure, numerical issues associated with sharp corners, and the challenges associated with inlet and outlet boundary conditions. These challenges are tackled with domain expertise and are an active research area. Wind effects on structures have been studied and applied in various studies to include in structural wind engineering [16–24]. Also, CWE has been used for other domains like wind energy [25–27], and pedestrian comfort around buildings [28–31]. To gain confidence in the CWE model, verification and validation are imperative to simulations for wind effects on the structure. Code verification and solution verification is also required for CFD solver [32]. Wind tunnel results are used to validate the CWE results in practice.

Structures subjected to wind undergo complex interactions and require in-depth analysis. This is particularly true for the case of flexible structures such as tall buildings or long-span bridges. It is well known that a fully coupled fluid-structure interaction analysis is needed for such problems. Here, the analysis considers the mutual interaction between the structure and the fluid flow around the structure. Such a coupled analysis is of great importance in estimating the accurate structural effects of wind loading. There are a couple of recent studies [33, 34] that indicate the algorithms and methodologies for wind structure interaction. The field broadly is termed Structural Wind Engineering (SWE).

Like other engineering disciplines, structural wind engineering practice also follows a deterministic approach to analysis and design. However, real-world structural wind engineering problems have many uncertainties associated with them, and deterministic models alone are not sufficient for making predictions under these uncertainties. Wind flow at a given location itself is uncertain inherently. A computational model of the structure that takes into account the uncertainties from various sources can provide

deeper insight into the structural response and make reliable predictions of Quantities of Interest (QoI). The uncertainties of the QoI are evaluated from the uncertainties of the inputs in the forward propagation of uncertainty. This is also known as the push-forward problem. The known uncertainties of the inputs are forward propagated through the model to obtain the uncertainties of the output QoI [35]. Hence, forward uncertainty propagation is fundamental in structural wind engineering problems with inherent uncertainties.

The stochastic model provides a better understanding of physics and provides a reliable prediction with quantified uncertainties in these cases. This thesis aims to include the various uncertainties from wind and structure and then determine the quantified uncertainties of the structural responses. When this uncertain wind is acted upon a structure with uncertain material parameters, the QoI is stochastic and needs additional considerations that are not present in CWE. These additional considerations to CWE are referred to in this thesis as Stochastic Computational Wind Engineering (SCWE). In SCWE, the uncertainties arising in CWE from various sources are accounted for. The motivation of the thesis is to incorporate the rich knowledge of UQ to CWE and enrich SCWE insights.

1.3 An Introduction to Stochastic Computational Wind Engineering

Structural wind engineering deals with analyzing structural responses, safety and serviceability evaluations, and control of structures subjected to wind loads. The QoI are the internal forces, deformations, accelerations, or any other quantities that are relevant for engineering decision making. As explained earlier, wind at a location itself is stochastic and time-varying. Stochastic computational wind engineering insight is required in these cases.

For example, one apparent randomness to be considered when analyzing a structure subjected to the wind is the wind turbulence at the atmospheric boundary layer. It can be observed that the wind speed recorded at the exact location but at different time intervals shows different characteristics. However, the statistics of a large number of such wind data at a location over a considerable duration show some stable probabilistic characteristics, as shown in Figure 1.2.

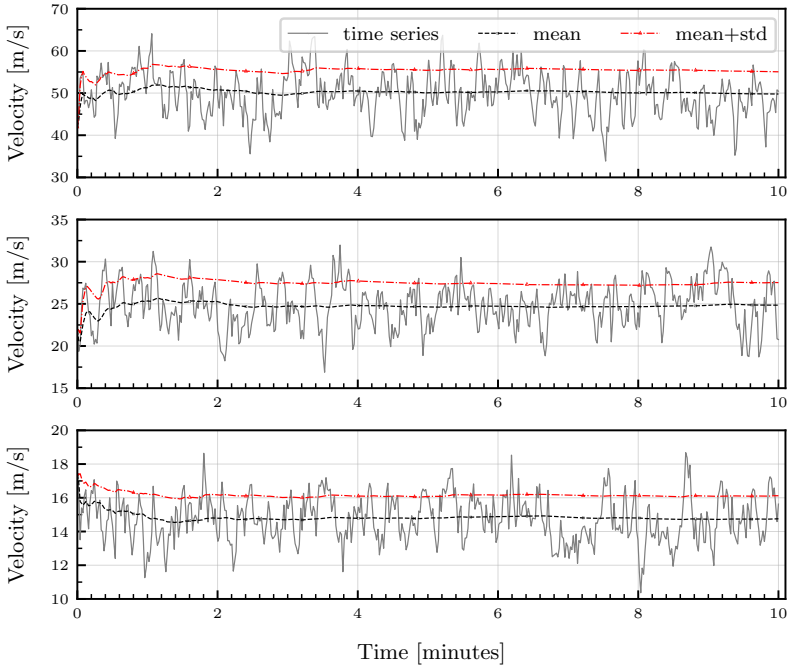

Figure 1.2 : Time series of wind velocities at three heights(increasing from bottom to top) with mean and standard deviation evolution over time is shown. The statistics are observed to converge over time.

1.3.1 Quantifying sources of uncertainty for stochastic computational wind engineering

Uncertainty can be classified as aleatory and epistemic depending upon its characteristics. Epistemic are reducible uncertainty, whereas aleatoric uncertainties are irreducible and are inherent to the system considered [35].

The Figure 1.3 represents the matrix of knowledge adapted from [36]. Here, the different aspects of uncertainty are depicted for an SCWE scenario. The matrix of knowledge is divided into four quadrants. It includes a fully deterministic simulation, either aleatoric or epistemic uncertainty, and

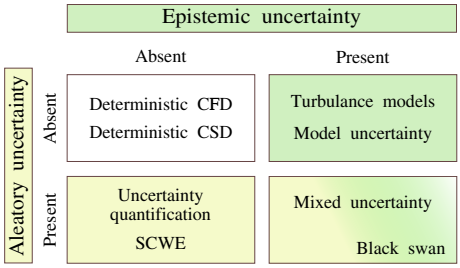

Figure 1.3 : The matrix of knowledge - a visualization of the interrelation between different types of uncertainties in the context of wind effects on structure adapted from [36].

the field known as Black swan events. In CWE, a deterministic simulation is used as all the information about the numerical model is known. This is true for cases where the geometry, boundary conditions, and properties of the fluid are known with certainty. Model uncertainty is also ignored when a fixed fidelity of the model is used to approximate the solution of a Partial Differential Equation (PDE). A fixed numerical scheme is used to solve the problem in that case. A deterministic CWE simulation is where the epistemic and aleatoric uncertainty are known fully, assumed to be known fully, or just ignored.

Epistemic uncertainty is reducible. A typical example of this category is turbulence. This type of uncertainty can be reduced entirely by doing a Direct Numerical Simulation (DNS) where the turbulence is resolved numerically. However, for other simulations, this source of uncertainty exists. Model uncertainty falls in this category. It can be reduced by adopting a high-fidelity model.

Aleatoric uncertainty is inherent and can not be reduced. For example, the wind loading acting on the structure is inherently stochastic. This can be characterized by probabilistic definitions, such as a random variable. The fourth quadrant represents the situation where the epistemic and aleatoric uncertainties are not known with complete certainty. Moreover, a high-risk, low-probability event may probably happen in this case. These are termed as Black swan events.

This thesis mainly focuses on the aleatoric uncertainties of wind loading on uncertain structures as they are of prime importance to SCWE applications.

1.3.2 Stochastic wind load chain

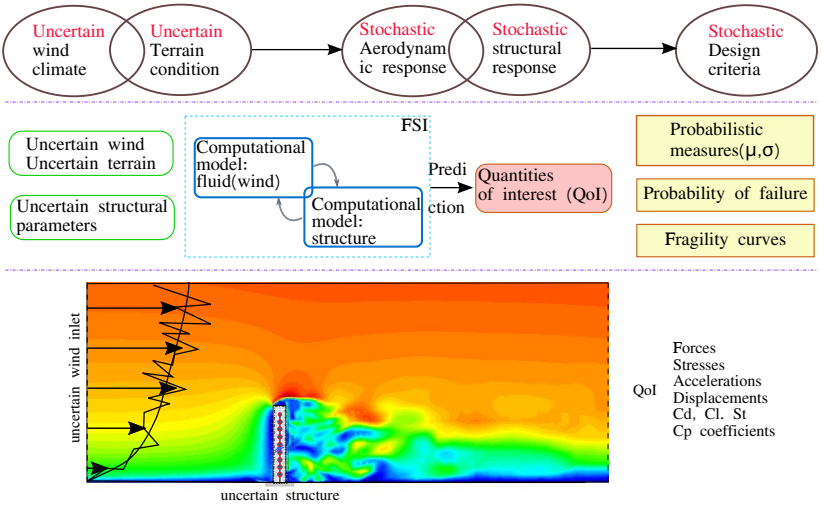

Figure 1.4 : Stochastic wind load chain - Davenport wind load chain is enriched with UQ knowledge to result in the stochastic wind load chain.

Figure 1.4 represents how the well-known Davenport wind load chain can be enriched with uncertainties considered in the inputs. The workflow starts with the uncertain input wind parameters as well as uncertain input structural parameters. This will result in an uncertain aeroelastic response of the structures. Now, the design criteria also need to be in the stochastic domain. This stochastic workflow serves as a basis for the analysis procedure followed in this study.

1.4 Objective and Contributions

The main objectives and contributions of the thesis are listed below.

- A systematic review of the most used numerical methods for uncertainty quantification is carried out with a clear focus of SCWE application.
- A comparative study of the various methods in uncertainty quantification for the coupled problem of wind-structure interaction is presented. The efficacies of various methods for the benchmark cases are systematically presented and discussed. The advantages, disadvantages, and applicability of each of the methods are discussed.
- A framework that uses adjoint sensitivity information for the uncertainty quantification in polynomial chaos is presented. A two-step surrogate approach that reduces the computational efforts using this is proposed and is presented for geometric uncertainty in flow problems. The applicability to wind engineering is discussed.
- The effect of uncertainties on a benchmark Commonwealth Advisory Aeronautical Council (CAARC) building under uncertain wind load is studied using the polynomial chaos approach.
- The effects of uncertainties of various parameters for wind effects on structure are quantified using global sensitivity analysis.
- Conditional value at risk is proposed as a measure for the performance evaluation of a time-varying quantity of interest for a complex phenomenon like wind engineering. The applicability in wind engineering is demonstrated for benchmark CAARC building under uncertain wind conditions.
- A significance testing based on the conditional value at risk between structural design options is proposed for the performance-based design selection of structures under uncertain wind loads.
- A novel workflow with risk-averse optimization based on conditional value at risk for Optimization Under Uncertainty (OUU) is presented.
- An adaptive sampling strategy for OUU for CWE problems at hand is used in this thesis and the efficacy of this novel approach is demonstrated.

- The proposed OUU workflow is applied for the shape optimization of buildings under location-specific uncertain wind loads. It is shown that the risk-averse strategy results in better-performing building shapes, indicating the significance of the proposed OUU strategy.

1.5 Outline of the thesis

The rest of the chapters are structured as below.

Chapter 2 presents various methods and their formulation for the forward propagation of uncertainties.

Chapter 3 presents various sources of uncertainty for wind engineering problems and how they can be represented. The chapter also discusses various quantities of interest for a time-varying complex phenomenon like that of wind engineering and proposes conditional value at risk as an efficient risk measure.

Chapter 4 presents the novel OUU framework developed and adopted for shape optimization of buildings under location-specific wind conditions.

Chapter 5 compares the approaches presented in chapter 2 for coupled FSI benchmark cases, the results are compared, and the applicability of each of the methods is presented for the coupled problem under consideration. The various forward UQ methodologies are explored and elaborated in this chapter. The advantages and applicability of the various methods are elaborated.

Chapter 6 describes the improvements of UQ for structural problems with sensitivity information by the adjoint approach. The proposed workflow is elaborated for a series of test case examples and demonstrates the computational efficiency.

Chapter 7 presents the verification and validation of the CAARC benchmark case, which is used as the demonstrator example in the later sections of the thesis.

Chapter 8 presents the uncertainty quantification for the benchmark test case CAARC building. A one-way coupled simulation is used for the wind-structure interaction. It also introduces a novel significance testing based on the conditional value at risk between design options for the performance-based design selection.

Chapter 9 discusses the OUU framework for shape optimization under location-specific wind conditions. The twist and tapering of a building are optimized such that the force resultant on the structure is minimized. A comparison is made between deterministic, risk-neutral, and risk-averse optimization designs, demonstrating the superior performance of the risk-averse design.

Chapter 10 summarizes the outcome of the thesis and provides recommendations for future studies.

All models are wrong, some are useful

George Box

CHAPTER 2

UQ IN STRUCTURAL WIND ENGINEERING: A REVIEW OF METHODOLOGIES

Uncertainty quantification has gained much attention in the past decade. The developments happening in the applied mathematics community need to be adapted to engineering disciplines. This comes with its own unique challenges from a specific application. The basics of various uncertainty quantification methods are introduced in this chapter. The theory, implementation, and other details of these methods are described in detail. The chapter starts with the classic Monte Carlo method and its implementation. Multi-level Monte Carlo method is introduced as a variance reduction technique to Monte Carlo. Generalized polynomial chaos and neural network as a cheaper surrogate is also presented here in this chapter. The UQ workflow based on each of these four methods is elaborated.

2.1 Uncertainty quantification in engineering applications

A real-world engineering simulation problem has many uncertainties associated with it; hence, a deterministic model is not sufficient to make realistic predictions. A computer simulation that incorporates the uncertainties from various sources also into consideration is closer to reality. Uncertainty quantification is the realistic and common way of representing the uncertainties from various sources, which cannot be assigned for a deterministic analysis and hence is not included in the deterministic prediction. This takes into account the uncertainties appearing in the input parameters as well as the modeling of the physical system for studying the impact of these uncertainties on the system response quantity of interest.

In structural engineering practice, the deterministic approach is commonly adopted for analysis and design. In a deterministic approach, a single value is used to define a parameter. However, neither the computational model nor the input parameters of the model are not known with full certainty in the real-world scenario. Observations clearly show the random characteristics of input parameters. A deterministic model assumes its output to be not uncertain as long as its input is fixed, whereas, for a stochastic model, a single input may give different outputs at different runs. Hence, a probability measure such as a Probability Density Function (PDF) represents the uncertain parameter. In the stochastic concept, each parameter is called a random variable, and the associated uncertainty is quantified in terms of a probability measure such as the PDF. Readers are referred to [35] for the basics of uncertainty quantification, probability theory, and different random variables.

2.1.1 Forward propagation of uncertainty

Figure 2.1 gives a schematic representation of the forward propagation of uncertainty in structural wind engineering. The three steps of the forward propagation of uncertainty are also indicated in Figure 2.1. The main steps of forward propagation of uncertainty are:

i. development of an accurate deterministic/stochastic model,

ii. identification and characterization of input parameters, and

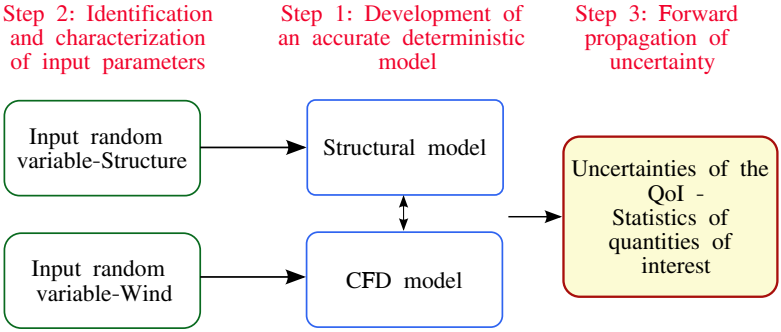

Figure 2.1 : Steps for forward propagation of uncertainties in structural wind engineering.

iii. forward propagation of uncertainty.

In the first step, theoretical/mathematical models are developed to represent the real-world problem. The computational model is derived from this mathematical model and is used to predict quantities of interest. There can be several outputs from a computational model. However, for an engineer/researcher, specific quantities are of more interest than others because they govern decision-making. These are referred to as Quantities of interest (QoI). The computational model may be stochastic or deterministic. Developing a new stochastic model for each new problem may be time-consuming and require expert knowledge. The uncertainty quantification methods may be intrusive or non-intrusive. Intrusive methods generally need access to the model and reworking the existing deterministic numerical and computational models. In many engineering applications, the computational model/code may be closed source, or the user has limited understanding, knowledge, or access to the inside of the model. In these cases, non-intrusive uncertainty quantification methods that use well-tested deterministic models or legacy codes come in handy.

Let's consider the deterministic model to be of the form,

$$Y = F(x). \tag{2.1}$$

where, x is the vector of input parameters, and Y is the output QoI. The function that produces the QoI from the input parameters can be as simple

as a mathematical function to as complex as a complete finite element model or a coupled finite element model in the case of structural wind engineering.

In the second step, uncertain input parameters are identified, and uncertainty for each input is well characterized by probability measures such as probability density functions. Since the input parameters are uncertain, x is modeled as a random variable, and hence Y automatically becomes a random variable as well.

Uncertainties in structural wind engineering problems can arise from various sources such as,

- The geometric parameters of the structural system, such as the cross-sectional area, moment of inertia, length, etc., of the structural elements.
- The material properties such as the modulus of elasticity, Poisson's ratio, other non-linear material parameters, etc., of the different materials used in the model.
- The parameters that define the various loading of the system, such as, but not limited to, the velocity of the wind, terrain condition, amount of live loads acting on the structure, snow and earthquake loading conditions, etc.
- The boundary and initial conditions imposed on the model, such as the support reactions, wind load profile, etc.

The sources of these input uncertainties are identified, and the respective uncertainties are characterized by the information on inputs obtained from experimental observations, expert knowledge, etc. A distinction between aleatoric and epistemic uncertainties is made for the above-listed items. The geometric parameters of the system can be classified as epistemic since they can be reduced by improved measurements. The others in the above list are mostly aleatoric. Here, this thesis discussion mainly focuses on the uncertainties of the wind and structural parameters modeled as aleatoric as argued in Section 1.3.1.

2.2 Forward propagation of uncertainty – an introduction to different approaches

The various methods available for forward propagation of uncertainty are briefly explored in this section.

The computation of output response uncertainties can be done explicitly for the linear parameterized models. Stochastic quantities such as the mean and standard deviation of the QoI can be obtained explicitly from the probabilistic description of the input parameters (mean and standard deviation). These are applied to X-ray tomography problems in [37].

A truncated multi-dimensional Taylor expansion for the output quantities of interest yields approximate uncertainty criteria in the perturbation method. The order of the Taylor series determines the accuracy of the method [38]. In the perturbation method, the series expansion is formed around the mean value of each input parameter. The method is used widely in structural mechanics [39]. The perturbation method can be used for FEM models as well. Formulations for higher-order moments are presented in [38]. An application to a multi-degree of freedom system can be found in [40].

Reliability-based methods focus on the tail of the PDF. The probability of failure is computed as the probability of exceedance of the prescribed failure criteria. First-order-reliability-methods (FORM) and second-order-reliability-methods (SORM) are widely used in structural engineering applications due to the simplicity of the method. They use a linear and second-order approximation of the failure domain, respectively. These methods focus on the failure domain alone and do not provide a complete stochastic picture of the QoI.

One of the most widely used and easy-to-implement uncertainty quantification methods is the sampling method. The frequently used sampling is the classical Monte Carlo (MC). The method was presented first in [41]. A sampling from the input uncertain parameter space is carried out, and the model is evaluated at each of these sampling points. MC then evaluates the statistical quantities and probability measures of the QoI, from the ensemble of QoI obtained by computing the statistics of these values. The sampling method is non-intrusive since they consider the model as a black box. They also do not suffer from the curse of dimensionality and, hence, can be used for cases with a large number of uncertain parameters.

Various improvements have been proposed to the standard Monte Carlo methods. One of the major research directions is to use non-random sampling strategies like quasi-Monte Carlo sampling [42] and Latin hypercube sampling [43]. Another way to reduce the mean square error is to use variance reduction techniques. Here, different levels of discretization in the FEM models are used. This is referred to as the Multi-level Monte Carlo method. It has been proposed in [44] and has attained much attention in recent times [44, 45]. Another approach is to use multi-fidelity methods, where instead of different discretization levels, different fidelities of the computational model are used.

Another class of methods is called surrogate models. In the surrogate method, the actual model is replaced by an approximate input-output relation. Once the surrogate models are available, it is possible to sample practically at negligible additional cost from these surrogate models. However, creating an accurate surrogate model is challenging and depends mainly on the kind of problem at hand. The response surface method describes the relationship between various input parameters and one output using a polynomial function [46]. Spectral methods are another class of methods where the uncertain parameters are represented as a series expansion called spectral expansion [47]. Polynomial Chaos (PC) expansion is presented to describe functions of Gaussian random processes in [48]. The terminology of chaos is a misnomer here as the model under consideration is not really chaotic.

Neural networks can also be used as an effective surrogate method to represent input-output relations. The choice of the experimental design that is used to generate data for neural network training is of great importance when it comes to the accuracy of these surrogates. The recent developments happening in artificial intelligence, machine learning, neural networks, etc., are promising to look into this method for uncertainty quantification. The accuracy and computational cost largely depend on the construction of surrogates and their performance in the region of interest.

2.3 Monte Carlo method for uncertainty propagation

The Monte Carlo algorithm is the most widely used method in uncertainty quantification and probably the universal tool for this purpose. The Monte

Carlo simulation method is a sampling method that relies on repeated random sampling from inputs to obtain the stochastic response of a model. The first step in MC simulation is to generate random numbers to follow the given probabilistic description of input parameters. A chosen random number generator tool is used to achieve this task. In direct MC simulation, corresponding to each generated input, the deterministic model is evaluated, and the QoI is collected. From the set of QoI, probabilistic measures such as the PDF, CDF, mean and standard deviation, etc., of the uncertain output parameter can be evaluated.

2.3.1 Details of Monte Carlo methods

The Monte Carlo(MC) estimate of a QoI Y is the average of N samples. The random vector x represents the input uncertainties. The quantity of interest Y is approximated in a FEM approximation of Y_h. Using this FEM approximation, the MC estimator is given by

$$E[Y_h] = \frac{1}{N}\sum_{n=1}^{N} Y_h^{(n)} \tag{2.2}$$

where, $Y_h^{(n)} = Y_h(x^{(n)})$.
The mean square error of an MC estimator is given by

$$err_{ms}^2(Y_h) = \frac{1}{N} Var(Y_h) + (E[Y_h - Y])^2 \tag{2.3}$$

The RMS error of the estimator is $O(N^{-1/2})$. To get an accuracy twice the initial one, one needs to quadruple the number of samples. This can be a trouble in cases with a large FEM model with an enormous number of degrees of freedom. In Eq. 2.3 the second term is the bias due to finite element discrimination. This term decreases with the decrease of the mesh size h. The first term is the variance error. To achieve this condition, one needs to choose a small enough mesh size to reduce the second term and a large enough sample size to reduce the first term. The classical MC algorithm is shown in Algorithm 1

Algorithm 1 Monte Carlo Algorithm

1: Set the number of samples, N
2: Set a tolerance level, ϵ
3: Set the sample mean, μ_0, and sample variance, σ_0^2, to zero
4: **For** i = 1 to N
5: Generate a random sample from the input distribution
6: Evaluate the QoI
7: Update the sample mean and sample variance
8: **If** Convergence criteria met (Eq. 2.3)
9: break
10: **End If**
11: **End For**
12: Post-process to obtain probabilistic measures of QoI

2.4 Multi-Level Monte Carlo (MLMC) method

The idea of MLMC was introduced and used extensively by [44] and [45]. The basic concept of MLMC for a finite element model is explained here in this section. The goal of MLMC is to decrease the overall computational cost. The QoI is computed from several finite element meshes. A hierarchical system of finite element spaces is created hence the name 'multi-level'. All of these FE meshes give a good approximation of the QoI. Now the sampling is done from these multiple levels of approximations. It is cheaper to compute the QoI in the coarse mesh and is expensive to compute the same in the fine mesh. However, the coarse mesh convergence is slow compared to the fine mesh. MLMC method exploits these facts. The method uses more samples from the coarse grid and a low number of samples from the fine grid. The number of samples from each level is inversely proportional to the cost of evaluation of the QoI at that level. This strategy allows getting an overall convergence at a lesser cost by sampling from multiple levels of the model.

Figure 2.2 shows the multiple levels of meshes as an indication compared to standard Monte Carlo, where sampling is done from the finest level alone. It may also be observed that the number of samples in MLMC is distributed all along the various grid levels.

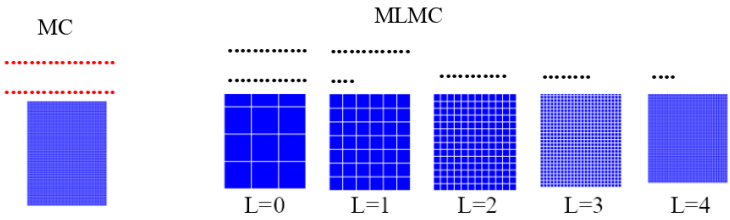

Figure 2.2 : MC v/s MLMC - Multiple levels used in MLMC v/s single finest level in MC. The dots indicate the number of samples drawn at each level.

2.4.1 Two-level Monte Carlo

To reduce the RMS error in Eq. 2.3 is to either increase the number of samples or reduce the variance. MLMC tries to reduce the variance and hence tries to bound the error to ϵ^2.

In two-level Monte Carlo, there are two discretizations, 1 and 0. Y_0 is coarser compared to Y_1. It is much cheaper to evaluate Y_0 compared to Y_1, then the two-level Monte Carlo estimator is given by

$$E[P_1] = E[P_0] + E[P_1 - P_0] \tag{2.4}$$

$$E[P_1] = \frac{1}{N_0}\sum_{n=1}^{N_0} P_0^{(n)} + \frac{1}{N_1}\sum_{n=1}^{N_1}(P_1^{(n)} - P_0^{(n)}). \tag{2.5}$$

If we define C_0 and C_1 as the cost of computing a single sample of Y_0 and $Y_1 - Y_0$, then the total cost of computing the MLMC estimator is

$$C = N_0 C_0 + N_1 C_1. \tag{2.6}$$

If we define V_0 and V_1 to be the variance of Y_0 and $Y_1 - Y_0$, then the overall variance is

$$C = N_0^{-1} V_0 + N_1^{-1} V_1. \tag{2.7}$$

The variance is minimized for a fixed cost by choosing

$$\frac{N_1}{N_0} = \frac{\sqrt{V_1/C_1}}{\sqrt{V_0/C_0}}. \tag{2.8}$$

2.4.2 Multi-level Monte Carlo formulation

The Multi-level is a generalization of the two-level explained in the previous section. Given a sequence of $Y_0, ..., Y_{L-1}$, the multi-level estimator is given by

$$E[Y_L] = E[Y_0] + \sum_{l=1}^{L} E[Y_l - Y_{l-1}] \tag{2.9}$$

$$E[Y_L] = \frac{1}{N_0} \sum_{n=1}^{L} \{ \sum_{n=1}^{N_l} (Y_l^{(n)} - Y_{l-1}^{(n)}) \}. \tag{2.10}$$

Where $Y_0, ..., Y_{L-1}$ are approximations of Y_L with increasing accuracy and also of increasing cost. The variance of the MLMC estimator is minimized for a fixed computational cost by choosing

$$N_l = \sqrt{V[Y_l]/C_l}. \tag{2.11}$$

The expression for optimal N_l is given by

$$N_l = [2\epsilon^{-2} \sqrt{V_l/C_l} (\sum_{l=0}^{L} \sqrt{V_l C_l})] \tag{2.12}$$

To reduce the mean square error of the estimator to ϵ^2 it is enough to bound the error of each terms to $\epsilon^2/2$. While the variance at levels and weak error decreases exponentially, we state the following theorem for details.

Theorem 1 [44, 49]
Given the positive constants $\alpha, \beta, \gamma, c_1, c_2, c_3$ such that $\alpha \geq \frac{1}{2} min(\beta, \gamma)$ and assume that the following conditions hold:

1. $E[P_l - P] \leq c_1 2^{-\alpha l}$
2. $V_l \leq c_2 2^{-\beta l}$
3. $C_l \leq c_3 2^{\gamma l}$

Then, there exists a positive constant c_4 such that for any $\epsilon < e^{-1}$ there exists an L and a sequence $\{N_l\}$ for which the multi-level estimator has a mean square error $e\,r\,r^2_{ms} \leq \epsilon^2$, and computational complexity C with bounds

$$E[C] \leq \begin{cases} c_4 \epsilon^{-2} & \beta > \gamma, \\ c_4 \epsilon^{-2} (log\,\epsilon)^2 & \beta = \gamma \\ c_4 \epsilon^{-2-(\gamma-\beta)/\alpha} & \beta < \gamma. \end{cases} \tag{2.13}$$

[44] can be referred for proof.

2.4.3 MLMC Algorithm

The MLMC algorithm implemented is adopted from [49]. The same is presented in Algorithm 2.

Algorithm 2 MLMC algorithm

1: Start with L = 2, and the initial target of N_0 samples on levels l = 0,1,2
2: **While** Extra samples need to be evaluated **do**
3: Evaluate extra samples on each level
4: Compute/update estimates for $V_l, l = 0, 1, ..., L$
5: Define optimal $N_l, l = 0, 1, .., L$
6: Test weak convergence
7: **If** not converged , set $L = L + 1$, and initialize target N_L
8: **End if**
9: **End While**

2.5 Generalized Polynomial Chaos Method

The polynomial chaos approach is a surrogate method that computes the forward propagation of uncertainty at a faster rate than sampling approaches. In the generalized polynomial chaos (PC) method, a spectral

representation of uncertainties, both the input and output uncertain parameters are represented by a PC expansion. PC expansion is a truncated polynomial series, and it consists of coefficients that are deterministic and orthogonal basis [47]. In the PC method, the random variable of interest is projected into a stochastic space defined by the orthogonal base functions (Ψ). These base functions are functions of random vectors (ξ). The random vector consists of multiple random variables depending on the problem at hand. Each random variable has a random space associated with it. $\xi_i \in \Omega_i$. The random variables are assumed to be independent and identically distributed (i.i.d). The uncertain parameters are represented by PC expansion as

$$X_j = \sum_{i=0}^{\infty} x_i \, \Psi_i(\xi_j) \,, \tag{2.14}$$

for practical purposes Eq. 2.14 may be truncated to a finite number of P terms.

$$X_j \approx \sum_{i=0}^{P} x_i \, \Psi_i(\xi_j) \,, \tag{2.15}$$

P is a function of the order (p), and dimensionality (n) of PC expansion.

$$P = \frac{(n+p)!}{n!\,p!} - 1 \tag{2.16}$$

The dimensionality of the problem is equal to the number of uncertain inputs. It may be observed that the total number of PC expansion terms rapidly grows with the number of dimensions. This is referred to as the curse of dimensionality. Hence, applying the PC expansion to high dimensional problems will be challenging [50].

Orthogonality of basis function

There exists the orthogonality property for the random base function such that

$$E[\Psi_i, \Psi_j] = E[\Psi_i^2]\delta_{ij} \tag{2.17}$$

where, δ_{ij} represents the Kronecker delta function and E is the expectation defined as,

$$E[\Psi_i, \Psi_j] = \int_{\Omega} \Psi_i \Psi_j \rho(\xi) d\xi \tag{2.18}$$

where ρ is the probability distribution function (PDF) of ξ.

There exists an orthogonal polynomial basis corresponding to each random variable of standard distribution [50] called the optimal polynomial. For normally distributed random variables, a Hermite representation may be used. For other standard distributions [50] may be referred. The optimal representation has a minimum number of terms, as higher-order coefficients are zeros.

2.5.1 UQ workflow based on PC expansion

In this section, the details of the steps involved in the UQ workflow based on PC expansion are elaborated. In forward propagation of uncertainty with PC expansion, both the input and output uncertain parameters are represented by the PC expansion.

PC expansion of the inputs

Firstly the uncertain input parameters are represented as PC expansion as in Eq. 2.15. The probability distribution of these input parameters is known. The probabilistic description of these inputs is obtained from experimental data or selected as standard distributions with known parameters based on experience or expertise. The basis function Ψ is chosen such that they are the optimal polynomial for the PDF of the random input variables, as explained in the previous section.

In the case of Hermite polynomials, few Hermite polynomials are

$$\begin{aligned} H_0(\xi_i) &= 1, \\ H_1(\xi_i) &= \xi_i, \\ H_2(\xi_i) &= \xi_i^2 - 1, \\ H_3(\xi_i) &= 1\xi_i^3 - 3\xi_i, \\ H_4(\xi_i) &= \xi_i^4 - 6\xi_i^2 + 3 \quad \text{etc.} \end{aligned}$$

The PC expansion coefficients of Eq. 2.15 can be found out using the orthogonality property of the Hermite polynomials as,

$$x_i^j = \frac{1}{< H_i^2 >} \int_{-\infty}^{\infty} X_j H_i(\xi(j)) \rho(\xi_j) d\xi_j. \tag{2.19}$$

Where $< H_i >$ denotes the inner product and $\rho(\xi_j)$ is PDF of the the j^{th} input parameter. For normally distributed random variables, the Hermite polynomial is the optimal polynomial, and hence the PC representation is reduced to

$$x_i^j = \mu_j + \sigma_j \xi_j \tag{2.20}$$

where μ is the mean of the j^{th}random variable and σ is the standard deviation of the random variable. Hermite polynomials can also be used for lognormal distributions, and the representation is presented in [51].

PC expansion of the outputs

In the next step, the output parameter is also represented by a PC expansion as

$$Y \approx \sum_{i=0}^{P} y_i \, \Psi_i(\xi) \,, \tag{2.21}$$

here ξ is a multi-dimensional random vector. P can be found out from Eq. 2.16. Since the order of the expansion is n, it is called a PC—n representation. The coefficients of polynomial expansion can be obtained by various intrusive and non-intrusive methods such as stochastic Galerkin, discrete projection, or least square regression. Focus is given more on the collocation method based on the least square regression. More details of stochastic Galerkin and discreet projection can be found in [50, 52–54]

Collocation method based on least square regression

Unlike the intrusive method, the non-intrusive method treats the problem as a black box. No knowledge of governing equations is needed in this solution technique. Hence this method is quite useful for FEM models where the governing equations are not explicitly known. Systems having

nonlinearity or systems with complex stochastic equations can also be determined with ease in this class of methods. A well-known strategy is the collocation method, which is based on the least square minimization of the discrepancy between the uncertain parameter and its truncated PC expansion.

In collocation methods, the error is forced to make zero at certain points of the random space, and these points are called collocation points. The collocation points are selected in the random space. Let $\xi^1, \xi^2, ...\xi^n$, are n collocation points and $Y_1, Y_2, ..., Y_n$ be the response at these collocation points. A linear regression approach is adopted for finding out the PC coefficients. At each chosen collocation point, Eq. 2.21 results in a set of linear equations,

$$\Psi\alpha = Y. \tag{2.22}$$

where α is a vector of unknown PC coefficients, Ψ matrix of base function values at the collocation points, and Y is the vector of responses at the collocation points as,

$$\begin{bmatrix} \Psi_0\left(\xi^1\right) & \cdots & \Psi_P\left(\xi^1\right) \\ \vdots & & \vdots \\ \Psi_0\left(\xi^n\right) & \cdots & \Psi_P\left(\xi^n\right) \end{bmatrix} \begin{Bmatrix} y_0 \\ \vdots \\ y_N \end{Bmatrix} = \begin{Bmatrix} Y^1 \\ \vdots \\ Y^n \end{Bmatrix} \tag{2.23}$$

The number of collocation points should be at least equal to the number of unknown PC coefficients. If the number of available equations is greater than the number of unknowns, regression analysis based on the least square approach is adopted to solve for α in Eq. 2.22.

As mentioned above, to determine the unknown coefficient y_i, the response of the system has to be evaluated at a set of input parameters obtained for specific values of the uncertain random variable, known as the collocation points. For a univariate system, the collocation points are selected as zero, and the roots of one order higher polynomial that is used to approximate the response. If more points are needed, they are chosen in such a way that they are distributed symmetrically about the mean value from the PDF of the random variable. The stochastic collocation method is easy to implement and leads to solutions easily, even for problems with nonlinearity, much more efficiently compared to intrusive methods.

For multivariate problems, a common methodology adopted is to find the collocation points from the full tensor product space. Since the number of points in the full tensor product grid increases exponentially with the dimension, these grids suffer from the curse of dimensionality. Sparse grids may be used to tackle these problems. Another strategy to choose a collocation point is based on the invertibility of the matrix Ψ, [52] which will be referred to in detail in Section 6.2.2.

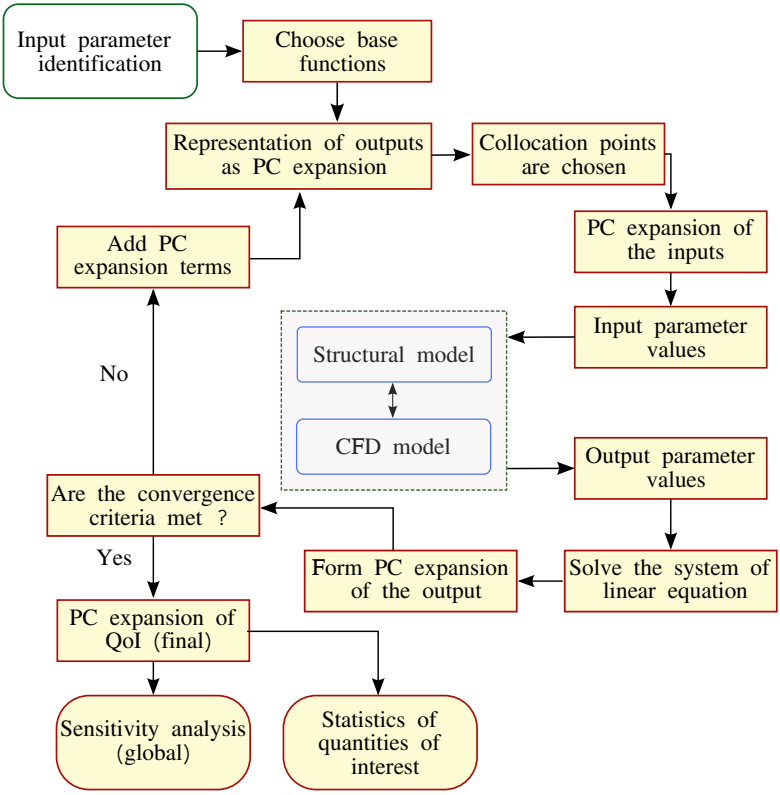

Figure 2.3 : Workflow of PC expansion based on collocation method.

Convergence criteria of polynomial chaos expansion

Based on the accuracy demand of the user, the order of the PC representation is chosen for the given problem. The solution process starts with a first-order PC expansion of the output random variable. The PC coefficients are determined for this expansion. Once the PC expansion of the output is determined, convergence criteria are checked with the previous expansion to determine how good the representation is. If convergence criteria are not met, the order of the PC expansion is increased, and new terms are added to the expansion. The process is continued until the chosen convergence criteria are met. The mean and variance, the first two moments, are considered to be important parameters in estimating the accuracy of PC expansion [47]. Since the convergence of PC approximation is in the mean square sense, the convergence of higher-order moments is not guaranteed. Different convergence requirements suggest different convergence criteria for the random variable. Increasing the number of terms in the PC expansion improves the convergence of the random variable. Please refer to [50] for a detailed discussion on convergence. The PC expansion of an uncertain parameter Y is said to converge if,

$$\lim_{P\to\infty}\left(\sum_{i=0}^{P} y_i\Psi_i(\xi)\right) = Y \tag{2.24}$$

Post-process of results

The post-processing can be done easily from the obtained PC expansion to get the mean, standard deviation, and other moments as in Eq. 2.25. Also, the obtained PC expansion can be used to sample from as model evaluations are cheaper to evaluate. This can, hence, be used for reliability computation, PDF estimation, etc.

$$\mu = y_0 \tag{2.25}$$

$$\sigma^2(Y) = \sum_{i=0}^{P} y_i^2 - y_0^2 \tag{2.26}$$

Sensitivity analysis explores the sensitivity of the QoI to the inputs. The variability of the QoI with respect to the inputs is quantified. Sobol' indices are a variance-based sensitivity analysis. The Sobol' indices are computed

from polynomial chaos expansion as in [52]. The Sobol' indices can be found out from the polynomial chaos expansion easily with negligible additional computational cost. The variance from the PC expansion can be found out as,

$$D_{\mathrm{PC}} = \sum_{j=1}^{P} y_{\mathrm{j}}^2 E\left[\psi_{\mathrm{j}}^2\right] \tag{2.27}$$

The response expansion coefficients are gathered according to the dependency (α) of each basis polynomial on j^{th} input, which is square summed and normalized to obtain the sensitivity indices. The total PC-based Sobol' indices can be found out as,

$$S_{\mathrm{j}}^{\mathrm{T}} = \sum y_{\alpha}^2 E\left[\psi_{\alpha}^2\right] / D_{\mathrm{PC}} \tag{2.28}$$

2.6 Neural network (NN) surrogate for uncertainty quantification

Neural networks can be used as an effective surrogate model and hence used for uncertainty quantification. This is based on the mapping between input-output pairs. The data generation for creating input-output pairs is achieved by running multiple deterministic simulations and can be expensive, like the sampling approaches. The trained NN surrogate is used for UQ by sampling from the surrogate in a Monte Carlo fashion. The details and applicability of the methodology for UQ are elaborated on and critically evaluated here in this section. Recently Physics Informed Neural Network (PINN) has been used to combine prior knowledge of the partial differential equation and the NN[55, 56].

The governing PDE for a continuous solution field u with respective boundary conditions on the domain Ω_d is described in Eq. 2.29. A system of equations has resulted in the numerical approximation in the Galerkin-based finite element method as Eq. 2.30.

$$\mathcal{L}(u) = 0 \qquad \text{in } \Omega_d \tag{2.29}$$

$$K(u^h)u^h = F \tag{2.30}$$

where, $K(u^h)$ is the stiffness matrix, u^h is the discretized solution field, and F is the force vector. The system of the equation may be rewritten in residual form as

$$r(u^h) = K(u^h)u^h - F \tag{2.31}$$

An iterative strategy like the Newton-Raphson Method is used for the solution of u^h. For a large problem with thousands of degrees of freedom, this linear solver step is expensive and time-consuming.

2.6.1 NN surrogate construction and backpropagation

A neural network surrogate can be created as a mapping from input random variables $\mathbf{x} = [x_1, x_2, ...x_m]$ to output random variables $\mathbf{Y} = [y_1, y_2, ...y_n]$ for the purpose of uncertainty quantification where L is the number of hidden layers in the network. Each layer has trainable weights w_l and biases b_l associated with them. Neural network training is an optimization problem that aims to find the best-suited weights and biases that minimize the discrepancy (called loss function) between the true value and the prediction of the output random variable. Backpropagation is a specific algorithm used in training neural networks that adjusts the weights and biases to minimize the loss function δ. In backpropagation, the gradient of loss function δ with respect to weights and biases are calculated, and then they are updated as,

$$w_l = w_l - \eta \frac{\partial \delta}{\partial w_l} \tag{2.32}$$

where η is the learning rate chosen by the user. The gradients in Eq. 2.32 are computed using chain rules.

$$\frac{\partial \delta}{\partial w_l} = \frac{\partial \delta}{\partial y} \frac{\partial y}{\partial w_l} \tag{2.33}$$

Eq. 2.33 is dependent on the loss function chosen by the user. The mean square error (MSE) $\delta_{MSE} = \frac{1}{m}\sum_{i=i}^{m}(y_i - y_i^t)^2$ is chosen as the loss function in this study. Here, y^t are the true values of output random variables.

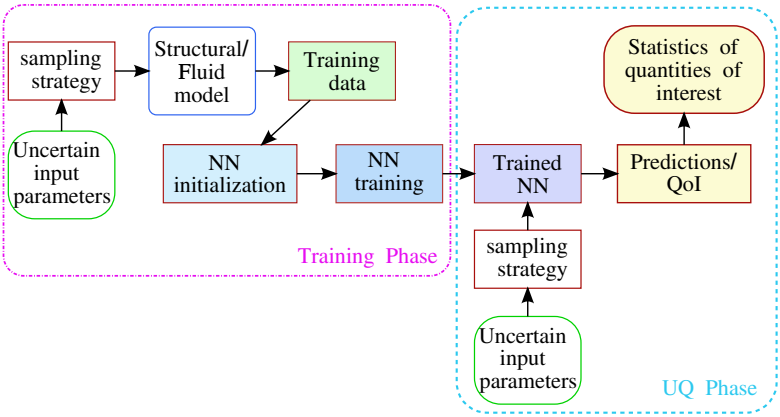

Figure 2.4 : Workflow of neural network used as a surrogate for uncertainty quantification in structural wind engineering applications.

2.6.2 UQ workflow based on Neural Network surrogate

The NN-based workflow for uncertainty quantification is presented here in this section. The NN can be used as an effective surrogate for uncertainty quantification, and the workflow is shown in Figure 2.4. The whole process has two stages. In the first phase, the NN surrogate is created. For this purpose, the deterministic model is run at selected experimental designs, and the data is generated. The experimental design also follows the random input variables. At least they should cover the support of the input uncertain variables. This is the most expensive step for problems with high computational costs. Once the data is available, one could train a NN for the input-output data pair created. The second phase is the UQ phase, where the NN surrogate is used for uncertainty quantification. Here, firstly, sampling is done from the inputs to follow the known distribution. Instead of the PDE, sampling is carried out from the surrogate to obtain the output QoI. Once the QoI is collected, the post-processing can be done in a Monte Carlo way, and the probabilistic description of the QoI can be obtained.

Wind extinguishes a candle and energizes fire. Likewise, with randomness, uncertainty, and chaos, you want to use them, not hide from them. You want to be the fire and wish for the wind.

Nassim Nicholas Taleb

CHAPTER 3

UNCERTAINTIES IN STRUCTURAL WIND ENGINEERING

Two important decisions in uncertainty quantification are identifying and characterizing the input uncertainties as well as defining the quantities of interests. This chapter describes the various input uncertainties, both from wind and structures, that must be considered for wind engineering applications and the QoIs relevant for structural wind engineering. A comprehensive description of location-specific input uncertainty characterization is presented and elaborated. Equally important to input uncertainties is defining the quantity of interest. In many cases, a simple average is inadequate for engineering applications. It is essential to look at the distribution's tails for this matter. A detailed description of the quantities of interest for structural engineers is also presented here. Conditional value at risk as a risk measure is presented and its suitability for wind engineering applications is discussed.

3.1 Multi-challenges of UQ in structural wind engineering

The current work focuses on identifying and quantifying the uncertainties in the structural wind engineering problem with wind modeled using the Finite Element Method (FEM) for the Large Eddy Simulation (LES). The application of uncertainty quantification for wind effects on structures has multiple challenges and is referred to as multi-challenges in this thesis as depicted in Figure 3.1. The multi-physics challenge comes from the fact that the analysis under consideration deals with the coupled wind-structure interaction problem. In recent times, there have been many advancements in the deterministic analysis of wind-structure interaction analysis. The fluid-structure interaction analysis can be done in a monolithic or a partitioned way. The partitioned approach has its advantages. A one-way coupling, a weak coupling, and a strong coupling can be employed in the analysis depending on the requirement of the problem. The field of coupling strategies and analysis methods for FSI has matured into its own research field [57].

The wind phenomenon at a location over a few years has two time scales - a micro scale and a macro scale. If we want to accurately capture both the climate and the weather effects on the structures during simulation, a multi-scale simulation is required. This brings some unique challenges in combining the two models. The independence assumption of the two scales is used in this thesis to define the inlet wind conditions.

The multi-dimensionality challenge comes from uncertainty quantification. The uncertainty may be coming from more than one source. This will lead to the fact that the dimension of the problem in the uncertain domain is not one but multi-dimensional. The high dimensionality of the stochastic problem will lead to unique challenges like the curse of dimensionality [50].

The multi-process challenge comes from high-performance computing as we need to run substantial CWE problems in multiple cores in parallel. Hence, this problem at hand is multidisciplinary and requires a multidisciplinary solution.

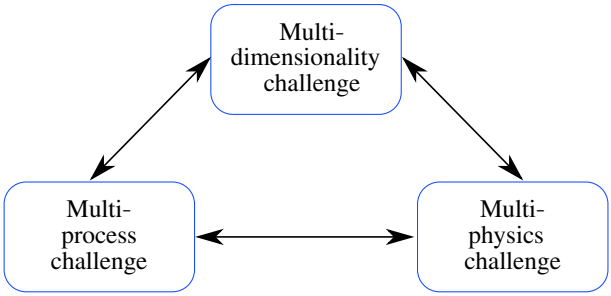

Figure 3.1 : Multi-challenges in uncertainty quantification for wind effects on structures

3.2 Uncertainties in wind parameters

There are various uncertainties in the wind parameters employed in this thesis. Here, the wind model used and the various uncertain parameters of the model are briefly described.

Due to the roughness of the surface of the earth, a strong friction effect is present retarding the uniform wind flow and forming the atmospheric boundary layer. The wind effects in the Atmospheric Boundary Layer (ABL) are modeled by decomposing the incoming wind velocity field as Reynolds decomposition, $u = \overline{u} + u'$, where, $\overline{u}$ is the steady mean profile component and u' is the unsteady turbulent fluctuations component.

The mean wind profile $\overline{u}$ is an average contribution to the overall wind field u. It changes in the time scale of a couple of hours to days [58]. Hence the mean profile is considered to remain consistent for the numerical simulation. The turbulent fluctuations of wind u' represent the wind gusts with a time span of seconds to a couple of minutes. The gust wind speed induces temporary states of maximum overall wind loading. It can induce resonant effects in large structures if their structural eigenfrequencies coincide with frequencies in the gust-induced wind load pattern. Two different models are used for each term $\overline{u}$ and u'. Similarly, the uncertainties of the two terms are dealt with separately in this work. Since these terms are of two different time scales, this modeling choice is justified.

3.2.1 Wind uncertainty modeling: mean profile

Almost all civil engineering structures exist inside the ABL flow. The terrain, adjacent structures, type of vegetation, etc., result in shear stress, affecting the wind flow at the specific location. These resulting air movements are of interest to the analysis and characterization of wind. The ABL is associated with the three regions along the height from the surface of the earth. The viscous sublayer is the closest to the earth, with low velocity and high shear stresses. The Prandtl layer is characterized by larger vortices with almost constant shear stresses. The third one is the Ekman layer, where the effects of Coriolis forces appear to take effect. The shear stresses tend to be negligible in this layer [59].

A logarithmic law is adopted here in this thesis. The wind shear is represented as

$$\frac{d\overline{u}}{dz} z \sqrt{\frac{\rho_{air}}{\tau_0}} = \frac{1}{k}. \tag{3.1}$$

The frictional velocity, u_* is expressed from the shear stress on the ground τ_0 by the formula $\tau_0 = \rho_{air} u_*^2$ [60]. We then have

$$\frac{d\overline{u}}{dz} \frac{z}{u^*} = \frac{1}{k} = \text{constant} \tag{3.2}$$

Integrating results in the logarithmic law for mean wind speed.

$$\overline{u}(z) = \frac{u^*}{\kappa} \ln(\frac{z}{z_0}). \tag{3.3}$$

Where κ is the Von Kármán constant. The value of κ is found to be 0.41. z_0 is the roughness length. Depending on the local terrain, the frictional forces will vary across the grass, vegetation, forest, water, or urban areas. These changes in local terrain type are adequately described by this roughness length parameter $z_0 > 0$. The value of this parameter for varying terrain types is available in code books [1]. The uncertainty of the roughness parameters is assumed to have a uniform distribution.

The mean velocity $\overline{u} = \overline{u}(z)$ can be modeled by the following quasi-logarithmic profile [60] furthermore considering the correction factor due to Coriolis effect as:

$$\overline{u}(z) = \begin{cases} \frac{1}{\kappa}\left(u_* \ln\left(\frac{z}{z_0}\right) + 34.5 f z\right) e(\theta) & \text{if } z \geq z_{\min}, \\ \overline{u}(z_{\min}) e(\theta) & \text{otherwise.} \end{cases} \tag{3.4}$$

Let's denote (x, y, z) as the Cartesian coordinates in the ABL around the structure to be designed. The direction of the mean wind is denoted by the unit normal vector $e(\theta) = (\cos(\theta), \sin(\theta), 0) \in R^3$. $z_{min} > z_0$ is the minimum height defined in [1], and $f = 10^{-4}$ is the Coriolis parameter.

The wind profile parameters u_*, θ, and z_0 in Eq. 3.4 are uncertain and therefore regarded as random variables in this study. The frictional velocity u_* and the incidence angle of wind θ are correlated variables. The windrose diagram characterizes the dependence of these two uncertain parameters. Analysis for the roughness length z_0 has been investigated in detail recently [61, 62]. In this thesis, we assume that z_0 is independent of the incidence angle, as well as the wind velocity. No details are available to imply the dependency between these parameters at given locations. Therefore, a uniform distribution, $z_0 \sim [z_L, z_U]$, where z_L and z_U are obtained from [63] depending on the terrain category used. In this thesis, we assume that z_0 is independent of u_* and θ, since no information is available on the dependence of these parameters.

3.2.2 Wind uncertainty modeling: directionality effects

The mean wind speed at reference height is correlated to the direction of the wind flow. It is incorporated in the adopted mean profile as in Eq. 3.4.

A windrose diagram illustrates the mean wind velocity along all directions at a location. The windrose represents the historical wind data at a given location. This historical wind data is employed to capture the dependency wind velocity and the incidence angle. A bivariate copula [30, 64] is employed to capture this dependence between θ and u_* in this thesis. It is well known and used in earlier studies that the mean wind velocity, averaged over all incidence angles θ, found to follow a Weibull distribution, Weib(λ, k), with a scale parameter λ and shape parameters k [58].

Similar to a windrose, a *roughnessrose*, which captures the relationship between z_0 and θ is also studied [58], but the data to calibrate such models is not available. Hence, the modeling assumption of independence of z_0 with u_* and θ is made in this thesis. As elaborated earlier, a bivariate copula is used to model the dependence between the random variables u_* and θ.

The bivariate copula model is calibrated with measurement data from the windrose diagram for location Basel, Switzerland at $z = 80$m from 2010-01-01 to 2015-12-31. The windrose data is available at `https://www.meteoblue.com`. The relation $u_* = (\kappa\overline{u} - 34.5fz)/\ln(z/z_0)$ by Eq. 3.4 implies that a copula model for θ and $\overline{u}$ can be used to represent the correlation between θ and u_*.

Multivariate copulas are used to create low-dimensional statistical models for random variables with complex dependencies [30, 64]. Sklar's theorem [65] is employed for generating the bivariate copula. A bivariate copula $C(\cdot,\cdot)$ is a distribution on the unit square $[0,1]^2$ having uniform $[0,1]$ marginals. For random variables X and Y, Sklar's theorem states that for all joint distribution $F_{X,Y}(\cdot,\cdot)$, a copula $C(\cdot,\cdot)$ can be defined such that

$$F_{X,Y}(x,y) = C(F_X(x), F_Y(y)), \tag{3.5}$$

where $F_X(\cdot)$ and $F_Y(\cdot)$ are the marginals of $F_{X,Y}(\cdot,\cdot)$. An empirical copula is employed, $\hat{C}_n(\cdot,\cdot)$ [66] in this thesis. More details on the copula creation can be found in Appendix A of [67].

Let $F_{\theta,\bar{u}}(x,y)$ represent the bivariate distribution function for the wind angle and mean velocity at reference height. Let $\{(\theta_i, \bar{u}_i)\}_{i=1}^n$ be a set of samples from the joint distribution of $(\theta, \bar{u})$. Next, define $\{(u_i, v_i)\}_{i=1}^n$ to be the transformed samples $(u_i, v_i) = (\hat{F}_\theta(\theta_i), \hat{F}_{\bar{u}}(\bar{u}_i))$, where $\hat{F}_\theta \approx F_\theta$ and $\hat{F}_{\bar{u}} \approx F_{\bar{u}}$ are consistent estimators of the true marginals. Here, $\hat{F}_\theta$ is constructed using a maximum likelihood estimate of a mixture of von Mises distributions with a prescribed orientation, and $\hat{F}_{\bar{u}}$ was constructed from the maximum likelihood estimate of a Weibull distribution. The empirical copula is defined from the set $\{(u_i, v_i)\}_{i=1}^n$ as follows:

$$\hat{C}_n(u,v) = \frac{1}{n}\sum_{i=1}^{n} I(u_i \le u, v_i \le v), \tag{3.6}$$

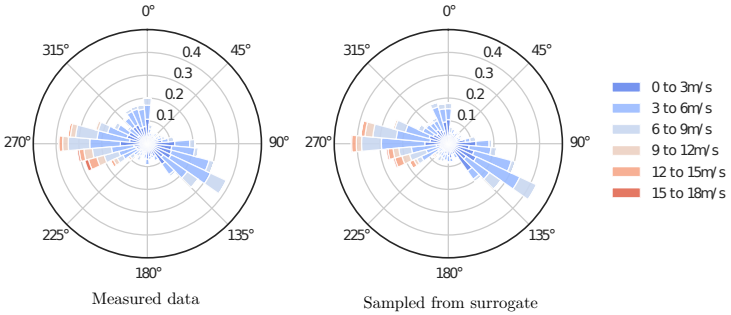

Figure 3.2 : Wind rose diagram representing the dependency between mean wind speed $\bar{u}$ and incidence angle θ. The figure shown is for location Basel, Switzerland at $z = 80$m from 2010-01-01 to 2015-12-31. The field data (left) is used to generate a copula surrogate, and the copula is sampled to generate the synthetic data (right).

where $I(a \leq b, c \leq d)$ is the indicator function

$$I(a \leq b, c \leq d) = \begin{cases} 1 & \text{if } a \leq b,\ c \leq d, \\ 0 & \text{otherwise.} \end{cases} \tag{3.7}$$

The set of transformed samples is in the unit square $[0,1]^2$.

With these definitions, the empirical, copula-based distribution function is defined as

$$\hat{F}_{(\theta,\bar{u})}(\theta, \bar{u}) = \hat{C}_n(\hat{F}_\theta(\theta), \hat{F}_{\bar{u}}(\bar{u})). \tag{3.8}$$

This function can be used to draw dependent samples of θ and $\bar{u}$.

Figure 3.2 shows the actual windrose for Basel and the bivariate copula model we calibrated for the location. It can be observed that they both agree well. The developed model can accurately capture the dependence between wind velocity and direction for the given location for historical data. The bivariate copula may be employed to generate the correlated samples needed for the UQ task while running the CDF simulations.

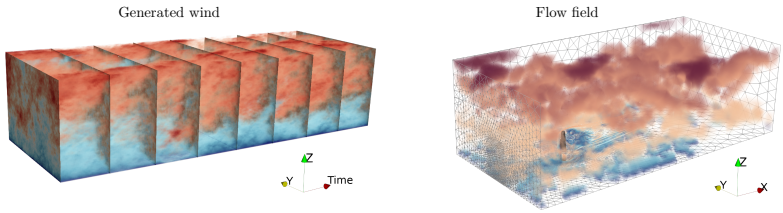

Figure 3.3 : Synthetic turbulent wind gusts $u'(t,y,z)$ are generated in the (t,y,z)-space (left) with Mann model. The 2D cuts of the wind block (y,z) are imposed on the inlet at time t as $u(t,x=0,y,z)=\overline{u}(z)+u'(t,y,z)$ for the CFD simulation (right).

3.2.3 Wind uncertainty modeling: turbulent fluctuations of wind

The wind fluctuations $u'(t,y,z)$ are modeled such that the wind statistics at the location of interest are captured. Different numerical models are used to handle this problem [68–71].

The widely used Mann model is employed in this thesis to model the wind gust fluctuations [60, 72]. The model is a well-established and widely used spectral model for wind generation in structural wind engineering [14, 73–75].

In the Mann model, the random velocity field is defined through the Fourier transform of the covariance tensor $R(r)$; namely, the so-called *velocity-spectrum tensor* $\Phi_{ij}(k)=\frac{1}{(2\pi)^3}\int_{C^3} e^{-ik\dot{r}}R_{ij}(r)dr$. As such, the synthetic turbulent fluctuations $u'=(u'_1,u'_2,u'_3)$ are defined by the inverse Fourier transform,

$$u'_i(x)=\int_{R^3} e^{ik\dot{x}}\sum_{j=1}^{3}C_{ij}(k)\xi_j(k)dk\,, \tag{3.9}$$

$C^*(k)=\Phi(k)$ and each $\xi_i\sim N(0,1)$ is an i.i.d. complex standard normal random variable. Where the positive-definite second-order tensor $C(k)$ is defined by the velocity-spectrum Φ via $C(k)C^\dagger(k)=\Phi(k)$, with $\dagger$ denoting complex conjugation of a matrix. Above, ξ_j, $j=1,2,3$, denotes Gaussian noise in R^3, i.e., each $\xi_j(k)\sim N(0,1)$ is independent and identically distributed complex standard normal random variable, and the integral in (3.9) is understood in the Fourier–Stieltjes sense. On a uniform tensorial

grid in C^3, with periodic boundary conditions, this integral can be approximated using the Fast Fourier transform; see, e.g., [60] for discretization details. Then, after generating a three-dimensional block of wind, the wind velocity can be mapped to the inlet of the computational domain of a CFD simulation as shown in Figure 3.3. Note that generating ξ_j requires a pseudorandom number generator. Without loss of generality, we assume that the corresponding seed r is uniformly distributed in $[r_L, r_U]$ (up to machine precision). Please refer to [60, 71, 73] for the explicit formula for $\Phi(k)$ and further details of the implementation of the wind generation process based on Eq. 3.9. The Mann model is calibrated to match the wind generated at a given location by matching the turbulence intensity profile, length scale, and wind spectra.

3.3 Uncertainties in structural parameters

Another source of uncertainty in structural wind engineering is the uncertainties arising from the structures. Structures may be built with various material properties that are associated with uncertainties. Some of the previous studies in the field have considered these uncertainties into account [76–79]. The various structural parameters may also not be known exactly in the modeling. The geometry of the structure or parameters of the system, such as the area of cross-section, moment of inertia, and length of the members, can be uncertain [76]. The material parameters, such as the modulus of elasticity and Poisson's ratio of the construction material, possess inherent uncertainties. The material properties assumed to have a unique value in the computational model are impossible to achieve in execution. The uncertainties in the strength of the material during the seismic analysis are considered in [77]. Another major source of uncertainty in structural engineering is the loads acting on the system. The various loads acting on the structure, such as the velocity of the wind, the earthquake magnitude, the amount of icing loads, the amount of live loads, etc., are associated with considerable variation.

An analysis of suspension bridges considering the uncertainties in wind velocity, geometry, and materials is presented in [78]. The various boundary conditions and initial conditions applied to the computational model also contribute to the uncertainties of the model. The support condition modeled in a computational model is impossible to achieve under real-

world conditions. A study considering uncertainties in foundation reaction is presented in [79].

The associated uncertainties of the structure are also considered in this thesis. Since a simplified model is used for the structure, the various parameters of the structure, like the stiffness and damping, are considered uncertain. These parameters are independent and hence can be considered as independent random variables. The distribution and associated probability definitions of each of these parameters are described later in each example. The uncertainty in the modeling is not considered in the study. Also, the uncertainties from the boundary conditions of the building, like the support reactions, are not considered. The assumption of fixed support at the ground for a building is found to be used largely in practice and widely accepted. Focus is given more on the parameter uncertainties that arise from the variation of the materials.

3.4 QoI in structural wind engineering

Let's focus our attention on the quantities of interest for structural engineering practice. Two main criteria need to be considered in the design of tall buildings: the strength and the serviceability criteria. The strength criteria deal with the capacity of the structure to resist the loads and guarantee that the building will not fail under the design load combinations. The serviceability criteria majorly ensure that the occupants are comfortable in the building. The various QoI from CFD are the forces and moments at the bases, called the shear forces and base moments. Since the building problem is in 3D, there are various components to this. One approach would be to take the magnitude of these forces as a QoI. These global forces represent the strength criteria of the building in consideration. The mechanical moment created at the center (O) of the base of the building B_z by the fluid pressure $p(x)$, simply called the base moment is defined as

$$M_z = \int_{B_z} (x - O) p(x) n(x) dS(x), \tag{3.10}$$

where $n(x)$ is the unit normal to the building surface. Another QoI will be the pressure along the various forces. Absolute pressure may be used for the design of local features, such as glass facades in all buildings or structures. The pressure may be represented as the normalized pressure

called the Coefficient of Pressure (C_p). Here in this thesis, the base forces and moments are considered as QoI. Also, the pressures on the various faces are also considered. The C_p can also be estimated by normalizing the surface pressure values. All these QoI are obtained as an output from the CFD analysis.

Another QoI of the structures is the displacement and acceleration at the top of the building. These QoI are of particular interest to engineers concerning the serviceability limit state. Here in this thesis, these two quantities are extracted from the structural model. All of the QoI mentioned above are time series in each simulation. It is challenging to treat these time-varying QoI's from each sample during the UQ analysis.

3.4.1 QoI of time series

All of the quantities of interest in wind engineering are time series. It is interesting to know which quantities be extracted from this time series that may be used for decision-making in the design stages. This section deals with the various risk measures that can be extracted from the time series of QoI.

Mean of a time series:
The average of a time series represents the central tendency and is computed as

$$E[X] = \frac{1}{N}\sum_{i=1}^{N} X(t_i) \tag{3.11}$$

Variance:
The standard deviation of a time series is a measure of the variation from the central tendency (mean). The variance may be computed as

$$Var[X] = \frac{1}{N-1}\sum_{i=1}^{N} (X(t_i)-\mu)^2 \tag{3.12}$$

The risk measure of QoI could be mean plus standard deviation.

Maximum:
The absolute maximum is the largest number of a time series. It may be estimated as

$$Max[X] = max(X(t_i)) \tag{3.13}$$

However, for a finite time series, the absolute maximum is not always the same. We will arrive at a higher maximum if we have larger data or longer time series. This makes this QoI troublesome for engineering applications. For this purpose, there are ways to estimate the maximum.

Estimate of the maximum:
An estimate of the maximum is proposed in [80] and is widely used for wind engineering. Here, we fit a Gaussian distribution to the tail of the distribution, and the maximum is estimated as the 80^{th} percentile of the Gaussian distribution.

Value at risk:
The value at risk is also called as a quantile. Let $F_X(x) := P(X \leq x)$ be the CDF of a real-valued random variable X defined on a probability space (Ω, A, P). The value at risk (VaR) of X, at confidence level $0 < \beta < 1$ is defined as

$$\mathrm{VaR}_\beta(X) := \inf\{s \in R : F_X(s) \geq \beta\}. \tag{3.14}$$

This is also known as a β quantile.

Conditional value at risk:
Conditional Value at Risk (CVaR) is defined as the conditional expectation above a quantile. The CVaR of X, at confidence level β, is the expected value of X in the largest $(1-\beta)\cdot 100$ percent of possible events. If $X \in L^1(P)$ and $F_X(x)$ is continuous, then CVaR is the conditional expectation

$$\mathrm{CVaR}_\beta(X) := E[X|X > \mathrm{VaR}_\beta(X)]. \tag{3.15}$$

3.4.2 Details of Conditional value at risk

Here we introduce and use conditional value at risk as a measure of the tail of the distribution for structural wind engineering. This is particularly interesting where the PDF is not symmetric. Two risk measures, the expected value and the conditional value at risk [81, 82] for structural wind engineering, are explored and then used to formulate the optimization objective function later.

From the above definition of CVaR,

$$\lim_{\beta \to 0} \mathrm{CVaR}_\beta(X) = E[X]. \tag{3.16}$$

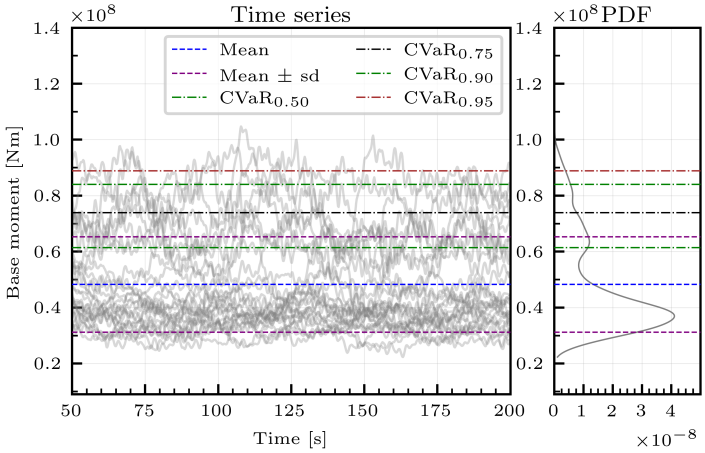

Figure 3.4 : Comparison of the mean, mean ± sd, and conditional value at risk CVaR_β for $\beta = 0.5, 0.75, 0.9, 0.95$ of the base moment $M_{\mathcal{Z}}(t,\xi)$ when $\mathcal{Z} = \mathcal{Z}_0$ in Numerical example 7B 9.4.2.

$\text{CVaR}_\beta(X)$ may also be defined as the solution of a scalar optimization problem [81],

$$\text{CVaR}_\beta(X) = \frac{1}{1-\beta}\int_\beta^1 \text{VaR}_\alpha(X)d\alpha = \inf_{s\in R}\left\{s + \frac{1}{1-\beta}E[(X-s)_+]\right\}, \tag{3.17}$$

where $(x)_+ := \max\{0, x\}$. We use this definition of the CVaR for computations and later in the optimization problem.

The risk measure CVaR has many mathematical properties that are appealing [81–84]. For structural wind engineering purposes, $\text{CVaR}_\beta(X)$ is a more reasonable measure of risk than the mean, variance, or standard deviation because it is a measure that quantifies the weight of the tail of X. Using this risk measure in optimization will allow us to minimize the expected value of limit states that generally cause failure.

In Figure 3.4, we illustrate the mean, variance, and CVaR for the QoI (base moment) $X = M_{\mathcal{Z}}(t,\xi)$ estimated from 30 independent samples of $\xi = (u_*, \theta, z_0, r)$ at the initial design state $z = z_0$ in Numerical example 7b,

presented in Section 9.4. A pseudo-random sampling strategy is used, and the probability density function (PDF) is estimated using kernel density estimation (KDE). It is observed that the distribution of base moment is multi-modal and highly skewed towards large values. Hence, a symmetric measure of risk, like the mean or mean + standard deviation, may not be adequate for decision-making. With this observation, we focus more on risk-averse optimization, where we try to minimize the CVaR of the QoI later in the thesis.

3.4.3 A note on averages

Here, we discuss various notations of averages we use in this thesis. Let u and p represent the fluid velocity and pressure, respectively, and let $X(t) = \varphi(u(t), p(t)) \in R$ be a time-varying QoI like base moment as in Eq. 3.10.

More than one notion of average is used to investigate the random variables. The first is the mean with respect to an invariant probability measure P_t at time t. We assume that $X(t)$: $t \in (0, \infty)$ is a stochastic process, with each sample path $X(t) = X(t;\omega)$ indexed by $\omega \in \Omega$. The average of X, with respect to P_t, at time t, is defined as in Eq. 3.18.

$$\langle X(t) \rangle = \int_{\Omega} X(t;\omega) d P_t(\omega). \tag{3.18}$$

For *statistically stationary* processes, i.e., stochastic processes whose joint cumulative distribution function (CDF) does not change when translated in time, the integral in Eq. 3.18 is constant for all time t. It is often assumed that there is a unique measure $P_\star$ such that $P_t = P_\star$ for all t and, furthermore, that for almost every sample path $X(\cdot, \omega)$, Eq. 3.18 may be rewritten as the (infinite) temporal average. Note that the lower bound, T_1, is arbitrary.

$$\langle X \rangle = \lim_{T \to \infty} \frac{1}{T} \int_{T_1}^{T_1 + T} X(t;\omega) d\, t. \tag{3.19}$$

The validity of Eq. 3.19 is an open problem in most cases, except some special situations [85]. Nevertheless, the *ergodic hypothesis* (i.e.,Eq. 3.19) remains widely accepted in the fluid dynamics community for many problem types and is made use of. In the context of wind engineering, this

assumption means that the statistical properties of wind can be inferred from a single time series of wind at a given location.

To compress the following notation, let's denote $\xi = (u_*, \theta, z_0, r)$ and use $\varrho(\xi)$ to represent the joint probability density function (PDF) of its components. It is clear that the system observables depend on ξ, $X(t) = X(t, \xi)$, or, in other words, for every sample of ξ, a different stochastic process $\{X(t, \xi)\colon t \in (0, \infty)\}$ is encountered. Each sample path in the process is written as $X(t, \xi; \omega)$.

The presence of ξ needs a second notion of average. The mean of $X(t, \xi)$, with respect to the uncertain parameter vector $\xi = (u_*, \theta, z_0, r)$, is determined

$$E\big[X\big] = \int_0^1 \int_{z_L}^{z_R} \int_0^{2\pi} \int_0^{\infty} X(\cdot, \xi)\varrho(\xi) d\, u_* d\, \theta\, d\, z_0 d\, r\,. \tag{3.20}$$

$E\big[X\big](t)$ is a stochastic process in t. Combining the two notions of average, Eq. 3.19, Eq. 3.20, we arrive at what now referred to as the *expected value* of X:

$$E\big[X\big] = E\big[\langle X \rangle\big]. \tag{3.21}$$

To estimate the expected value of observables $X(t, \xi)$, the (finite) temporal average is presented first as,

$$\langle X(\cdot, \xi) \rangle_T = \frac{1}{T} \int_{T_1}^{T_1+T} X(t, \xi) d\, t, \qquad T > 0. \tag{3.22}$$

Secondly, the (finite) ensemble average is presented,

$$E_S\big[X\big] = \frac{1}{N} \sum_{i=1}^{N} X(\cdot, \xi_i), \qquad N = |S| > 0, \tag{3.23}$$

where $S = \{\xi_i\}_{i=1}^N$ is a finite sample set of i.i.d. realizations of the random variable ξ. In this work, the estimator

$$E_S\big[\langle X \rangle_T\big] \approx E[X], \tag{3.24}$$

will be our approximation of choice for estimating Eq. 3.21.

Since the expected value is defined, other statistics can be defined as well. For instance, we define the variance as follows:

$$\mathrm{Var}[X] = E\big[(X - E[X])^2\big], \tag{3.25}$$

and, likewise, the standard deviation $\sigma = \sqrt{\mathrm{Var}[X]}$. The variance and standard deviation measure how spread out realizations of the observable X are to time t and the parameters in ξ. We may use the variance Eq. 3.25 to derive an expression of the variance of the estimator $E_S\big[\langle X\rangle_T\big]$. Indeed, a straightforward computation shows that

$$E\big[(E_S\big[\langle X\rangle_T\big] - E[X])^2\big] = \frac{\mathrm{Var}[\langle X\rangle_T]}{|S|}. \tag{3.26}$$

In general, the numerator $\mathrm{Var}[\langle f\rangle_T]$ will decrease as $T \to \infty$. However, because of the presence of the random vector ξ, $\mathrm{Var}[\langle f\rangle_T]$ cannot be expected to vanish in the $T \to \infty$ limit.

3.4.4 Concluding remarks on the risk measures

Of the various risk measures of the QoI introduced earlier, the building design may be carried out based on the design decision with any of the risk measures. A robust building design should have a low probability of extreme limit states.

A robust building design may have a low variance in a random load X simply because a low variance implies a low probability of extreme X-values. However, directly controlling the variance/standard deviation is not optimal for structural wind engineering as we are interested in only one part of the tail of the distribution.

One significant motivation for seeking alternative risk measures is that $\mathrm{Var}[X]$ penalizes variation both below and above the average $E[X]$. Meanwhile, in typical structural engineering practice, only extreme values on one side of the mean have to be reduced; cf. Figure 3.4. Multiple other drawbacks of optimizing for the variance and standard deviation are discussed in [82].

As an alternative to $\mathrm{Var}[X]$, we consider the conditional value at risk [81, 82] as a risk measure in decision-making. All the failure states are more important than simply controlling the most optimistic failure state. Let's

consider when X can be identified with a stress acting on/within a physical system. Here, lower values of X are generally preferable to higher values of X. Thus, $\text{VaR}_\beta(X)$ represents the most optimistic value that X can achieve in the worst $(1-\beta)\cdot 100$ percent of possible events. Alternatively, $\text{CVaR}_\beta(X)$ represents the expected value of X in the worst $(1-\beta)\cdot 100$ percent of possible events. Hence CVaR is explored s risk measure in this thesis.

Everything should be made as simple as possible, but not simpler.

Albert Einstein

CHAPTER 4

OPTIMIZATION UNDER UNCERTAINTY

Once we accomplish an uncertainty quantification, the next level of complexity would be to optimize considering the uncertainties. An optimization under uncertainties framework for structures under uncertain wind is presented in this chapter. We start off the chapter with a state-of-the-art in civil engineering for OUU. A novel framework for shape optimization considering the uncertainties is presented here. A risk-neutral and risk-averse optimization framework is explored and presented. The problem description and theoretical aspects of optimization under uncertainty for building design are explored. We use a finite difference approach for sensitivities. An adaptive sampling for optimization is proposed to reduce the number of model evaluations. The adaptive sampling is presented in Section 4.4. We apply the proposed framework in wind engineering application later in Chapter 9.

4.1 OUU: state of the art in building design

Wind displays inherent uncertainty in its flows. This is particularly true for the fluctuating component of the wind. Nevertheless, the mean wind velocity and mean wind direction are also associated with uncertainty and can be considered as random variables as in Section 3.2. Similarly, the mean wind profile is associated with uncertainties coming from the influences of the terrain conditions. To reach at a robust and reliable design, the designer needs to take these uncertainties into consideration during analysis [86]. The quantification of these inlet wind conditions is well studied in wind turbine response in the literature [26, 27].

However, uncertainty quantification of tall structures offers room for improvement, and this improved building design process, considering the uncertainties in the wind response of the structure, is presented. The literature does not investigate the stochastic optimization of building geometry under the uncertainties arising from site-specific wind conditions.

This chapter is a comprehensive framework for optimizing structure geometries under the uncertainty of the incoming wind conditions. The global geometric parameters are optimized to reduce the base reaction forces resulting from uncertain wind flows. The geometric change in building structures can be global and local. The local changes generally adopted are corner modifications like stepping, chamfering, and rounding of corners. The most used global geometric modifications are twisting, tapering, adapting the dimensions and shape of an opening, and modifying the size and location of "stepping" features [87]. The proposed optimization workflow can consider all of these geometric modifications. However, focus is given more on the tapering and twisting in numerical examples inspired by the tall building shown in Figure. 4.1. A methodical optimization under uncertainty procedure for designing global geometric features in buildings is developed and presented here.

Given the uncertain nature of the incoming wind, different stochastic optimization problems can be formulated. For example, it is possible to consider a "risk-neutral" optimization formulation, wherein we try to optimize for only the mean of the quantity of interest. Alternatively, a robust optimization can be considered where the objective is to minimize for the mean plus standard deviation [91] or a reliability-based optimization [25] where the reliability is minimized.

Figure 4.1 : Modern tall buildings with unconventional shapes - Absolute World Towers, Mississauga, Canada have an elliptical cross-section with twist along the height [88] (left); (b) F&F tower, Panama has a twist along the height [89] (middle); and (c) 30 St Mary Axe tower, London has a circular dome at the roof [90] (right).

In this thesis, a risk-averse optimization is presented by minimizing the CVaR [81, 83, 84]. Although CVaR is a measure of risk that originally emerged in finance [81], it has been seen in recent years to be reasonable for engineering design applications [82–84, 92]. It is argued in [82] that CVaR is mathematically superior to robust and reliability-based optimization formulations when used to control low-probability events [82, 93, 94]. Focus is given to risk-averse optimization in this thesis, and the results are compared against a risk-neutral optimization problem.

All statistics in the presented optimization workflow are estimated via the Monte Carlo method. A stochastic gradient descent method [95] is used for numerical optimization. A novel adaptive sampling strategy is introduced [92, 96–98] in order to reduce the cost of stochastic optimization. This is very useful since each of the deterministic simulations is computationally expensive.

An elliptical geometry parametrized by fewer design parameters is chosen for the optimization problem. Previous studies that considered uncertainties in the wind do not consider the directionality of wind account. A site-specific design of buildings considering the historical wind data is proposed, including the directionality as elaborated in Section 3.2.2.

4.2 OUU problem formulation

4.2.1 Optimization problems

In this thesis, the following three optimization problems are presented.

$$\min_{\mathcal{Z}\in C}\left\{J(\mathcal{Z}) := E[M_{\mathcal{Z}}]\right\}, \tag{Problem 1}$$

$$\min_{\mathcal{Z}\in C}\left\{J(\mathcal{Z};\beta) := \mathrm{CVaR}_{\beta}[M_{\mathcal{Z}}]\right\}, \tag{Problem 2}$$

$$\min_{\mathcal{Z}\in C}\left\{J(\mathcal{Z}) := \langle M_{\mathcal{Z}}\rangle\right\} \quad \text{subject to } \xi = \xi_{\mathrm{PWD}}. \tag{Problem 3}$$

Where, $\mathcal{Z}$ is the design variable, and C is the design space for optimization. $\beta = 0.90$ unless specified otherwise. ξ_{PWD} denotes $\theta = \theta_{\mathrm{PWD}}$ the predominant wind direction (PWD), and with all remaining wind field parameters at their mean values. The base moment is used as the QoI for the optimization in the numerical example. The optimum of Problem 1 is a *risk neutral* optimum design with the lowest expected value for the QoI. The optimum of Problem 2 is a *risk-averse* optimum design with the lowest 10%-tail expectation of the QoI. The optimum of Problem 3 is a deterministic optimum design that has the lowest time average of the QoI for $\xi = \xi_{\mathrm{PWD}}$. The optimization problem of Problem 3 does not consider uncertainty. In exceptional cases, the optimal designs for all three problems, Problem 1, Problem 2, and Problem 3, can be close to each other. However, for complex geometries and uncertain environments, the resulting optimum designs of all three problems may be quite different; [92].

4.3 OUU workflow based on FD sensitivity

This section describes the gradient-based, iterative, adaptive stochastic optimization algorithm we have employed to solve Problem 1 and Problem 2. The developed OUU algorithm reduces the computational cost of optimization by adapting the number of samples $N = N_k$ in each gradient estimate based on the accuracy of the present design iterate $\mathcal{Z}_k$ analogous to [92, 96–98]. In particular, the accuracy of each gradient is determined by an estimate of its variance.

4.3.1 MC approximation of the objective functions

It is already presented how to approximate $J(\mathcal{Z})$ in Section 3.4.1. By invoking Eq. 3.24, we have that $J(\mathcal{Z}_k) \approx J_{S_k}(\mathcal{Z}_k)$ where $S_k = \{\xi_i\}_{i=1}^{N_k}$,

$$J_{S_k}(\mathcal{Z}_k) = \frac{1}{N_k} \sum_{i=1}^{N_k} J_i(\mathcal{Z}_k), \tag{4.1}$$

and

$$J_i(\mathcal{Z}) = \frac{1}{T} \int_{T_1}^{T_1+T} M_{\mathcal{Z}}(t, \xi_i) dt\,. \tag{4.2}$$

The gradient of the objective function with respect to the design variable at each of the samples, $J_i(\mathcal{Z})$, can be computed via finite differences in the design variable $z \in C \subset R^d$ at the cost of $d+1$ independent CFD simulations. Since the flow is of high Reynold's Number (Re), and is chaotic, an accurate estimate of the gradient for each sample requires a long time interval [99]. The exact length is dependent on the specific problem at hand. Since the flow is chaotic, extra care is taken when selecting an appropriate finite difference increment in each design variable. The empirical mean of sample gradients is an estimate of the gradient of $J(\mathcal{Z})$, namely,

$$\nabla J(\mathcal{Z}_k) \approx \nabla J_{S_k}(\mathcal{Z}_k) = \frac{1}{N_k} \sum_{i=1}^{N_k} \nabla J_i(\mathcal{Z}_k), \tag{4.3}$$

where, ∇ denotes the gradient.

For notational simplicity, let $J(\mathcal{Z})$ denote either $J_1(\mathcal{Z})$ or $J_2(\mathcal{Z})$. At each design iterate $\mathcal{Z}_k$, we choose to approximate $J(\mathcal{Z})$ with a sample average approximation; this is one of the more common procedures used in stochastic optimization [84].

The modifications involved in generalizing Eq. 4.1, 4.3 to the objective function $J(\mathcal{Z};\beta)$ require that we invoke Eq. 3.17 to rewrite

$$J(\mathcal{Z};\beta) = \min_{s \in R} \left\{ s + \frac{1}{1-\beta} E[(M_{\mathcal{Z}} - s)_+] \right\}. \tag{4.4}$$

and note that the optimal values of x on both the left- and right-hand sides coincide. We now define the following generalization of Eq. 4.2:

$$J_i(\mathcal{Z}, s) = \frac{1}{T} \int_{T_1}^{T_1+T} \left(M_{\mathcal{Z}}(t, \xi_i) - s\right)_+ dt\,. \tag{4.5}$$

Then, after defining $s^\star = s^\star(\mathcal{Z}_k, S_k, \beta)$ via the one-dimensional minimization problem

$$s^\star = \underset{s \in R}{\arg\min} \left\{ s + \frac{1}{1-\beta} \frac{1}{N_k} \sum_{i=1}^{N_k} J_i(\mathcal{Z}_k, s) \right\}, \tag{4.6}$$

we approximate $J(\mathcal{Z}_k; \beta) \approx J_{S_k}(\mathcal{Z}_k; \beta)$, as well as its gradient $\nabla J(\mathcal{Z}_k; \beta) \approx \nabla J_{S_k}(\mathcal{Z}_k; \beta)$, as follows:

$$J_{S_k}(\mathcal{Z}_k; \beta) = \frac{1}{N_k} \sum_{i=1}^{N_k} J_i(\mathcal{Z}_k, s^\star), \qquad \nabla J_{S_k}(\mathcal{Z}_k; \beta) = \frac{1}{N_k} \sum_{i=1}^{N_k} \nabla J_i(\mathcal{Z}_k, s^\star). \tag{4.7}$$

As before, we choose to generate the following iterate $\mathcal{Z}_k$ via the standard gradient descent strategy, From now on, for notational simplicity, let $J(\mathcal{Z})$ denote both $J(\mathcal{Z})$ and $J(\mathcal{Z}; \beta)$ in Problem 1 and Problem 2. Likewise, we will write $J_{S_k}(\mathcal{Z})$ for both $J_{S_k}(\mathcal{Z})$ and $J_{S_k}(\mathcal{Z}; \beta)$.

Once the gradients above have been obtained at the current design $\mathcal{Z}_k$, we use the stochastic gradient descent method [95] to determine the next iterate,

$$\mathcal{Z}_{k+1} = \mathcal{Z}_k - \alpha \nabla J_{S_k}(\mathcal{Z}_k), \qquad \alpha > 0\,. \tag{4.8}$$

For greater robustness, efficiency, and computational saving, we select each batch size $N_k = |S_k|$ adaptively based on a posteriori estimate of the statistical error described in [92, 96–98].

Owing to the presence of the non-smooth operator $(\cdot)_+$ in Eq. 4.5, the functions $J_i(\mathcal{Z}, s)$ are not continuously differentiable with respect to z or s. Even though the gradient $\nabla J_i(\mathcal{Z}, s)$ can be computed uniquely at almost every design point x, the non-differentiability can present issues if a naive

gradient descent algorithm is used [81, 83]. However, in our numerical simulations, these issues with gradient descent were not observed, likely because the step size used was small enough that the optimization errors remained lower than other simulation errors. If this is not the case in other problems, it is recommend to replace $(\cdot)_+$ with a smooth approximation; for further details, see, e.g., [83].

4.4 Adaptive sampling

It is observed from Eq. 3.26 that the variance in the gradient estimator $\nabla J_{S_k}(\mathcal{Z}_k)$ is inversely proportional to the batch size $N_k = |S_k|$. Hence, a bigger batch size N_k at each of the stochastic gradient descent iteration Eq. 4.8 results in a high probability of lowering the objective function value, i.e., $J(\mathcal{Z}_{k+1}) < J(\mathcal{Z}_k)$. This will reduce the total number of iterations needed to arrive at the optimal design. However, using a bigger batch size for all optimization iterations is computationally expensive for the number of samples. It turns out that linear convergence can be accomplished by starting with a smaller batch size that increases as $\|\nabla J(\mathcal{Z}_k)\| \to 0$.

This thesis uses an adaptive sampling strategy based on the "norm test" presented in [96, 97] to tune this batch size. The adaptive sampling strategy consists of the subsequent steps. The algorithm starts off with a relatively small batch of samples S_0, and before each successive iteration $k+1$, an evaluation is made if the computed gradient is likely to reduce the objective function or not. If it is judged that the accuracy of the gradient is sufficient, the next batch will have the same size, i.e., $|S_{k+1}| = |S_k|$; otherwise, a larger batch size will be chosen at the next iteration, i.e., $|S_{k+1}| > |S_k|$. In the latter case, the ratio $|S_{k+1}|/|S_k| > 1$ is determined by the "norm test" described below.
The norm test delivers a posteriori control of the variance of the sample gradient $\nabla J_{S_k}(\mathcal{Z}_k)$. It is built around the observation that $\nabla J_{S_k}(\mathcal{Z}_k)$ is a descent direction $\mathcal{Z}_k$, for sufficiently smooth J, if

$$\|\nabla J_{S_k}(\mathcal{Z}_k) - \nabla J(\mathcal{Z}_k)\|^2 \leq \vartheta^2 \|\nabla J_{S_k}(\mathcal{Z}_k)\|^2, \quad \text{for some } \vartheta \in (0,1). \tag{4.9}$$

Computing the left-hand size exactly is infeasible, but if we replace the expression with its expectation, i.e.,

$$E\left[\|\nabla J_{S_k}(\mathcal{Z}_k)-\nabla J(\mathcal{Z}_k)\|^2\right]=\mathrm{Var}(\nabla J_{S_k}(\mathcal{Z}_k))=\frac{\mathrm{Var}(\nabla J_i(\mathcal{Z}_k))}{|S_k|}, \tag{4.10}$$

then it may be accurately estimated. Indeed, the true variance of the gradient samples, $\mathrm{Var}(\nabla J_i(\mathcal{Z}_k))$, can be approximated by the sample variance

$$\mathrm{Var}_{S_k}(\nabla J_i(\mathcal{Z}_k))=\frac{1}{|S_k|-1}\sum_{i=1}^{N_k}\|\nabla J_i(\mathcal{Z}_k)-\nabla J_{S_k}(\mathcal{Z}_k)\|^2. \tag{4.11}$$

Using this expression, we arrive at the norm test:

$$\frac{\mathrm{Var}_{S_k}(\nabla J_i(\mathcal{Z}_k))}{|S_k|}\leq\vartheta^2\|\nabla J_{S_k}(\mathcal{Z}_k)\|^2. \tag{4.12}$$

Algorithm 3 Adaptive sampling algorithm.

1: initial design Z_0, initial sample set S_0, constant $c>0$.
2: Set $k\leftarrow 0$.
3: Repeat
4: **If** convergence test is satisfied
5: compute $d_k=-\nabla J_{S_k}(\mathcal{Z}_k)$
6: choose step size $\alpha_k>0$
7: compute new design iterate: $\mathcal{Z}_{k+1}=\mathcal{Z}_k-\alpha_k d_k$
8: set $k\leftarrow k+1$
9: set $|S_k|=|S_{k-1}|$ and choose a new sample set S_k
10: **Else**
11: update $|S_k|$ using Eq. 4.13 and compute remaining samples

It has been shown that an idealized norm test gives optimal convergence rates for the convex objective function and is robust enough to efficiently deal with many non-convex problems [96, 97].

At an iteration k where Eq. 4.12 is violated, the subsequent batch S_{k+1} is prescribed to have a sample size satisfying

$$|S_{k+1}|=\mathrm{Ceiling}\left[\frac{\mathrm{Var}_{S_k}(\nabla J_i(\mathcal{Z}_k))}{\vartheta^2\|\nabla J_{S_k}(\mathcal{Z}_k)\|^2}\right], \tag{4.13}$$

where Ceiling[·] returns the least integer greater than or equal to its argument. On the other hand, if Eq. 4.12 is satisfied, the next batch size remains unchanged. The entire procedure is summarized in Algorithm 3.

4.5 Concluding remarks on OUU workflow for tall buildings under wind

The main benefit of the adaptive algorithm is that the smaller sample size in initial optimization steps reduces the overall cost and leads to faster progress towards the optimal design. The optimization error dominates in the first steps, and the smaller batch size will not hinder the optimization progress. The sample size grows progressively, allowing the logical growth of samples which keeps the sampling error in line with the optimization error. The chance of oversampling is less as the algorithm adapts to the correct sample size, even for a bad initial guess.

The numerical example of building design considering the workflow elaborated above is presented in Chapter 9. Optimization under uncertainty for structural wind engineering problems is associated with substantial computational costs. However, this effort and computational costs are justified considering the fact that tall buildings are built only once, and the cost of failure is enormous. The building foundation and other structural members are extremely challenging to retrofit due to changes in loading, extreme weather, or design errors. Considering the uncertainties during the design optimization phase will minimize the risks and reduce the possible risk of failures and retrofits.

The only certainty is that
nothing is certain.

Pliny the Elder

CHAPTER 5

UQ IN WIND EFFECTS ON STRUCTURES

The different uncertainty quantification approaches detailed in Chapter 2 are compared against each other here for wind engineering applications with a special focus on structural responses. This chapter discusses the basics of uncertainty quantification for coupled problems and their associated challenges. Various methods used for uncertainty quantification are compared for three numerical examples. Section 5.1 starts with the Monte Carlo method and discusses the practical implementation for the fluid problem in Kratos. Section 5.2 uses the polynomial chaos method based on the collocation approach. Section 5.3 presents the multilevel Monte Carlo method. Observations are made on the method's applicability to structural wind engineering problems. Two problems, one in low Re number and one in high Re number, are presented in this section. Section 5.5 presents and discusses UQ with neural networks and their limitations for practical applications. The efficacy of different UQ methods is presented, and comments are made on the applicability of each of these methods to structural wind engineering.

5.1 Monte Carlo Method

The Monte Carlo simulation method is a sampling method that relies on repeated random sampling from inputs to obtain the stochastic response of the model. The Monte Carlo method is one of the uncertainty quantification approaches that can handle high dimensionality. It is non-intrusive, robust, and simple to implement. Here in this section, MC is used and the implementation described in Section 2.3 for uncertainty quantification for a benchmark fluid problem realized in Kratos Multiphysics.

5.1.1 Numerical example 1A

The widely used DFG flow around cylinder benchmark problem is adopted in the first numerical example [100]. The benchmark simulates a fluid in a pipe with the cylinder in the flow in 2D. The geometry of the problem is shown in Figure 5.1. The fluid density of $\rho = 1.0$ and a kinematic viscosity of $\nu = 0.001$ is used. The upper and lower ends have a no-slip boundary condition. A parabolic velocity profile is applied in the inlet. The readers are referred to [100] for more details on the benchmark example. The inlet boundary condition is,

$$u(0, y) = \frac{4U\, y(0.41 - y)}{0.41^2} \tag{5.1}$$

where U is the maximum velocity at the center. The problem is simulated in Kratos Multiphysics. The Reynolds number of the problem is Re= 20. A fractional step VMS formulation of Navier Stokes equation is used in Kratos Multiphysics. The flow problem is solved and the QoIs are evaluated.

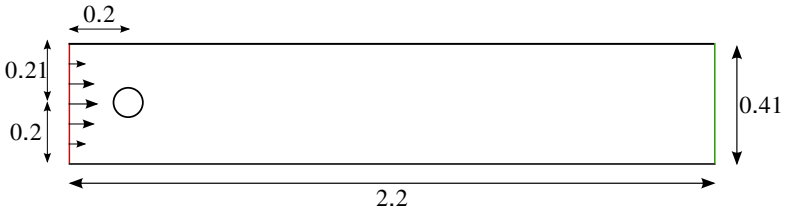

Figure 5.1 : Details of the geometry and boundary condition used in Numerical example 1A

5.1.2 Sources of uncertainty

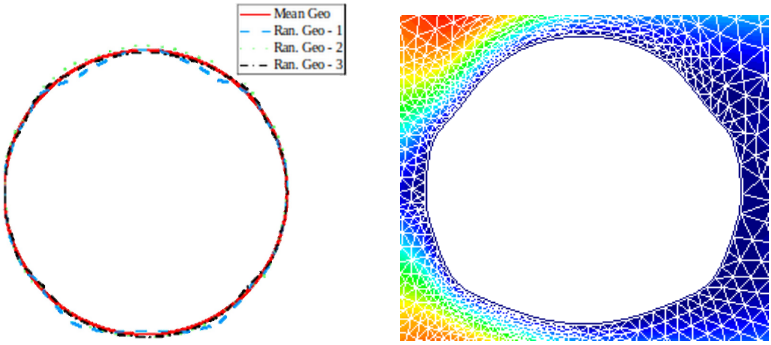

Figure 5.2 : KL expansion used for the random geometry of the structure - Random geometry scaled by a factor of 3 (left); and Random geometry realized in Kratos Multiphysics scaled by a factor of 6 (right).

The geometry of the cylinder is considered uncertain in this study. The geometric uncertainty is motivated from the practical cases of icing in cables or other operational considerations of dusting and wear and tear resulting in uncertain geometry.

The main source of uncertainty is the random geometry of the original circle under flow, which is modeled as a random field. The random field is represented by the Karhunen-Loeve (KL) expansion.

$$Y = Y_{mean} + Y_{pert} \tag{5.2}$$

where Y_{mean} is the original geometry coordinates The perturbations in the Y coordinate Y_{pert} are represented as a KL expansion as

$$Y = Y_{mean} + 0.001 \sum_{i=1}^{m} \sqrt{\lambda_i} \phi_i \xi_i \tag{5.3}$$

where λ_i, ϕ_i are the eigenvalues and the eigenvectors of the covariance function. A Gaussian random field with an exponential covariance function of $e^{-\frac{\Delta Y}{l}}$ is assumed for the KL expansion. A covariance length of $l = 0.05$

is used in the numerical study. The first 8 modes of the KL expansion are considered in Numerical example 1A. The QoI is the time-averaged coefficient of drag. It is important to note that Gaussian random fields are unbounded, which can introduce modeling errors for shape uncertainties. Figure 5.2 depicts the geometric perturbations realized in the CFD solver. They are incorporated in the CDF using a mesh moving strategy in Kratos Multiphysics. The mesh is solved in the first time step, and then by fixing the mesh, the deterministic problem is solved for the perturbed geometry.

5.1.3 Results and discussions

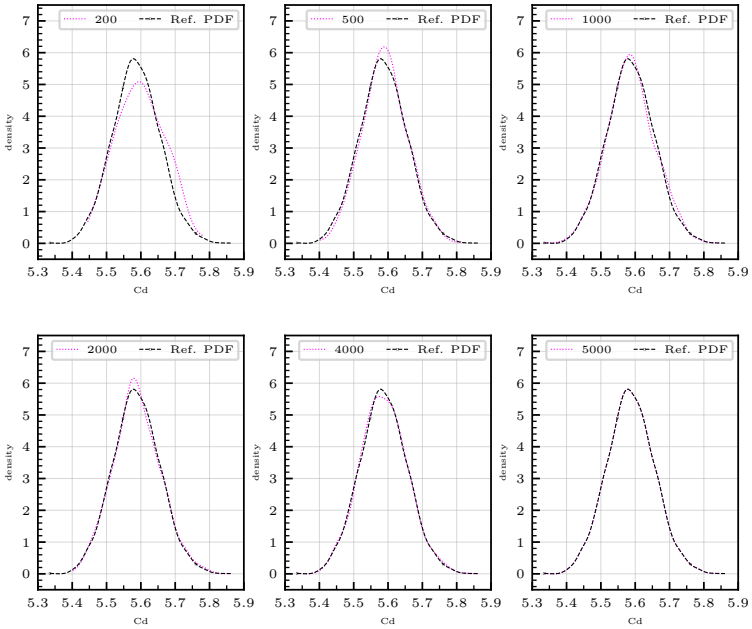

Figure 5.3 : Comparison of PDF of coefficient of drag with increasing number of samples in MC.

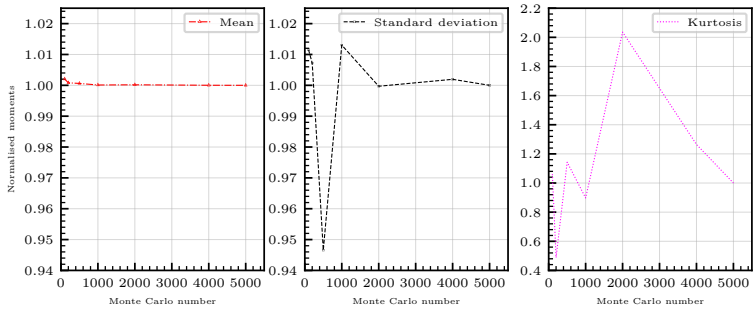

Figure 5.4 : Normalized moments of the coefficient of drag with increasing number of samples in MC.

Uncertainty quantification for the problem described in the previous section is carried out with the algorithm specified in Section 2.3. The quantity of interest is the coefficient of drag, defined as

$$C_d = \frac{2F_d}{\rho u^2 A} \tag{5.4}$$

where, ρ is the mass density of the fluid and u is the average flow velocity at the inlet, and A is the reference area.

Figure 5.3 shows the PDF of C_d as the number of samples is varied. The reference PDF is shown with 5000 samples. It can be seen that the PDF converges to the reference values as the number of samples increases. This shows the large number of MC samples required for the convergence. The PDF is obtained from samples using kernel density estimation. In Figure 5.4, the convergence of mean, standard deviation, and higher orders are plotted against the number of samples. They are normalized with the final value for a better comparison. It can be seen that the mean and standard deviation converges faster compared to higher-order moments.

5.2 PC expansion method

The polynomial chaos method, as explained in Section 2.5, is used for the uncertainty quantification of Numerical example 1A here. The collocation-based approach elaborated in Section 2.3 is adopted in this study.

5.2.1 Numerical example 1A

The same example as used for MC and described in Section 5.1.3 is evaluated with the generalized polynomial chaos method here in this section. A second-order PC expansion denoted as PC 2 is used in this numerical example. The KL expansion is used to model the uncertain inputs. Since the random inputs are Gaussian, a Hermite polynomial is used for the PC expansion as explained in Section 2.5.1. The collocation points are identified as the roots of the basis functions, and the deterministic model is evaluated on these collocation points to obtain the stochastic results. The obtained PDF is shown and compared with the MC results in Figure 5.5.

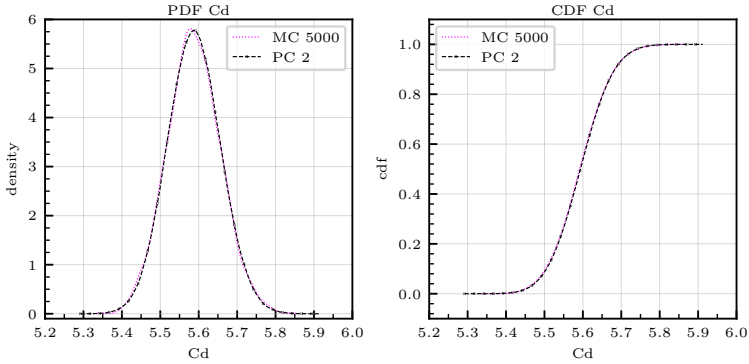

Figure 5.5 : PDF and CDF of coefficient of drag compared with PC and MC

5.2.2 Results and discussions

The PDF and CDF of the coefficient of drag obtained from second-order polynomial chaos expansion (PC 2) are compared with MC simulation

Table 5.1 : Comparison of moments between PC and MC.

	MC 5000	PC 2
Mean	5.5871	5.5880
Standard deviation	0.0690	0.0692
Skewness	0.0916	0.0930
Number of model evaluations	5000	92

with 5000 samples. The results are plotted in Figure 5.5. It can be seen that the PC 2 can accurately capture the stochastic behaviors of the problem at hand. Not only the mean and standard deviation but the PDF and CDF of the QoI are predicted accurately. The mean, standard deviation, and computational cost required are compared for both PC and MC in Table 5.1. It is observed that the PC can capture the stochastic nature of the problem at a fraction of the computational cost.

5.3 Multilevel Monte Carlo methods MLMC

The Multilevel Monte Carlo (MLMC) method is a recent variance reduction technique. The idea of MLMC was introduced and used extensively by [44] and [45]. The goal of MLMC is to decrease the overall computational cost by sampling from a hierarchical system of finite element spaces (levels). All of the FE meshes give a good approximation of the QoI. Now sampling is done from these multi-levels. It is cheaper to compute the QoI in the coarse mesh and is expensive to compute the same in the fine mesh. However, the coarse mesh convergence is slow compared to the fine mesh. The method uses more samples from the coarse grid and fewer samples from the fine grid. The number of samples from each level is inversely proportional to the cost of evaluating the QoI at that level. This strategy allows to get an overall convergence at a lesser cost by sampling from multiple levels of the model, as we have seen in the formulation in Section 2.4

The fluid-structure interaction problem is a complex multi-physics system. In real-world models, the fluid and structural parameters are found to have some inherent variations. These uncertainties in the input param-

eters are taken into consideration in stochastic fluid-structure interaction (SFSI). The Multilevel Monte Carlo method is found to be efficient and is applicable to SFSI problems [101]. SFSI problems, in general, have both fluid and structure parameters that are uncertain. So it should be noted that the coupling variable is also uncertain.

There are, in general, four steps to MLMC for SFSI problems:

1. Creating the hierarchy of discretization
2. Sampling
3. Evaluation of the partitioned FSI problem
4. Determination of the statistics of QoI

Details of each of these steps are presented in detail in Section 5.3.1.

5.3.1 Numerical example 2

Figure 5.6 represents a specific FSI problem of a cylinder kept in flow with the single degree of freedom structural solver in the vertical direction, so as to capture motion induced by vortex shedding in wind engineering. The CFD domain and details are similar to Numerical example 1A.

The problem consists of two subdomains, fluid subdomain Ω_f and structural subdomain Ω_s with their boundaries Γ_f and Γ_s, respectively. The fluid-structure interface Γ_i is given by $\Gamma_i = \Gamma_f \cap \Gamma_s = \Gamma_s$.

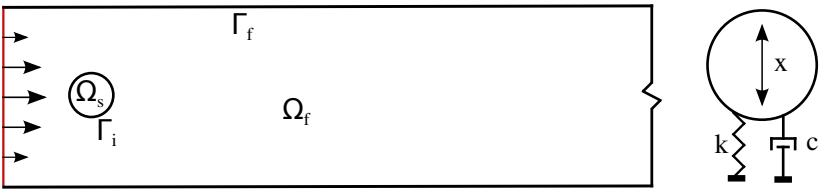

Figure 5.6 : General fluid-structure interaction problem (left); and details of coupling with the SDoF(right).

The governing flow equation, structural equation, and the coupling conditions at the interface for a general FSI problem are briefly explained.

The unsteady flow of an incompressible fluid for domain Ω_f is governed by the conservation of mass and the Navier-Stokes equations, given by

$$\boldsymbol{\nabla} \cdot u = 0 \tag{5.5}$$

$$\frac{\partial u}{\partial t} + u \cdot \nabla u - \nu \nabla^2 u + \frac{1}{\rho} \nabla p = f_f \tag{5.6}$$

for $x \in \Omega_f$. Where u is the velocity, p is the pressure, ν is the kinematic viscosity, and f_f is the external force per unit volume. The deformation u_y of the structure is determined by the conservation of momentum

$$\rho_s \frac{d^2 u_y}{d^2 t} - \nabla \cdot \sigma_s = f_s \tag{5.7}$$

for $x \in \Omega_s$. Where ρ_s represents the density of structure, σ_s the Cauchy stress tensor, and f_s the body forces per structure volume.

The conditions on the fluid-structure interface are the kinematic condition and the dynamic condition.

$$\begin{aligned} u &= \frac{d u_y}{d t} \\ \sigma_f \cdot n_f &= \sigma_s \cdot n_s \end{aligned} \tag{5.8}$$

for $x \in \Gamma_i$, where n_i is the normal unit vector that points outwards from the domain Γ_i.

In the case of strongly coupled partitioned FSI simulation, the interface conditions are ensured at each time step. A Dirichlet-Neumann coupling is used for the current strongly coupled FSI problem. A Dirichlet-Neumann coupling is the type of coupling in which Dirichlet conditions are applied to the fluid domain and the Neumann condition on the structure. In the interface Γ_i from Figure 5.6, let the displacement of the interface be represented by x and the stress on the interface by y. So the fluid solver can be

written as $y = \boldsymbol{F}(x)$ and structural solver as $x = \boldsymbol{S}(y)$. Relaxation schemes are also used to improve the stability and convergence of the iteration. A simple and efficinet way to invoke relaxation is to blend the current solution step with the previous solution step.

$$x^{k+1} = (1 - w^k)x^k + w^k \tilde{x}^{k+1} \tag{5.9}$$

where k denotes the iteration number at each time loop, w is the relaxation factor which is a function of the residual R, and $\tilde{x}^{k+1}$ denotes the structural displacement at the interface calculated by the structural solver at $k+1$ iteration. The partitioned procedure is detailed in Algorithm 4.

Algorithm 4 Partitioned FSI procedure

1: **For** $n = 1$ to N_{end} **Do**
2: Initialise $x^{n,0}$
3: Solve the fluid problem, $y^{n,0} = \boldsymbol{F}(x^{n,0})$
4: Solve the structure problem, $\tilde{x}^{n,0} = \boldsymbol{S}(y^{n,0})$
5: Initialize the residual
6: Apply relaxation as Eq. 5.9
7: Solve the fluid problem, $y^{n,k+1} = \boldsymbol{F}(x^{n,k})$
8: Solve the structure problem, $\tilde{x}^{n,k+1} = \boldsymbol{S}(y^{n,k+1})$
9: Update the residual
10: **If** converged **Then**
11: Go to next time step $n = n+1$
12: **Else**
13: Increase k and go to 6
14: **End if**
15: **End for**

A benchmark example of CFD problem [100] is considered in this study. The uncertainties are considered in both the structure as well as in the fluid parameters. The uncertain input parameters considered are shown in Table 5.2. The fluid problem is coupled with an SDoF solver in the vertical direction so as to capture the vortex-shedding phenomenon. The governing equation of motion of an SDoF system instead of Eq. 5.7 is

$$m\ddot{x} + c\dot{x} + kx = f_s \tag{5.10}$$

Table 5.2 : Details of the input parameters.

Parameter	Mean [mm]	standard deviation
Inlet velocity	1	0.1
Fluid density	0.5	0.05
Kinematic viscosity	0.2	0.02
Mass	0.001	0.0001
Eigen frequency	0.5	-

Table 5.3 : Details of the MLMC grid hierarchy.

Level	Mesh size - circle [mm]	Number of nodes	Computation time [s]
L0	0.01	503	5.02
L1	0.005	1030	10.47
L2	0.002	2000	20.47
L3	0.001	4014	25.83
L4	0.0005	6570	47.15

where m, c, and k are the mass, damping, and stiffness of the system. The mass and eigen frequency are shown in Table 5.2. The stiffness and damping are calculated from the eigen frequency.

Navier-Stokes equation is solved in the open-source platform of Kratos Multiphysics as before. The Single Degree of Freedom (SDoF) solver is solved with a generalized alpha scheme. An Aitken under relaxation is used for the current study. Reynold's number computed for the mean values of the parameter is $Re = 100$. The QoI is the time-averaged drag force coefficient(C_d) of the circular cylinder. The time average is computed from the time when the simulation starts to become oscillatory. The lift coefficient is found to be zero as the motion is periodic.

The deterministic results on each of these meshes are shown in Figure 5.8. The four steps explained in Section 5.3 are elaborated for the given problem. For creating the hierarchy of discretization in the first step, the

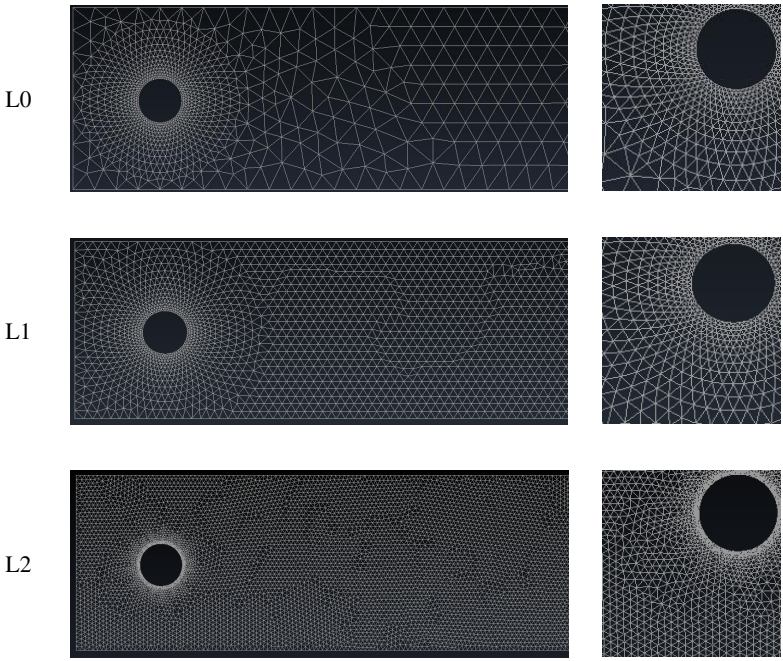

Figure 5.7 : Details of the adopted mesh levels for multilevel Monte Carlo

meshes are non-nested. The fine mesh is decided, and the coarser meshes are developed from the fine mesh by considering larger mesh sizes. The mesh hierarchies in this study are chosen such that the number of nodes approximately doubles at each level. The coarsest mesh should also be able to capture the global flow behavior. The number of nodes, elements, and cost of evaluating the QoI in each of the levels are tabulated in Table 5.3. Figure 5.7 shows the first three mesh levels. The flow fields in each of these mesh level sets are plotted in Figure 5.8. It can be seen that the coarsest level can also capture the global flow behaviors pretty accurately. Now, an initial number of 32 simulations is done at the first three levels to estimate the parameters α, β from Eq. 2.13. Figure 5.9 shows the values obtained by least square regression as α, β and $\gamma = 2$ for the current study.

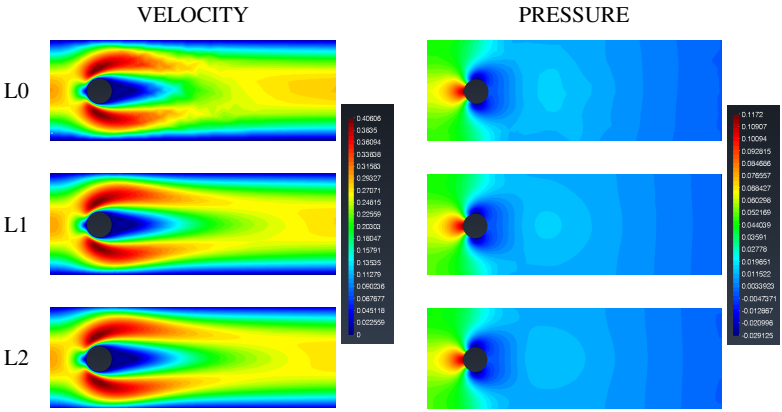

Figure 5.8 : Details of QoI at each of the adopted mesh levels for the mean value of the uncertain parameters.

Both the fluid and structural parameters are assumed to be uncertain. The details of the uncertain input parameters are tabulated in Table 5.2, and the normal distribution is truncated at 3 times the standard deviation. At each level, the samples are taken independently. It should be noted that the same sample is used for the levels l and $l-1$ in Eq. 2.13. A partitioned evaluation of the FSI problem is done in the next step.

The evaluation of the deterministic system is done. The pressure and velocity snapshots are presented in Figure 5.8. The results are collected, and a UQ analysis is done. The results of the same are presented in the next section.

5.3.2 Results and discussions

This section presents and discusses the results of MLMC for fluid-structure interaction problems with uncertain inputs. The MLMC estimator for the coefficient of drag is evaluated for the problem at hand at three different error bounds. The exponent of bounds of cost, variance, and the QoI is determined numerically in the current study. The variance at each level is plotted in Figure 5.9 and is found to be nearly the same for all levels. The difference in variance is found to decrease, implying less number of

samples required at higher levels. The variance of the coarsest level is more compared to other levels.

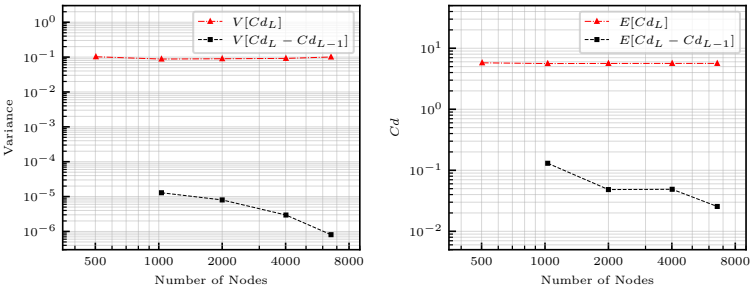

Figure 5.9 : Variance reduction observed for MLMC

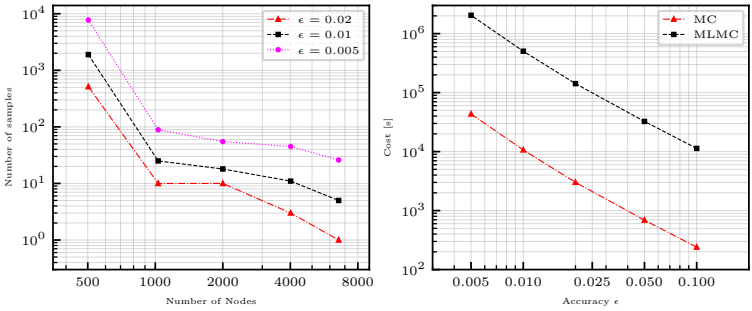

Figure 5.10 : Number of samples required in MLMC for different target accuracies (left); and comparison of cost for MC and MLMC (right)

Therefore most of the samples are drawn from the coarsest level. The number of samples required for each of the levels is plotted in Figure 5.9, and it can be seen that the number of samples reduces as the levels are increased. Most of the samples are drawn from the coarsest level as expected. As the error bound are decreased, the required number of samples increases for all levels. Thus the total cost is increased as error bounds are decreased. Figure 5.11 shows the cost of MLMC compared to MC simu-

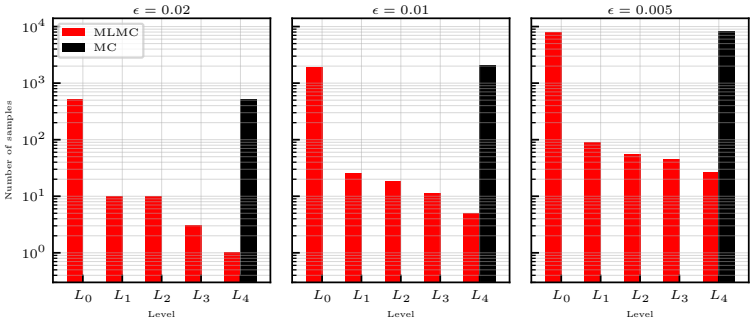

Figure 5.11 : MC v/s MLMC - number of samples required at each level

lations at the finest mesh. The costs are obtained as $N_l C_l$ where C_l is the cost at level l. One can see that the cost of MLMC is less than the MC for all error levels. An average factor of five times saving is obtained for the FSI problem. Setting up the MLMC grid hierarchy and initial computations also contribute to overall cost and effort, which are not accounted for in this cost comparison.

Comparison of computational cost

The cost of standard MC with MLMC is compared. It can be seen from Table 5.4 that a considerable computational saving of up to 8.9 is achieved by adopting the MLMC method. This is done by sampling more from the coarsest level and only running the finest level for a few number samples. The computational gain is shown for all the target error levels. Hence, it can be concluded that the MLMC is promising for UQ in low Re flow structure interaction problems. However, the next section presents more investigations into high Re flows.

5.4 Numerical example 3

The numerical study presented in Numerical example 2 is made to a high Re number problem by making the velocity larger. The inlet velocity of 10m/s is used in this numerical example. Hence, the Re is of the order

Table 5.4 : MLMC comparison of cost with standard MC.

Error	MLMC cost [s]	MC cost [s]	Gain factor
0.1	182	262	3.2
0.05	285	1242	4.4
0.02	1272	11420	8.9
0.01	4465	35100	7.9
0.005	22401	140400	6.3

10^4. It may be seen that the inputs are now varying at higher levels as well. The problem at hand is similar to the previous one. The solution can be computed as explained in Section 5.3.

5.4.1 Results and discussions

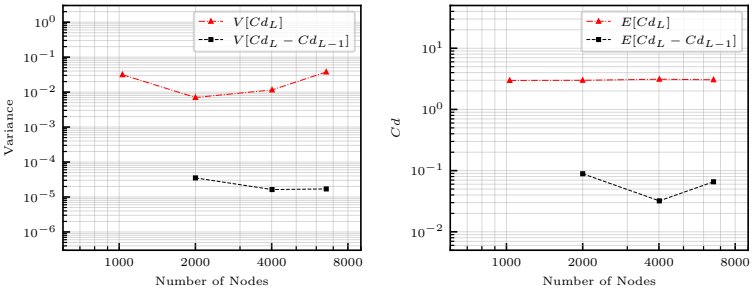

Figure 5.12 : Variance reduction is not observed in MLMC for high Re flows

In order to investigate the flow behavior at high Reynold flows, studies were conducted that measured the convergence versus the interpolation error at different levels of meshes. Figure 5.12 demonstrates the difference of the levels $E[Cd_L - Cd_{L-1}]$ estimated using a sample average over 50 realizations. It can be observed from the figure that geometric decay of this estimate of the difference with fine mesh is not observed. The variation of the variance of the difference is also shown in Figure 5.12. It may also be

noted that this quantity does not decay with the increasing fineness of the mesh.

On further detailed investigation, it was uncovered that bias and variance decay could be challenging to obtain for high Reynolds number flows due to the chaotic nature of the high Re flow. This makes retaining the correlation between fine and coarse samples in an MLMC setting difficult. Hence, the MLMC hypotheses of Section 2.4 are unlikely to be satisfied. These factors make applying MLMC for the target final application in structural wind engineering impossible. The Re in the actual wind flow is of the order of 10^8 and this makes the problem more complex.

5.5 Neural Networks

Neural networks as explained in Section 2.6 are used as a surrogate for uncertainty quantification for a structural wind engineering problem here. As an upcoming and promising field of research this application was explored with a computationally less challenging problem. A physics-informed neural network was also explored collaboratively for uncertainty quantification applications [56].

5.5.1 Numerical example 4

A simplified structural model of the CAARC building is explored in this numerical example. The wind is not modeled in CFD, instead a bluff body definition of the drag coefficient is used here. Knowing the C_d at each cross-section, rectangular in this case, the total force in each section can be found as,

$$F_d(z) = \frac{\rho V(z)^2 A C_d}{2} \tag{5.11}$$

where, ρ is the air density, $V(z)$ is the velocity at height z, A is the reference area and c_d is the coefficient of drag for the cross-section. The structure is modeled as an Euler-Bernoulli beam. The input parameters are tabulated in Table 5.5. A similar geometry to CAARC benchmark building is adopted in this numerical example.

Table 5.5 : Input parameters for the building structure under wind loads

Inputs	Distribution	Values
Natural frequency (f)	-	0.2Hz
Density	-	160 kg/m^3
Damping ratio	-	0.05
Mean wind velocity	Weibull	Mean = 20 m/s, shape parameters = 2
Roughness length	Uniform	[0.1, 0.7]

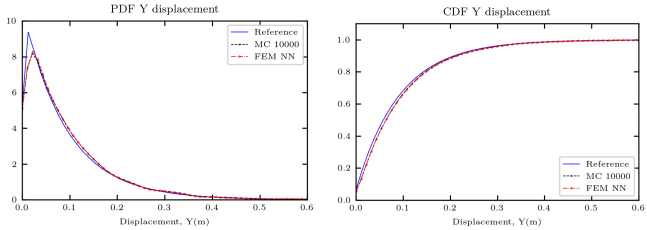

Figure 5.13 : Comparison of NN surrogate with MC PDF (left); and CDF (right) of the top displacement

5.5.2 Results and discussions

The UQ analysis is carried out with the NN surrogate method and MC with 10,000 and reference solution with 100,000 samples. The QoI is the horizontal displacement at the top of the building. The probability density function (PDF) and cumulative density function (CDF) of the QoI are shown in Figure 5.13. It can be seen that the results match each other. To quantify the results better, the first four moments are tabulated in Table 5.6. The error in the mean is less than 0.01% showing a close agreement with the reference results. Other higher-order moments are captured accurately by the method. The deviation in the kurtosis from the reference value may be attributed to the sampling error, as the values of MC 10000 and FEM-NN are comparable.

However, the training time for the Neural network is relatively high compared to the problem at hand. Once the surrogate is created, it is easier to sample from the surrogate. However, the number of training data required is higher compared to other surrogate methods with more mathematical support. Each training point required is also associated with the deterministic evaluation of the underlying model. Hence, creating a good NN surrogate model can be costly during the data creation phase and the training phase. Also, to identify the optimum neural network parameters, hyperparameter tuning may be required, which is also not straightforward and requires computational resources. Hence, due to the complexity of the underlying physics and deterministic problem, it may be concluded that this approach is not the best suited for structural wind engineering.

Table 5.6 : Comparison of moments for NN surrogate with MC.

	Mean	Standard deviation	Skewness	Kurtosis
Reference	0.092774	0.094128	2.08002	6.61567
MC 10,000	0.093232	0.095423	2.20634	8.17860
FEM-NN	0.092765	0.094416	2.22340	8.32967

5.6 Concluding remarks - comparison for FSI

The Monte Carlo method is found to be universal. However, the large number of model evaluations required for the method makes it challenging for wind engineering applications. The variance reduction technique of the Multi-level Monte Carlo method is found to be effective at low Re numbers but is found unsuitable for high Re number flow cases. This makes the method unsuitable for practical structural wind engineering problems. The polynomial surrogate is found to be a good alternative for low-dimensional problems in wind engineering. However, the curse of dimensionality makes it challenging for high-dimensional problems. The NN is found to be computationally expensive for training and data generation for practical structural wind engineering problems. Hence, it will not be explored further in this thesis. The PC and MC will be used going

forward in the thesis for the 'real' wind problem and later in optimization under uncertainties.

An approximate answer to the right problem is worth a good deal more than an exact answer to an approximate problem.

John Tukey

CHAPTER 6

UNCERTAINTY QUANTIFICATION USING GRADIENT ENHANCED POLYNOMIAL CHAOS

Here, in this chapter, the proposed two-step uncertainty quantification using the gradient information is elaborated. The PC expansion we present in Chapter 2 and used for the FSI benchmark example in Chapter 5 is enhanced with the sensitivity information to accelerate the surrogate creation. Also, sensitivity information is used for screening in the beginning to reduce the stochasticity of the problem. Hence, a two-step approach is proposed in this chapter. The proposed method is presented for a numerical study of the cylinder in flow. The computational gain achieved compared to MC and the polynomial chaos approach is demonstrated. The method's applicability to UQ for wind engineering is discussed in the summary of the chapter.

6.1 Introduction to gradient enhanced surrogate models

As elaborated in Section 2.5, surrogate models have been used for simple, efficient relations between input and output parameters. These models are convenient where the deterministic simulations they are based on are computationally expensive, or the data is available from measurements. To infer the relationship between the inputs and outputs is expensive when the number of input stochastic dimensions grows to large numbers and all surrogate models suffer from this shortcoming. It is helpful, in this case, to use all the information available in the deterministic model for surrogate creation. One of the most common and useful pieces of information available in addition to QoI is the gradients. The gradients refer to the sensitivity of outputs with respect to the inputs. By using the gradient information, the number of model evaluations can be reduced for surrogate models. Alternatively, this gradient information can be used to increase the accuracy of the surrogate with the same number of model evaluations. Gradient-enhanced kriging has been used in [102] and shows that the gradient-enhanced version is faster and more accurate. The efficacy of the gradient-enhanced version of the kriging has been shown in various studies [103] [104].

The gradient information for improving the regression in polynomial chaos is used in [105]. Gradient-enhanced polynomial chaos with L_1 minimization for constructing sparse polynomial chaos approach is presented in [106].

6.2 Sensitivity analysis and gradient enhanced polynomial chaos

The sensitivity analysis can be done via different approaches. Direct sensitivity, adjoint approach, and automatic differentiation are the most common approaches.

In the adjoint approach for the time-varying problems, the primal is solved forward in time, while the adjoint is a linear equation solved backward in time. The main advantage of the adjoint approach is that the backward adjoint solves a linear operation, and all the sensitivity information is obtained almost at no additional cost. Kratos Multiphysics has built-in

additional solvers for the computation of adjoint sensitivities for structural and fluid applications. These adjoint solvers are made use of in this thesis.

One drawback, as discussed in the previous chapter, for polynomial chaos surrogates is that the number of collocation points grows rapidly with an increase in input parameters. This can be troublesome for engineering problems with large input parameters that are uncertain since it requires a large number of deterministic evaluations. One way to overcome the curse of dimensionality is to use gradient information to build surrogate models. We propose and use the gradient information for the least square minimization problem and reduce the number of model evaluations. This gradient-enhanced polynomial chaos method is elaborated on in the next section.

Using the adjoint method for evaluating the gradients, the sensitivity information can be obtained at a considerably low additional cost. This sensitivity information is used to reduce the training effort of the polynomial chaos expansion. Figure 6.5 shows the additional computational resources required for the adjoint solves compared to the primal ones in Kratos Multiphysics for the numerical study of consideration. It can be seen that the ratio is around 1.4, and it is independent of the stochastic dimension. This implies that almost all the gradient information at the selected collocation point can be obtained at practically negligible additional cost.

In this thesis, a two-step approach is employed, whereby the number of random input variables is reduced and, hence, solves the curse of dimensionality partially. This dimensionality reduction strategy employed is elaborated and illustrated in detail in Section 6.3.

6.2.1 Formulation of GESC

In the regression approach, the polynomial coefficients are evaluated by solving the least square problem as in Eq. 2.22. Here, in Gradient Enhanced Stochastic Collocation (GESC), we have additional information on gradients at each of the collocation points. Hence, the information matrix can be enhanced to include this information. The Eq. 2.23 then becomes

$$\begin{bmatrix} \Psi_0\left(\boldsymbol{\xi^1}\right) & \cdots & \Psi_P\left(\boldsymbol{\xi^1}\right) \\ \frac{\partial \Psi_0\left(\boldsymbol{\xi^1}\right)}{\partial \xi_1} & \cdots & \frac{\partial \Psi_P\left(\boldsymbol{\xi^1}\right)}{\partial \xi_1} \\ \vdots & & \vdots \\ \frac{\partial \Psi_0\left(\boldsymbol{\xi^1}\right)}{\partial \xi_d} & \cdots & \frac{\partial \Psi_P\left(\boldsymbol{\xi^1}\right)}{\partial \xi_d} \\ \vdots & & \vdots \\ \Psi_0\left(\boldsymbol{\xi^n}\right) & \cdots & \Psi_P\left(\boldsymbol{\xi^n}\right) \\ \frac{\partial \Psi_0\left(\boldsymbol{\xi^n}\right)}{\partial \xi_1} & \cdots & \frac{\partial \Psi_P\left(\boldsymbol{\xi^n}\right)}{\partial \xi_1} \\ \vdots & & \vdots \\ \frac{\partial \Psi_0\left(\boldsymbol{\xi^n}\right)}{\partial \xi_d} & \cdots & \frac{\partial \Psi_P\left(\boldsymbol{\xi^n}\right)}{\partial \xi_d} \end{bmatrix} \begin{Bmatrix} y_0 \\ \vdots \\ y_P \end{Bmatrix} = \begin{Bmatrix} Y^1 \\ \frac{\partial Y^1}{\partial \xi_1} \\ \vdots \\ \frac{\partial Y^1}{\partial \xi_d} \\ \vdots \\ Y^n \\ \frac{\partial Y^n}{\partial \xi_1} \\ \vdots \\ \frac{\partial Y^n}{\partial \xi_d} \end{Bmatrix}. \tag{6.1}$$

The least-square approach requires us to choose the number of collocation points where the deterministic model needs to be evaluated.

6.2.2 Selection of collocation points

As mentioned above, to determine the unknown coefficient y_i, the response of the system (both QoI and the gradients) has to be evaluated at a set of input parameters obtained for specific values of the uncertain random variable, known as the collocation points. For a univariate system, the collocation points are selected as zero, and the roots of one order higher polynomial that is used to approximate the response [52].

If more points are needed, they are chosen in such a way that they are distributed symmetrically around the mean value from the PDF of a random variable. The stochastic collocation method can be easily implemented and leads to solutions easily, even for problems with nonlinearity, much more efficiently compared to intrusive methods.

For multivariate problems, a common methodology adopted is to find the collocation points from the full tensor product space. Since the number of points in the full tensor product grid increases exponentially with the dimension, these grids suffer from the curse of dimensionality. Here, in

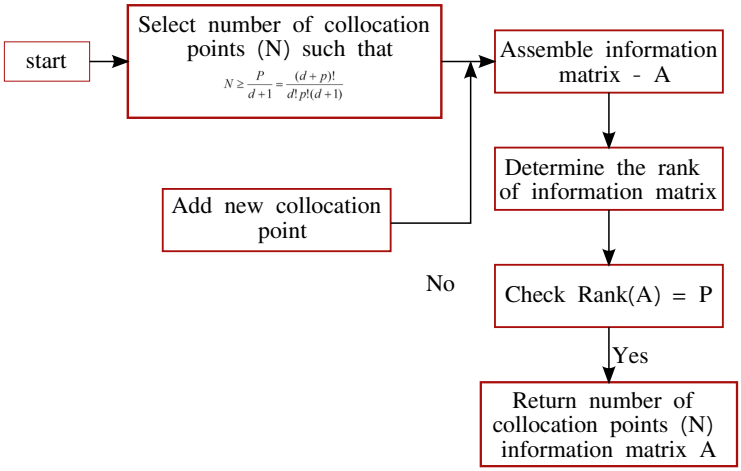

Figure 6.1 : Details of the workflow adopted to choose collocation points in GESC.

this work, we chose the collection points from the full tensor grid such that the rank of the information matrix is more than the rank required as elaborated in [52]. The workflow adopted in this work for the choice of the collocation point is shown in Figure 6.1.

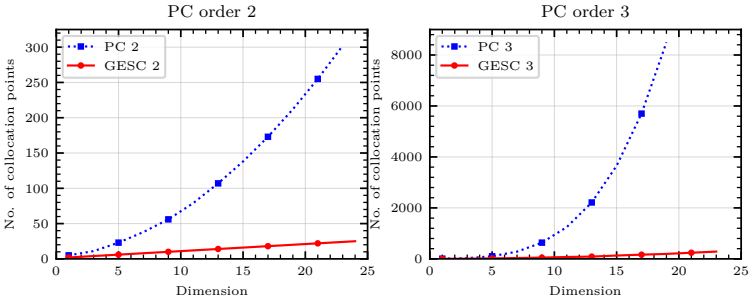

Figure 6.2 : Comparison of cost, the number of collocation points required for PC and GESC

6.2.3 Required computational efforts

The number of collocation points obtained from the above algorithm for different dimensions for the PC and gradient-enhanced version are shown in Figure 6.2. The number of collocation points required increases as the number of dimensions increases in both the PC and GESC. However, for order 2 GESC, the number of collocation points required increases linearly, while for the PC, it increases quadratically. Hence, the difference between the two is clearly evident for higher dimensional problems. For a dimension of 15, the number of collocation points in GESC is approximately 1/15 times the number required for PC. The difference becomes approximately 1/80 th, showing the effectiveness of the method for higher order higher dimensional problems.

6.3 Two-step approach

The proposed two-step approach with dimensionality reduction and basis reduction is elaborated in the following Figure 6.3. The core concept of the two-step approach is to make a pre-selection of the important inputs in step 1 and then only consider the uncertainties of the important parameters in the analysis for GESC in step 2. The first step is to do a sensitivity analysis of the mean parameters and sort the parameters based on their importance. We make three categories of inputs. High-importance parameters, medium-importance parameters, and low-importance parameters. The high-importance parameters have larger impacts on the outputs. Hence, they are included in the UQ analysis. The low-importance parameters are neglected since they have lower sensitivity values. This results in a reduction of the overall dimensionality of the stochastic space. The reduction of dimensionality is of prime importance for surrogate construction since the resulting problem is of lower dimension, and hence, a lower number of collocation points are required in the UQ analysis. A basis reduction is proposed for the medium-importance parameters. The higher-order terms of the medium-importance parameters are neglected from the PC expansion, resulting in a basis reduction. This will also result in a reduced number of collocation points. After the first step, the number of PC terms is reduced. It can be seen that the dimensionality reduction and basis reduction dramatically reduce the computational cost. This is clearly justified in the numerical example shown below. The choice of the

sensitivity thresholds for categorizing the input parameters needs to be made by the user. This choice has a major role to play since we make a dimensionality reduction based on this categorization. However, the existence of medium-importance parameters will still include the lower-order PC terms of those parameters even if the threshold for high-importance parameters is too large.

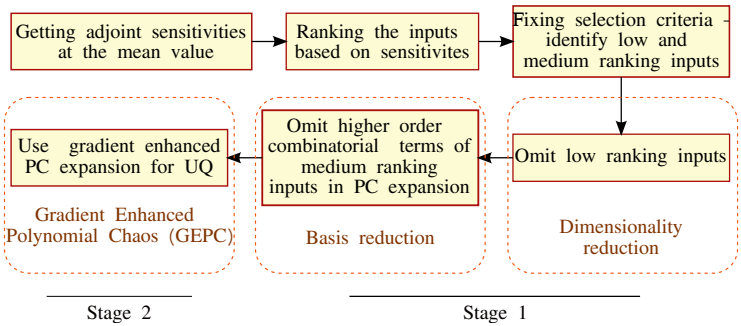

Figure 6.3 : Details of the two-step approach elaborating the various steps.

6.4 Numerical study

The gradient-enhanced polynomial chaos and the two-step approach are applied to the cylinder in the flow problem we elaborated on in Section 5.1. The Numerical example 1A is explored with GESC, and a comparison is made with GESC, PC, and MC approaches. The accuracy and computational costs are compared and commented on.

6.4.1 Uncertain geometry description

The uncertain geometry is modeled with a KL expansion. The details of KL expansion and parameters are described in section 5.1. Two numerical examples are introduced here. Numerical example 1A with a correlation length, $l = 0.05$, and Numerical example 1B with a correlation length, $l = 0.02$. In Figure 6.4, we plot the weighted eigenvalues and average variance error against the number of modes in the KL expansion. For an average variance error of 5% we choose the number of modes as 8 and 20

for Numerical example 1A and 1B, respectively. It can also be seen that the weighted eigenvalues are also very low for these mode numbers chosen to truncate the KL expansion. Hence, Numerical example 1A has 8 dimensions, and 1B has 20 dimensions. We show the GESC approach for Numerical example 1A and the two-step approach for Numerical example 1B since it is a high-dimensional problem.

The uncertain geometry realized in Kratos via mesh motion solver is shown in Figure 5.2. The uncertain geometry definition may be found in Section 5.1.

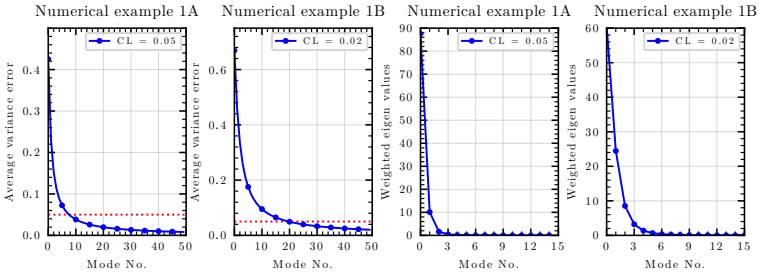

Figure 6.4 : Choice of the number of modes in the KL expansion for Numerical example 1A and Numerical example 1B.

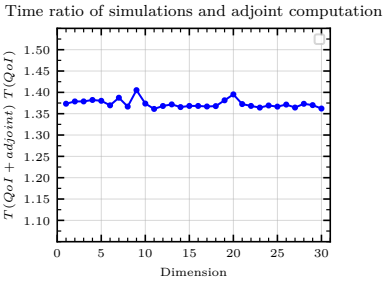

Figure 6.5 : Computational cost required additionally for sensitivity evaluation with varying stochastic dimensions.

6.4.2 Quantities of interest and their sensitivities

The QoI is the time-averaged drag coefficient as in Eq. 5.4. The input uncertainties are in the geometry of the circle. The Reynolds number considered is 20 and hence the flow is laminar. An adjoint approach is used to compute the sensitivities. Figure 6.6 shows the time average pressure, adjoint pressure, and drag sensitivities with respect to the nodes. The drag sensitivities are larger at the extreme vertical points, as expected. The additional computational time required in our implementation for the calculation of sensitivity for varying stochastic dimensions is shown in Figure 6.5. It is observed that for adjoint sensitivities, the additional effort required is 40% more than the QoI alone. However, this factor is found to be almost the same for all the dimensions. This gradient information obtained at a small additional cost for a higher dimensional UQ problem is used for the two-step approach to result in a computationally efficient forward propagation of uncertainties.

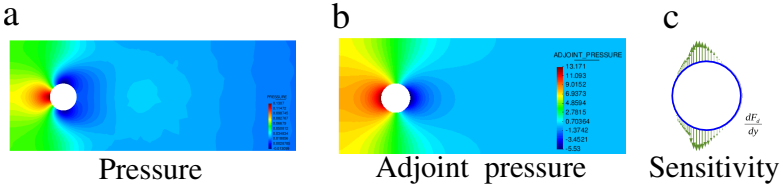

Figure 6.6 : Sensitivities with respect to nodal coordinates for cylinder in flow problem evaluated with Kratos Multiphysics.

6.4.3 Numerical example 1A - Results and discussion

The uncertainties of the geometry are quantified using GESC elaborated in Section 6.2.1 and the results are quantified here. The moments of the QoI for the PC, MC, and GESC are tabulated in Table 6.1. It can be seen that the first two moments match really well for all three approaches. However, the third moment differs significantly. The GESC requires only 0.47% of effort compared to MC. This improved performance at the cost of accuracy in higher-order moments is a justifiable compromise. The computational time required for the GESC approach is 25% of the computational time required for PC. There is also an additional cost of computing sensitivities using the adjoint approach in GESC. This 75% computational saving with

Table 6.1 : Comparison of moments for GESC, PC, and MC.

	MC 5000	PC 2	GESC 2
Mean	5.5871	5.5880	5.5881
Standard deviation	0.0690	0.0692	0.0735
Skewness	0.0916	0.0930	0.0274
Number of model evaluations	5000	92	11
Computation time (s)	145000	2678	687
Computation time (%)	100	1.85	0.47

comparable accuracy in moments shows the applicability of the gradient-enhanced polynomial chaos. The PDF and CDF of the QoI for all three approaches are also plotted in Figure 6.7. It can be seen that the GESC is able to predict the mean and standard deviation pretty accurately compared to PC and MC at a fraction of the cost, as inferred in Table 6.1. The higher-order moments, like the skewness, are observed to have larger errors.

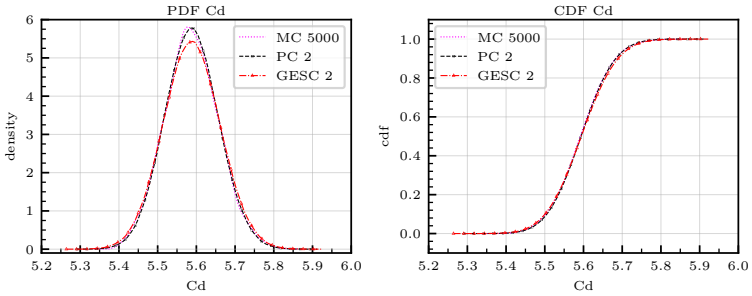

Figure 6.7 : PDF and CDF of coefficient of drag evaluated with GESC, PC, and MC.

6.4.4 Numerical example 1B - Results and discussions

For the covariance length of $l = 0.02$ we have a 20-dimensional problem as shown in Figure 6.4. Here, the two-step approach described in Section 6.3

Table 6.2 : Identification of high, medium, and low importance parameters based on normalized sensitivities.

mode no.	Normalized sensitivities	Sum of normalized sensitivities	
1	0.55	0.55	High
2	0.14	0.69	
4	0.12	0.81	
3	0.12	0.92	
6	0.04	0.97	Medium
8	0.01	0.98	
5	0.01	0.99	
10	0.00	0.99	
12	0.00	0.99	
14	0.00	0.99	
...	...	...	low

is used. A threshold is set for medium and high dimensions, and the identifications are based on their local sensitivities at the mean values. This is shown in Table 6.2.

Once the modes are sorted, the dimensionality reduction is applied and the basis reduction is done as before. The stochastic analysis is carried out and compared in Table 6.3 and Figure 6.8. It can be observed that the two-step approach is able to capture the first two moments pretty accurately at a reduced cost of 30% compared to GESC, showing the effectiveness of the two-step approach. The deviation in the skewness is also observed here similar to Numeical example 1A.

6.4.5 Two-step approach - results and discussion

For the Two-step approach, the surrogate for the full basis and the reduced basis with GESC are tabulated in Table 6.3 and plotted in Figure 6.8. It can be seen that they match really well, and the observables are predicted very accurately. This shows the efficacy of the proposed two-step approach for

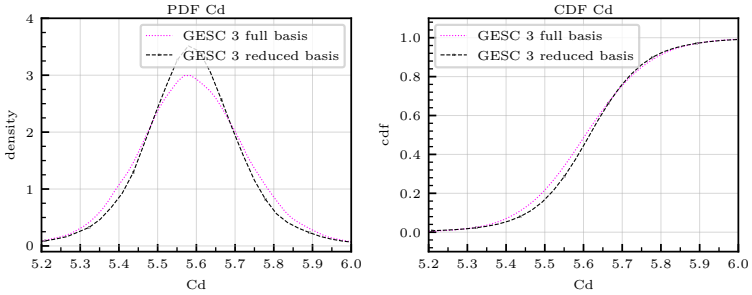

Figure 6.8 : Comparison of PDF and CDF between GESC and two-step approach.

forward propagation of uncertainties. However, the higher moments were not captured with higher accuracy in the reduced basis model.

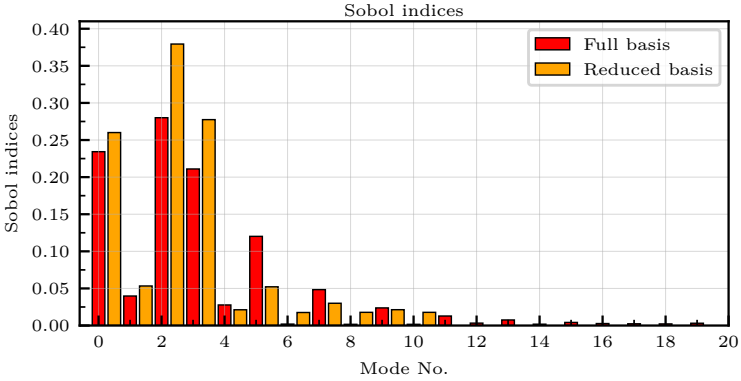

Figure 6.9 : Comparison of Sobol'indices between GESC and two-step approach.

6.4.6 Comparison of computational effort

Figure 6.10 shows how efficient the GESC is for each step. It can be seen that the major saving is from the dimensionality reduction. Extra savings

Table 6.3 : Comparison of moments between GESC and two-step approach.

	GESC.	two-step approach	% difference
Mean	5.5908	5.5880	0.19
STD	0.1439	0.1387	3.613
Skewness	0.1047	0.0327	68.7
Numer of model evaluation	241	74	30

in computation are obtained from the basis reduction. It can be clearly observed that the two-step approach is an efficient way to build a surrogate for the problem where sensitivity information is available.

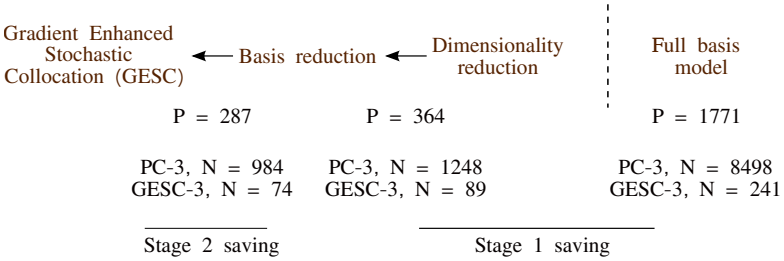

*P is the number of PC coefficients and N is the number of model evaluations required

Figure 6.10 : Details of the computational savings achieved using the two-step approach and GESC.

6.4.7 Challenges for application to full-scale wind scenario

We show that the gradient-enhanced polynomial chaos with a pre-selection (two-step) approach is a computationally efficient way to build a surrogate for uncertainty quantification. However, the major challenge is to have local sensitivity information available for all the quantities of interest with respect to all the input parameters under consideration. This may require modifying the existing adjoint element formulations or writing new ones. The adjoint information may not be available in commercial codes for all the QoI with respect to inputs of interest. This is a major challenge when it comes to the applicability of the method. Also, the sensitivity evaluation

for Navier-Stokes is found to diverge for high Reynolds numbers due to the chaotic inherent nature of the flow problem and butterfly effect. We do not have sensitivity information available for high Re flows that are of interest to practitioners in this thesis, hence, even though the method is promising, it will not be used for the showcase example of wind flow around the building as in Chapter 8.

"Prediction is very difficult, especially if it is about the future"

Niels Bohr

CHAPTER 7

VERIFICATION AND VALIDATION IN WIND EFFECTS ON TALL BUILDING

The first step of uncertainty quantification is to get a good deterministic model representative of the physics as elaborated in Figure 2.1. Verification and validation ensure the quality of the deterministic simulation and the correctness of the solution to the deterministic problem. Here in this chapter, the various verification and validation methods are explored for structural wind engineering. A numerical example of a well-known CAARC benchmark building is demonstrated, and the validation of the numerical wind tunnel for this benchmark structure is carried out, ensuring the quality of the deterministic simulation used for uncertainty quantification in Chapter 8.

7.1 Verification and Validation

The basic terminology and concept of verification and validation in the context of computational structural wind engineering problems are de-

scribed here. The verification and validation concept is widely popular in the computational fluid dynamics community [107]. In scientific computing and simulation, a modeler primarily tries to model reality with computer models developed based on the conceptual model and uses the available computational resources to predict the quantities of interest. These predictions are about the real world. The conceptual model is developed from the theory and mathematical formulation of the real world based on the physics of the real-world problem. The conceptual model consists of all the information, mathematical formulation, and mathematical equations that describe the physics of the real-world problem at hand. In CWE, the conceptual model includes a mathematical description of the physics of the fluid domain and structural domain and the coupling between these two. The partial differential equation (PDE) describing the two physics and the coupling strategy is the basic building block of the conceptual model. The auxiliary equations, like the turbulence model, the initial conditions, the boundary conditions, etc., are also part of the conceptual model. A computational model is the computer implementation of the conceptual model. The computational model also referred to as the computer model or code, is operational and solves the PDEs described in the conceptual model to result in numerical values of the output QoI.

Verification and validation ensure the accuracy of these two, conceptual and computer models and ultimately ensure the accuracy of the prediction of the quantity of interest. The American Institute of Aeronautics and Astronautics (AIAA) definitions of verification and validation are as follows [107]

> "Verification: the process of determining that a model implementation accurately represents the developer's conceptual description of the model and the solution to the model.
>
> Validation: The process of determining the degree to which a model is an accurate representation of the real world from the perspective of the intended uses of the model."

For structural wind engineering, verification provides a confirmation that the computer model/code correctly implements the fluid and structural physics and that the implementation solves the equation correctly. This step does not have any role to play in the real-world application of

the problem, whereas validation offers an idea of how accurately the computational model and simulation represent reality. Validation is a check of how much the prediction and the reality are in consensus with each other. Verification is assessing if the equation is solved right, whereas validation is assessing if the right equation is being solved [108]. There are two steps in verification. The first is code verification, and the second is solution verification. Code verification refers to ensuring the computational code tests are implemented and are functioning as intended, whereas solution verification ensures the computational models give the correct results for the benchmark test problems. Code verification aims at uncovering the bugs in the code, checking computed results against benchmark problems with known solutions, and assessing the performance of the algorithm. Solution verification amounts to producing a posteriori error estimate for the output QoIs. Verification will not be looked upon in much detail in this thesis. Refer to this thesis [109] for details on solutions and code verifications in Kratos Multiphysics. The validation of the fluid and structural code for the SWE application is also explored in [109] with CAARC benchmark as a showcase example. The focus is on validation methodology and uncertainty quantification in the rest of the chapter.

7.1.1 Validation

As the AIAA guide defines, validation is the process of determining how much a model is an accurate representation of the real world from the perspective of the intended use of the model [107]. In SWE, hence, validation deals with the assessment of the comparison between computational results and experimental data from measurements. The measurements may be done scaled down on a wind tunnel or on real scale for a few benchmark cases. Validation does not explicitly answer how the computational model may be changed to improve the agreement between the computational result and the experimental measurements. It only shows how much agreement there is between the two.

In many cases, for structural wind engineering, it is not possible to conduct validation experiments on the complete system due to the complexity of the problem. As elaborated in Chapter 1, the structure we analyze may be unique and, in many cases, not built yet, making a full-scale validation impossible. Also, not all the cases may not be possible to model in

wind tunnels. This is particularly true for scaled-down aero-elastic models. In these cases, a hierarchy approach is used in which the SWE model is subdivided into simpler subdomains. Validation tests are done, and the results are compared for the computational and experimental results for the subsystems, benchmark cases, or unit problems. It may be noted here that individual computational outcomes of a model are validated, and codes/models are not validated [108]. Hence, promising data for an individual outcome of one validation experiment does not ensure that the entire SWE model is validated. However, these validation experiments give overall confidence in the predictions made from the computational models, showing that the model has achieved a given level of accuracy in solving the specific problem at hand for a specific QoI.

The basic approach of validation involves the identification and quantification of the error and uncertainty in the conceptual and computational models, estimation of the numerical error in the computational implementation, estimation of the experimental error, and checking how much agreement is there between the computational prediction and the experimental measurement.

Error in experiments and simulation

The different sources of error in a computer simulation are discussed by [110]. Error in the simulation E_{sim} is defined by

$$\begin{aligned} E_{\text{sim}} &= y_{\text{sim}} - y_{\text{real-world}} \\ &= (y_{\text{sim}} - y_{\text{computer}}) + (y_{\text{computer}} - y_{\text{model}}) \\ &\quad + (y_{\text{model}} - y_{\text{exp}}) + (y_{\text{exp}} - y_{\text{real-world}}) \\ &= E_1 + E_2 + E_3 + E_4 \end{aligned} \tag{7.1}$$

where, y_{computer} is the QoI that could be theoretically computed on a flawless computer with unlimited speed, precision, and memory. Hence, E_1 denotes numerical error resulting from the discrete solution and the perfect computer solution. It is, hence, a solution or calculation error. These types of errors can be minimized by solution verification procedures.

E_2 symbolizes the error due to the algorithm and is handled by the code verification process. E_3 depicts the error that arises from the difference

between the mathematical model and the experimental measurement, referred to as the model error. The computation of E_3 is more challenging than E_1 and E_2 since experimental measurements are always associated with uncertainties. For example, the same wind tunnel experiment repeated at different times or in different facilities will deliver slightly different results. Another problem with experimental measurement is that they also provide the necessary input data for the simulation model. The boundary conditions, initial conditions, excitation measurements, etc., depend on these uncertain measurements. This may result in E_3 becoming a closed loop.

E_4 shows the errors due to the difference between the true value of the real world and the measurement of the quantity of interest. This is referred to as an experimental error. The true value from the real world is seldom deterministic, as in most cases, especially in wind engineering problems, the reproduction of the exact same physical condition cannot be accomplished from one realization to the next. It is interesting to note that a zero total error does not mean the errors E_1 to E_4 are all zeros. An error of one term can cancel out the error of the other term and result in the total error becoming zero.

An estimate of E_1 and E_2 is obtained through verification, and an estimate of E_3 and E_4 is obtained through validation. Hence, it is important to do verification and validation so that not only an idea of the total error can be obtained, but also an estimate of the individual terms can be made. Hence, an informed decision about the trustworthiness of predictions from computational models can be made.

7.1.2 Validation metric

The concept of validation metrics originated from the requirement of a mathematical operator that calculates the difference between the prediction of scientific computing and the experimental measurement in a validation scenario. Validation metric is defined in [111] as a mathematical operator that measures the difference between a system response quantities obtained from a simulation result and one obtained from experimental measurements. The validation metric is used as an objective measure of the distance in some sense between prediction and experimental measurement. The validation metric is, hence, a non-negative quantity.

Hypothesis testing is used traditionally for model validation. In hypothesis testing, the model is tested for a large number of trials to see if it meets the hypothesis test condition to desired statistical accuracy. If the hypothesis is satisfied, the computational model is said to be validated, and if not, the model is invalidated. This approach gives the idea that the model passes or fails a particular hypothesis and is not a qualitative measure. Another simplified approach used is a comparison of the mean values. This approach compares the mean values of the experimental and the simulation results. In literature [112–114] the vector norms, L_1 and L_2 norms, have been used as validation matrices. This method focuses only on specific statistical quantities other than the whole probability distribution of the parameter. In many previous studies, even the uncertainty propagation through the model has not been executed.

7.1.3 Comparison of probability distributions and p-boxes

In a non-deterministic study, the validation metric is the difference between the probability distribution of the experiment and the simulation. A useful tool for this comparison for the validation exercise is based on comparing the shapes of the cumulative density function (CDF) of the two distributions [115]. The uncertainty of the system can be purely aleatory or mixed (a combination of aleatory and epistemic). In cases where the uncertainty is purely aleatory, the probability measure will be a CDF, and in cases where there is an interval estimate of the parameters of the probability density function, the probability measure will be a p-box. A detailed description of the comparison of shapes of CDF and p-boxes for validation exercise is available in [115].

A method of propagation of P-boxes through the system using a sparse polynomial chaos approach is presented in [116]. In the study, the parameter uncertainty is considered as p-boxes. Both the aleatory and epistemic uncertainty of the input parameters are considered. The algorithm is based on the polynomial chaos approach. A mathematical model considering the quantified uncertainties is close to a real scenario. A brief review of computer predictions with quantified uncertainty is presented in [117], where the use of uncertainty quantification for validation is emphasized.

A comprehensive framework for verification, validation, and uncertainty quantification in scientific computing is presented in [111]. The val-

idation metric explained above is extended to a framework. Both aleatory and epistemic uncertainty are addressed in the framework. In cases where both epistemic and aleatory uncertainties are present, the concept of probability box (p-box) is used. Key steps for validation are presented, and an example of a hypersonic nozzle flow was presented for better understanding in [111].

In the upcoming section, we validate the CFD solver used by Kratos Multiphysics using the well-studied and documented benchmark case, Commonwealth Advisory Aeronautical Council (CAARC) benchmark building B [21]. The results are compared with published studies, and we explore the validation metric in this benchmark example to ensure the quality of our deterministic simulation.

7.2 Validation of the CAARC building B

The validation of the well-documented benchmark CAARC benchmark building B will be carried out and presented in this section. Kratos Multiphysics is used in the current study to model the wind effects on benchmark tall building. The building geometry is modeled at full scale, even though many experimental and few numerical studies have done scaled-down testing. This benchmark example will then later be used for the UQ task in Chapter 8. It is important to make sure the physics is solved correctly before doing the UQ task as elaborated in Section 7.1.1.

Building B of the CAARC benchmark study has been widely researched and simulated in CWE and CFD in the past [16, 17, 21, 23]. The benchmark building B of CAARC has a classical bluff body shape with a flat top and rectangular cross-section. The lateral surfaces are also flat without any parapets or additional geometric features. The simplicity of the geometry makes it a perfect choice for a benchmark case. The plan dimensions are 45 m x 30 m. The height of the benchmark building is 180 m.

7.2.1 Details of reference measurements

Previous investigations have been conducted both in the wind tunnel and using CFD for the CAARC benchmark building B [16, 17, 21, 23]. Among these studies, we use the numerical study on the aerodynamic and aeroelastic response of CAARC building B from [22]. The study also compares

its results with previous studies and all these results are made use of in the validation. We refer to [22] for reference values for validation of the CFD model in Kratos Multiphysics.

The quantity of interest reported in [22] are the pressure coefficients at the height of 2/3 of the total height and the force and moment coefficients at the base. All these coefficients are normalized quantities to the free stream velocity. This makes the setting up of the CFD and validation easier.

The pressure coefficient at any point is the normalized pressure with free stream velocity described as

$$C_{P_i} = \frac{P_i - P_0}{1/2\rho V_H^2}. \tag{7.2}$$

The force and moment coefficients are found from the shear force and moments at the base by normalizing with respect to the free stream velocity as,

$$\begin{aligned}
C_{F_X} &= \frac{\sum_{i=1}^{NTN} F_{X_i}}{1/2\rho V_H^2 WH}; \quad C_{\sigma F_X} = \frac{\sum_{i=1}^{NTN} \sigma F_{X_i}}{1/2\rho V_H^2 WH} \\
C_{F_Y} &= \frac{\sum_{i=1}^{NTN} F_{Y_i}}{1/2\rho V_H^2 WH}; \quad C_{\sigma F_Y} = \frac{\sum_{i=1}^{NTN} \sigma F_{Y_i}}{1/2\rho V_H^2 WH} \\
C_{M_X} &= \frac{\sum_{i=1}^{NTN} M_{X_i}}{1/2\rho V_H^2 WH^2}; \quad C_{\sigma M_X} = \frac{\sum_{i=1}^{NTN} \sigma M_{X_i}}{1/2\rho V_H^2 WH^2} \\
C_{M_Y} &= \frac{\sum_{i=1}^{NTN} M_{Y_i}}{1/2\rho V_H^2 WH^2}; \quad C_{\sigma M_Y} = \frac{\sum_{i=1}^{NTN} \sigma M_{Y_i}}{1/2\rho V_H^2 WH^2}
\end{aligned} \tag{7.3}$$

where, ρ is the density of the air, V_H is the velocity at height H, and W is the building width. C_{F_X} represents the force coefficients in the direction X and M_{F_X} is the moment coefficient. $C_{\sigma F_X}$ represents the root mean square of the fluctuation of F_X.

7.2.2 Setting up of numerical simulation in Kratos

As elaborated earlier, we conducted the numerical simulation to model the wind flow around the rectangular CAARC building B model with Kratos Multiphysics. The fluid properties are listed in Table 7.1. The high Reynolds

number in the present simulation causes the flow to be extremely turbulent.

A finite element method formulation for flow problems based upon a variational multi-scale (VMS) formulation [118] is used. The fluid domain is discretized with fractional step elements. Figure 7.1 shows the computational domain setup adopted in the current simulation. The boundaries of the fluid domain and the applied boundary conditions are also depicted in the figure.

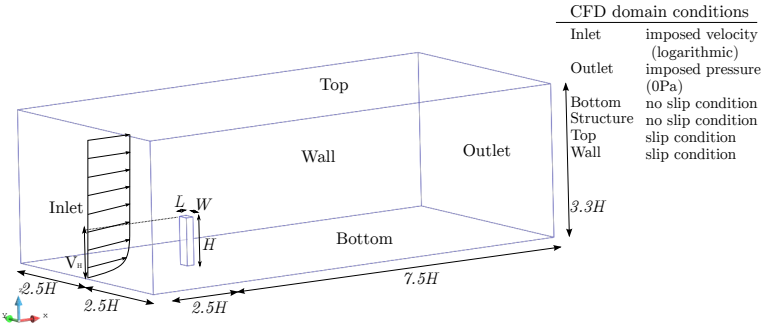

Figure 7.1 : Details of the CFD simulation domain and boundary conditions.

Table 7.1 : Fluid properties and problem data for CAARC simulation in Kratos Multiphysics.

Parameter	Value
Density $\rho[Kg/m^3]$	1.225
Viscosity $\mu[m^2/s]$	$1.507E^{-05}$
Dynamic viscosity ν [Kg/m s]	$1.846E^{-05}$
Characteristic length w [m]	45
Reynolds number Re	$9.7E^{07}$

Boundary condition at the inlet

A steady inlet condition is used in the simulation, similar to the original study. The wind inlet does not change with respect to time, however the profile varies over the height. A logarithmic profile is adopted here as elaborated in Section 3.2.1, in contrast to an exponential profile in the original study [22].

In the current study, a corrected logarithmic profile as Eq. 3.4 is adopted. In practice, the wind measurements are carried out at a reference height and for a duration of 10 minutes (600s).

The mean velocity of 40 m/s as in [22] at a reference height of 180 m is used in the inlet boundary. The roughness length value of 2 m is chosen for the logarithmic profile so that both the adopted wind profile and the exponential profile with an exponent of 0.3 as defined in [21] are in good agreement.

7.2.3 Validation of the CFD results

The results of the CDF simulation are compared with the previous literature [22]. A quantitative comparison is compiled with the force and moment coefficients defined in Eq. 7.3 and the pressure coefficient at 2/3H. A qualitative comparison of the pressure and velocity field is also presented here.

Pressure coefficients at reference height

The pressure coefficient is the normalized pressure with respect to the free stream velocity as in Eq. 5.4. The time average of pressure coefficients at the reference height of 2/3 H is visualized for comparison in Figure 7.2. The RMS value of fluctuation of the coefficient of pressure is also visualized in the same figure. The C_p plots obtained from the current simulation are compared with numerous previous studies. These include both numerical and experimental studies. The figure compiles data from four wind tunnel experiments and three numerical simulations and compares it with the present study. The C_p plots obtained are in good agreement with the C_p distribution from earlier studies. An identical distribution is seen in the front and back faces. However, the present simulation does not accurately capture a jump seen in the C_p distribution at the front corner. Similar

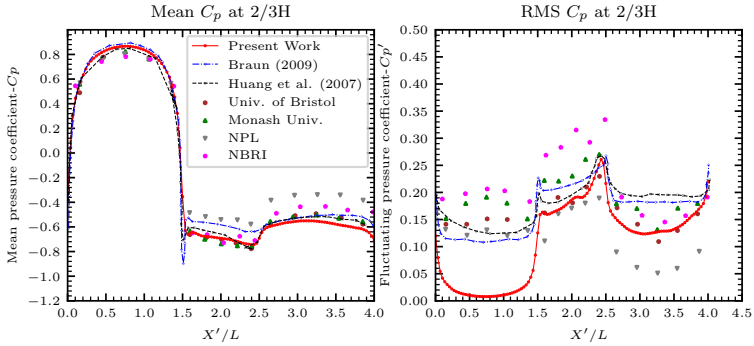

Figure 7.2 : Comparison with previous studies Mean (left) and RMS (right) of coefficient of pressure at height of 2/3H

statements can be made regarding the RMS of pressure fluctuations as well. Adequate agreement of cp values can be seen at the back face of the building. However, the RMS value at the front face of the building is under-predicted in the current simulation. It is evident that the RMS value is dependent on the turbulent characteristics of the incoming wind. Moreover, since we normalized the pressure with the free stream velocity for the C_p computation, the fluctuations on the front face were not well captured in our simulation.

Validation of force and moment coefficients

The force and moment coefficients are normalized base shear and base moment values as in Eq. 3.10. The time history plots of the aerodynamic force and moment coefficients for the present study are compared with previous literature [22] for validation. The comparison is shown in Figure 7.3. It may be observed that the two plots agree well. To quantify, we present the time average and RMS in time of these coefficients in Table 7.2. The mean values of the force and moment coefficients exhibit a lower error compared to [22]. Nevertheless, the RMS values of the force and moment coefficients are higher in the present study, which could be due to the higher Reynolds number compared to [22], making the flow more turbulent, hence more variation in the QoIs. Overall the correlation observed between the two studies is commendable.

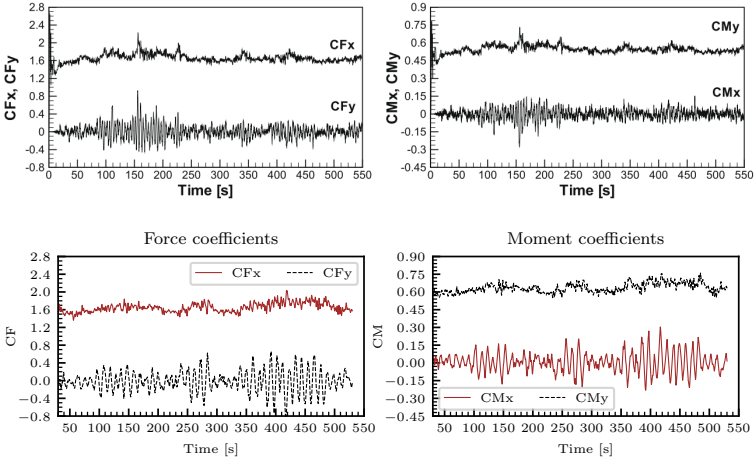

Figure 7.3 : Comparison with previous studies Time histories of coefficient of forces and moments reported in [22] (top), and the ones obtained in the present study (bottom).

Table 7.2 : Validation of force and moment coefficients - comparison with previous studies.

References	C_{F_X}	$C_{\sigma F_X}$	C_{F_Y}	$C_{\sigma F_Y}$
Present work	1.648	0.102	-0.015	0.238
Braun [22]	1.660	0.076	0.008	0.106
Obasaju [119]	1.490	0.060	-0.039	0.092
Huang et al. [120]	1.830	0.060	0.006	0.134
-	C_{M_X}	$C_{\sigma M_X}$	C_{M_Y}	$C_{\sigma M_Y}$
Present work	0.005	0.083	0.634	0.039
Braun [22]	0.004	0.048	0.570	0.038
Obasaju [119]	0.000	0.043	0.640	0.030

7.2.4 Results of validation studies for CAARC building B

The CAARC benchmark building B is simulated in Kratos Multiphysics and results are compared with previous studies [22]. A valid agreement is found between the two studies with respect to the coefficient of pressure, force coefficients, moment coefficients, and pressure fields. The time mean and time RMS of the quantities are used for the validation as a QoI, and a linear distance between them is used as a validation metric. The validation exercise ensures that the deterministic simulation used later for UQ is of superior quality. We present the UQ task on the same benchmark building in Chapter 8.

To improve the validation results, it is always possible to spend more elements on the mesh, use larger domains, smaller time steps, etc. Also, many local features may not be accurately modeled when validating against real measurements. The computational resources available are limited in practical cases. For SWE, it is the choice of the modeler to spend this resource on uncertainty quantification or making finer meshes and modeling detailed geometric features, etc. This particular choice is referred to as the quandary of resource allocation in this thesis. A detailed deterministic simulation, modeling all details, is not always possible or practical. One detailed deterministic model may not be able to cover all the design scenarios. In many cases, it is advantageous to do an uncertainty quantification with the available resources than to perfect the deterministic model to model local features or do simulations with the finest models. However, in the end, the quandary of resource allocation is up to the decision maker, designer, engineer, or researcher.

"Structural engineering is the art of molding materials we don't wholly understand into shapes we cannot fully analyze, so as to withstand forces we can't really assess, in such a way that the community at large has no reason to suspect the extent of our ignorance."

Dr. A. R. Dykes

CHAPTER 8

UQ OF TALL BUILDINGS SUBJECTED TO UNCERTAIN WIND LOADS

The design of a tall building requires analysis of the forces that are experienced by the same during the lifetime of the structure. There can be many sources of uncertainty in such a design scenario. The uncertainties can be from estimating the load components (such as the weight of the structure, or the change in live loads), environmental loads (wind, earthquake, snow loads, etc.), material properties, and geometry (type of material, composition, manufacturing process, and quality control in construction). The various uncertainties from both wind and structural parameters, as discussed in Chapter 1 and 3, are quantified for the validated benchmark problem in Chapter 7 here using high fidelity CFD simulations. Two examples are presented, one with a time-independent inlet and one considering fluctuating components of the wind.

8.1 Wind effects on structure - Fluid modeling

The building considered for this study is the same as from Chapter 7, the CAARC benchmark building. To study the effect of uncertainties, the deterministic simulation is verified and validated first as in Chapter 7. To analyze the wind effect on this structure, a numerical wind tunnel is used. The high Reynolds number of the wind flow problem in the current simulation makes it highly turbulent. Since natural wind is being assessed in this work, the incompressible Navier-Stokes PDE is used for the physical modeling (Eq. 5.5 and Eq. 5.5). Appropriate initial and boundary conditions are prescribed. The boundary conditions are depicted in Chapter 7.1.

The wind flow around the building is simulated using CFD analysis with the open-source Kratos Multiphysics solver. This involves a FEM solution for flow problems based upon a VMS formulation from [118]. The fluid domain is discretized with tetrahedral elements, and a BDF2 time integration scheme is used. The computational domain, as well as the boundary conditions, are described in Figure 7.1. The chosen size of the domain is similar to previous studies [12]. The blockage ratio is less than 0.8 % of the domain. The velocity and pressure snapshot at T = 300 seconds is shown for the deterministic simulation at the mean values of the uncertain parameters in Figure 8.1 and 8.2.

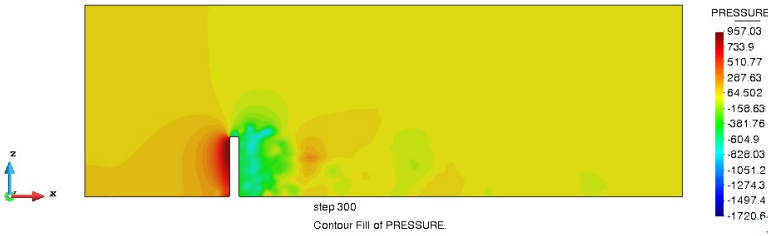

Figure 8.1 : Pressure along the vertical cut at time, t = 300 seconds.

8.2 Details of Structural modeling and analysis

The structural model of the CAARC B is modeled as a prismatic cantilever beam supported at the bottom, with continuous mass and stiffness. It is im-

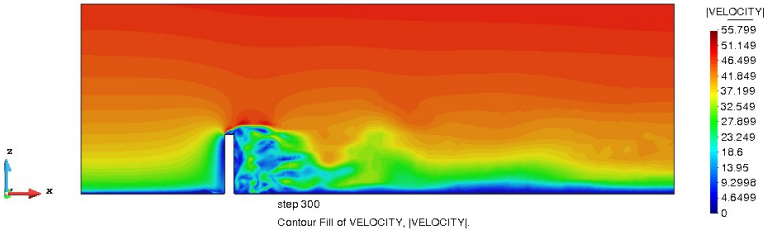

Figure 8.2 : Velocity along the vertical cut at time, t = 300 seconds.

possible to capture the modes prescribed in the benchmark with modeling as a full cross-section. For the study, a custom parametrizable Timoshenko beam with FEM formulation is co-developed and used as in [121]. This model is able to capture the modes prescribed by the benchmark study. The 3-dimensional (3D) building is modeled by a simplified structural model considering both bending and shear deformations. The 3D Timoshenko beam theory is hence used to capture the equivalent structural system. [122] presented a simplified methodology for the analysis of framed structure shear wall interaction problem. It can be seen that the Timoshenko beam model can effectively model various structural systems used for tall buildings in practice. Hence this structural choice is justified.

Timoshenko beam model

The Timoshenko beam theory is used to model the simplified structural system to analyze CAARC building B. A 3D prismatic, homogeneous, and isotropic beam element is used for the element formulation. The element considers both shear deformation and rotational inertia. Since the shear deformations are taken into account, the planes that were initially perpendicular to the neutral axis are no longer perpendicular to it after deformation.

$$E I u''_{(b)y}(x) = M(x) = -M_1\left(1-\frac{x}{L}\right)+M_2\left(\frac{x}{L}\right) \tag{8.1}$$

$$G(A/\alpha)u'_{(s)y}(x) = S(x) = -\frac{1}{L}\left(M_1 + M_2\right) \tag{8.2}$$

where A/α denotes the effective area in shear. The bending and shear deformations add up to the total deformation.

$$u_y(x,t) = u_{(b)y}(x,t) + u_{(s)y}(x,t) \tag{8.3}$$

where, $u_{(b)y}$ is the bending component and $u_{(s)y}$ is the shear component. A consistent mass formulation is used here. Both the stiffness and mass matrix, therefore, depend on the relative importance of the shear deformations to the contribution from bending. This ratio is

$$\Phi = \frac{12EI}{G(A/\alpha)L_e^2} \tag{8.4}$$

Where E and G are the moduli of elasticity and shear of the material, I is the moment of inertia of the cross-section, A/α is the effective shear area, and L_e is the length of the discrete beam element. In 3D two relative shear importance factors are defined corresponding to each bending direction.

For the dynamic problem at hand, the governing Equation of Motion (EOM) is

$$M\,\ddot{u}_y(t) + C\,\dot{u}_y(t) + K\,u_y(t) = F(t) \tag{8.5}$$

where, M, C and K are the global mass, damping and stiffness matrices and F is the external force. The external force is the wind time history in our case. This force corresponds to each of the Degree of Freedom (DoF), resulting from the computational wind engineering model. $u_y(t)$ is the displacement, $\dot{u}_y(t)$ the velocity and $\ddot{u}_y(t)$ the acceleration vector, respectively.

Implementation details of the structural model

The Timoshenko beam model implemented in the present work is capable of carrying out a 3D analysis of tall buildings subjected to wind forces. A linear geometric and material model is used for the system, and a

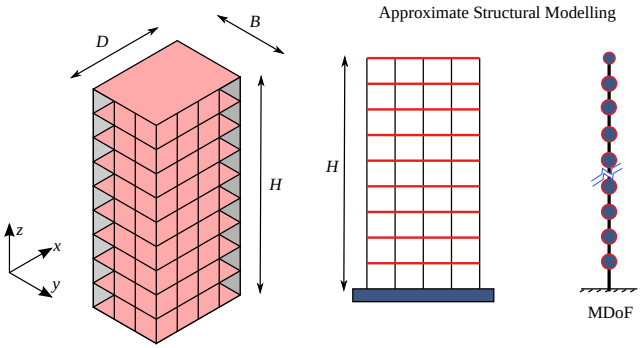

Figure 8.3 : Simplified structural model adopted for the current study.

Generalized-alpha time integration scheme is used for the time integration. The sway modes and torsional modes are uncoupled in the analysis. The torsional stiffness is calculated from the polar inertia of the equivalent cross-section. A Rayleigh damping model is assumed for computing the damping. The numerical structural models of the arrangement are set up such that the eigenfrequencies can be matched to the prescribed values.

8.3 Coupling of fluid and structure

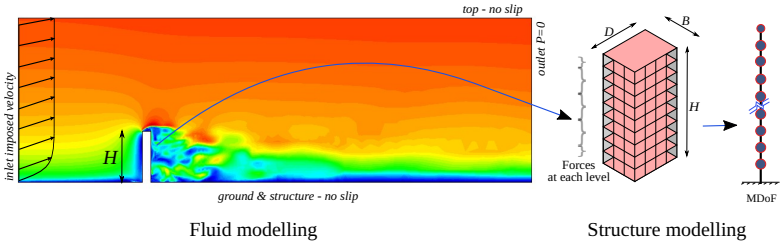

Figure 8.4 : Transfer of wind forces from CFD to the structure.

A coupled fluid-structure interaction needs to be evaluated for the analysis of wind effects on the structure. In the current study, a one-way coupled analysis is carried out. The fluid flow around the structure results

in pressure distribution on the surface and, hence, in nodal forces in the structure. These fluid forces are assigned to the structural model described in Figure 8.4. A one-way coupling is adopted; hence the deformations of the structure are not transferred back to the CFD model.

This assumption of fluid forces having a considerable effect on structural deformations compared to the impact of the deformations on the pressure field of the fluid is justified for tall buildings.

8.4 Numerical study 5A

8.4.1 Source of uncertainty

As discussed in Section 3.2, there are various uncertainties present in the wind effects on the structure. The Mean and RMS of the input wind velocity are considered uncertain. The roughness length, which depicts the roughness of terrain in the location, is also considered uncertain in the current study. These parameters determine the inlet boundary condition of the wind simulation. From the structure side, the natural frequencies and the damping of the structure are considered uncertain. The various uncertainties are tabulated in Table 8.1. The mean and standard deviation of the inputs are shown in the same table.

Table 8.1 : Uncertain input parameters and their distributions.

input parameters	Mean	standard deviation	distribution type
Mean wind velocity	40	4	normal
RMS velocity	4	0.4	normal
Roughness length	0.3	0.03	normal
1st mode eigen frequency	0.23	0.023	truncated normal
damping %	1	0.1	truncated normal

8.4.2 Propagation methods

A polynomial chaos method based on a regression approach is adopted for the current study. The theory is detailed in Chapter 2. The details of

the methods and steps for PC surrogate construction are briefly described here.

Once the deterministic model is prepared, verified, and validated, as elaborated in Section 7.2, the uncertain input parameters are quantified. This step involves the probabilistic characterization of the inputs. The PDF of the input uncertain parameters is identified through experiments. In cases where experimental data is not available, expertise or experience may be the basis for such a selection. In the PC method, the input uncertain parameters with a given PDF are represented by a PC expansion. Here a Hermite polynomial is chosen. The output PC parameters are also represented by a PC expansion. A Hermite polynomial is also used for the output parameters here. The order of the PC expansion is chosen, and the workflow is determined as in Figure 2.3. The PC coefficient d of the equation is determined through a regression approach, as shown in Eq. 2.22. The deterministic model is evaluated at each of the collocation points to get the output quantities of interest. In regression, at least the number of collocation points should be more than the unknown PC coefficients. When the number of collocation points is more, as oversampling, a common strategy adopted is to use least square regression. In this thesis, an oversampling of 3 is used for PC expansions. The post-processing to obtain the global sensitivity analysis, mean, standard deviation, etc., can be obtained from this without much additional effort. The details of the adopted workflow are shown in Figure 2.3.

8.4.3 Results and discussions

To start with, we first model the wind loads on the structure by a bluff body formulation from the C_d value of the building. Here the wind force is obtained from the formulae Eq. 5.4. The uncertainties of the mean wind profile and structure, as in Table 8.1, are used for this study.

Quantities of Interest

The base moment and base forces are the principal quantities of interest to the limit state of strength. The displacement and acceleration at the top floor are also of great interest to the designer as they govern the limit state of serviceability. Another QoI is the C_p distribution at 2/3 of the total height and the building's base moment and force. Since all these are time series,

it is essential to choose a quantity best representative of its behavior for decision making. One QoI is the mean of the time series. The second is the maximum of the time series. Another QoI is the expected maximum of the time series, which is the 90 % quantile of the distribution of the extrema for the time series as explained in Section 3.4.1

Convergence of standard MC

An extensive MC analysis is performed to obtain the stochastic response of the structure. The uncertainties tabulated in Table 8.1 are propagated through the structural model, and the various QoIs listed above are observed. The QoI analyzed are the drag force and the bending moment, as well as the top floor acceleration and the top floor displacement. The mean, maxima, and the maxima estimated of these quantities are observed through the MC analysis. The PDF of these quantities is plotted in Figure 8.5 with a varying number of MC samples. The convergence is checked for the drag force. The other quantities are observed. It can be seen that all the QoI are approaching their convergence values as the number of samples is increased.

Convergence of PC expansion

The stochastic response of the QoI is observed via PC through regression for the given problem. The PC order is increased from 2, 3, and 4. The PDFs of each QoI are plotted in Figure 8.6. The output uncertain parameters have a PC order of 2,3, and 4, and the MC 1100 simulations are also compared in this picture. It can be seen that the PC converges faster, and the stochastic response is captured by the PC surrogate pretty accurately.

The moments of the PC order and MC are compared in Table 8.2. It can be seen that the moments converge for the higher-order PC, and they match with the MC values. This shows the effectiveness of PC expansion in solving stochastic structural analysis problems. It can be seen that PC 2 is enough to predict the mean and standard deviation of all the quantities pretty accurately. Hence for the rest of this study, a PC 2 is used. The PC expansion can diverge for problems that lack smoothness. However, such behavior is not observed here. The PC 2, PC 3, and PC 4 are in close agreement with each other. They also match with the MC results. This shows the convergence of PC expansion results. The probability distributions shown

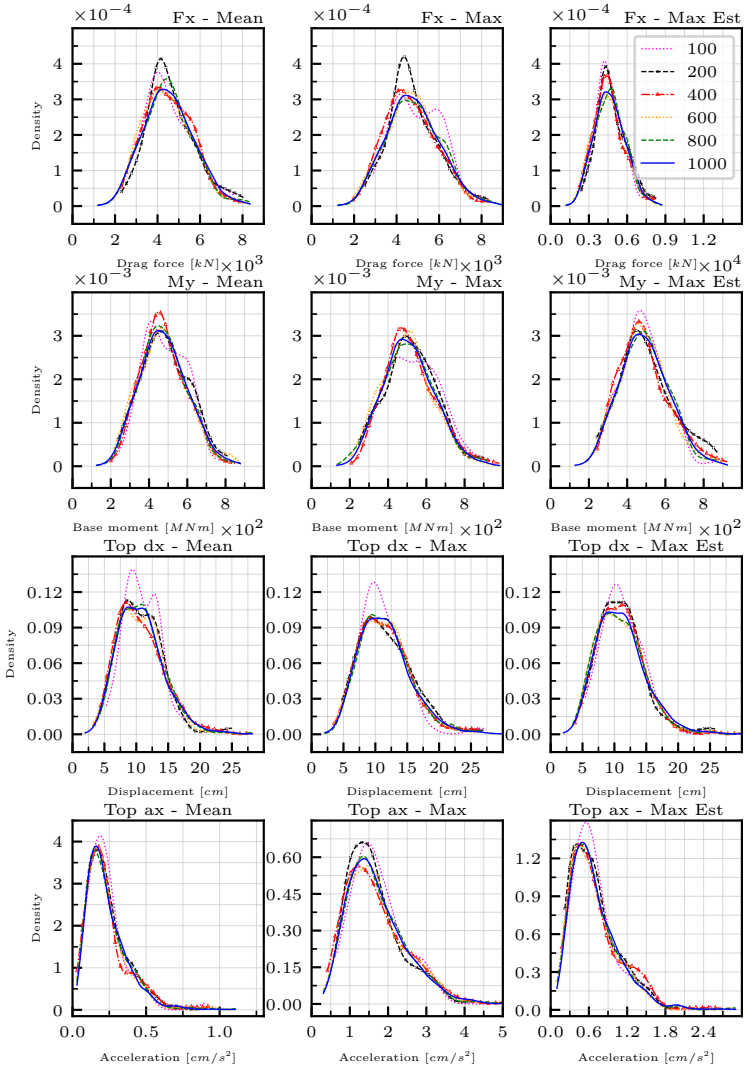

Figure 8.5 : PDF of responses evaluated with varying number of samples with MC.

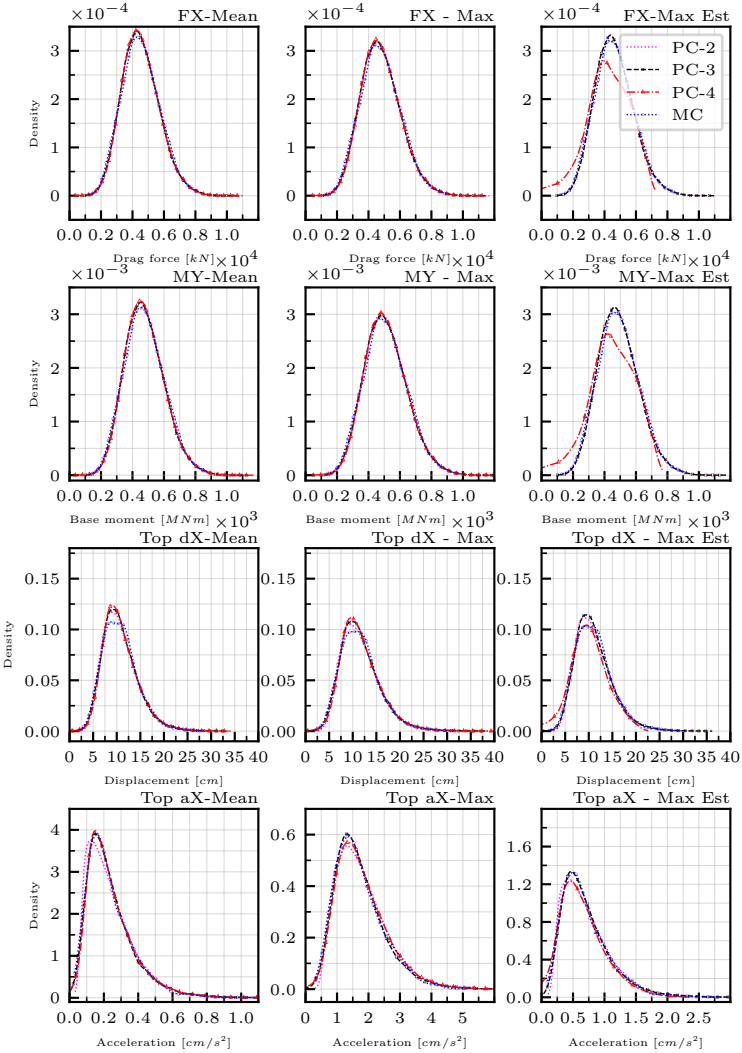

Figure 8.6 : PDF of responses for PC 2, 3 and 4 compared against MC results.

in Figure 8.6 indicate that the PC is an efficient way to determine the stochastic response of buildings under the stochastic wind.

Computational costs

The number of model evaluations of the PC and MC is compared here. It can be seen that the PC expansion is an efficient way to determine the stochastic response. However, it suffers from the curse of dimensionality. It grows exponentially when the number of input parameters grows, and it becomes prohibitive. It can be seen that PC is an efficient way where the number of input parameters is less. The computational gain offered by the PC is such that the post-process of the PC expansion can be done cheaply.

Table 8.2 : Responses PC vs MC for base moments ($N\,m$) and drag forces (N)

	My - Mean		My - Max		My - Max est	
-	Mean	STD	Mean	STD	Mean	STD
PC 2	4.76e+08	1.25e+08	5.13e+08	1.35e+08	4.90e+08	1.29e+08
PC 3	4.76e+08	1.25e+08	5.10e+08	1.35e+08	4.90e+08	1.29e+08
PC 4	4.77e+08	1.25e+08	5.12e+08	1.34e+08	4.29e+08	1.96e+08
MC	4.78e+08	1.25e+08	5.11e+08	1.34e+08	4.91e+08	1.28e+08
	Fx - Mean		Fx - Max		Fx - Max est	
-	Mean	STD	Mean	STD	Mean	STD
PC 2	4.52e+06	1.19e+06	4.80e+06	1.26e+06	4.63e+06	1.21e+06
PC 3	4.52e+06	1.19e+06	4.78e+06	1.26e+06	4.62e+06	1.21e+06
PC 4	4.53e+06	1.18e+06	4.79e+06	1.25e+06	4.05e+06	1.85e+06
MC	4.54e+06	1.19e+06	4.79e+06	1.25e+06	4.64e+06	1.21e+06

8.5 Response of uncertain structure under uncertain mean wind

Here in this section, a CFD is used with PC 2 for evaluating the stochastic response of the building under wind loads. The details of the CFD are

Table 8.3 : Responses PC vs MC for top displacement (m) and top accelerations (m/s^2)

	dx - Mean		dx - Max		dx - Max est	
MC No.	Mean	STD	Mean	STD	Mean	STD
PC 2	1.07e-01	3.66e-02	1.16e-01	4.15e-02	1.11e-01	3.87e-02
PC 3	1.07e-01	3.72e-02	1.16e-01	4.19e-02	1.11e-01	3.94e-02
PC 4	1.08e-01	3.67e-02	1.16e-01	4.12e-02	9.65e-02	4.94e-02
MC	1.07e-01	3.65e-02	1.16e-01	4.07e-02	1.11e-01	3.84e-02
	ax - Mean		ax - Max		ax - Max est	
MC No.	Mean	STD	Mean	STD	Mean	STD
PC 2	2.36e-03	1.36e-03	1.80e-02	8.17e-03	7.15e-03	3.89e-03
PC 3	2.37e-03	1.43e-03	1.74e-02	8.11e-03	7.09e-03	3.97e-03
PC 4	2.38e-03	1.42e-03	1.77e-02	8.16e-03	6.17e-03	4.20e-03
MC	2.33e-03	1.36e-03	1.70e-02	7.71e-03	6.95e-03	3.80e-03

shown in the Section 8.1. The PC 3 is also plotted for reference in Figure 8.7. It can be seen that PC 2 and PC 3 are in close agreement with each other. The mean value and the deterministic value corresponding to the mean of each of the QoI are also plotted in the figure. It can be seen that the mean of the PDF is always more than the deterministic value. This indicates the need for a stochastic analysis of the problem at hand. To do a full MC for the CFD is not possible for the industry due to the prohibitive cost. Hence PC solution like the one proposed above may be employed. It is still manageable to do 40 CFD simulations to obtain a pretty accurate estimate of the QoI as shown here. The top floor acceleration as QoI dealt in detail in numerical study 5B, and hence, we do not focus on top floor accelerations here. While comparing the stochastic response of the equivalent wind load and CFD, it may be observed that the equivalent wind load estimates are conservative. They are also unable to capture the other wind effects like the vibration across the direction in the flow.

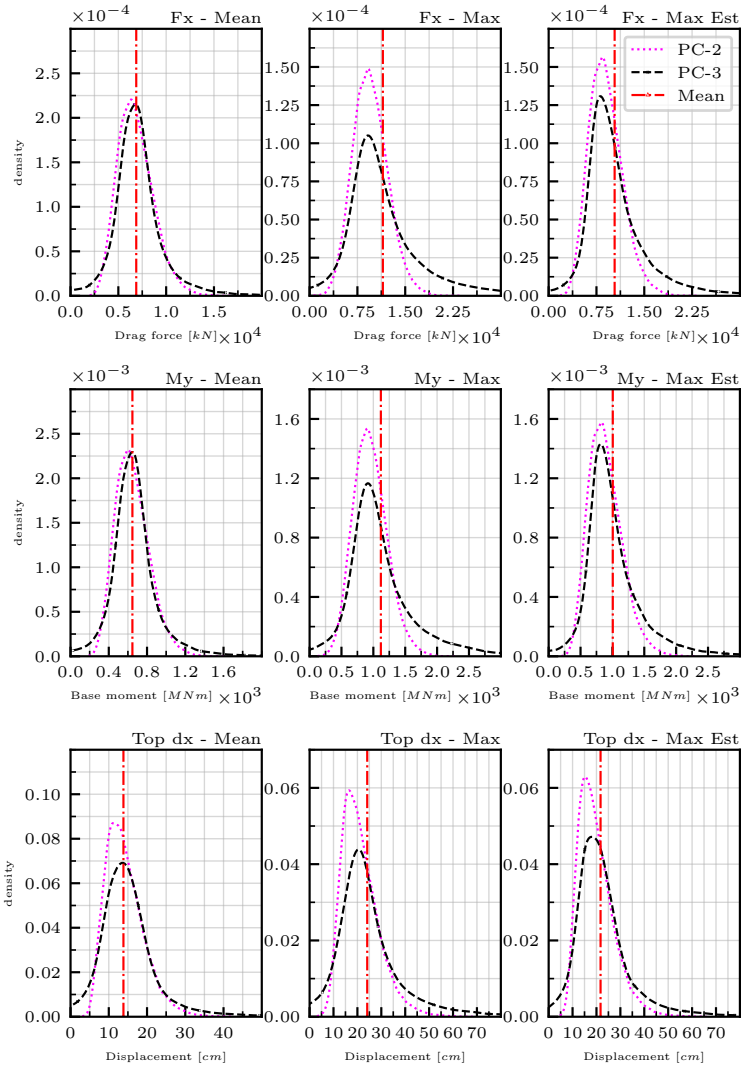

Figure 8.7 : PDF of responses evaluated with PC 2 and PC 3 for wind simulated in CFD.

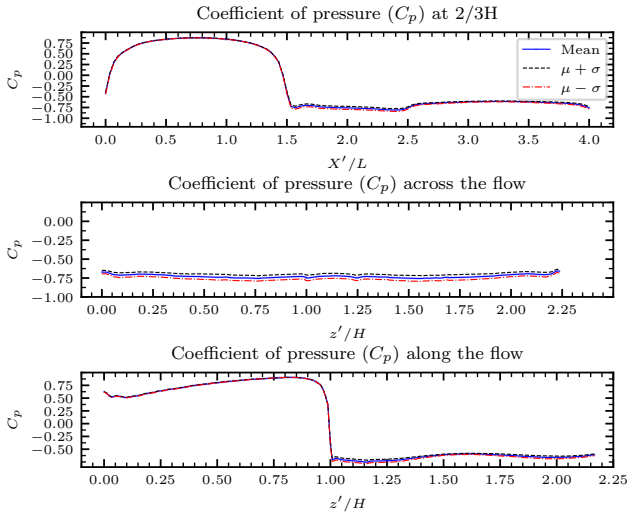

Figure 8.8 : C_p distribution as QoI along the reference height (top); across the flow(middle); and along the flow (bottom).

8.5.1 Global sensitivity analysis

A global sensitivity analysis is done in order to find out how uncertainties in the QoI are affected by the input parameters. Unlike local sensitivity analysis, global sensitivity measures are incorporated over the entire range of the input parameters. In the global sensitivity analysis, uncertainties due to the combination of the parameters are also considered. Global sensitivity analysis methods can be classified into two groups as (a) regression-based methods and (b) variance-based methods. Sobol' indices are a variance-based method, and they provide accurate information of sensitivity in most of the models [52]. The Sobol' indices based on polynomial chaos are determined from the PC expansion with negligible additional computational cost as shown in Eq. 2.28. The total sensitivity indices of all the parameters are stabilized in Table 8.4. dx and ax refer to the displacement and acceleration at the top of the building. It can be seen that for the forces and moments, the Sobol' indices are high for the wind parameters compared to the structural parameters. It is common knowledge that the wind

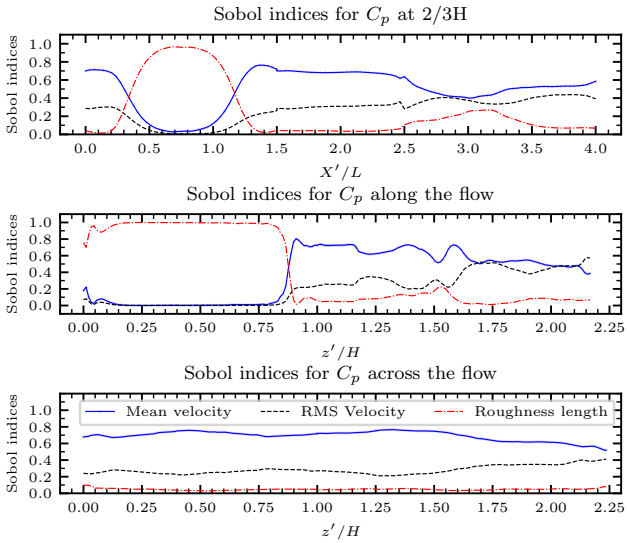

Figure 8.9 : Sobol'indices for C_p distribution at three cross sections.

parameter has more uncertainty compared to that of the structural parameters. When this is combined with the fact that Sobol' sensitivities are more for the wind parameters, it is important to quantify the uncertainties of the incoming wind during the design of tall buildings.

8.5.2 Pressure coefficient

The mean and standard deviation of the C_p distribution is plotted in Figure 8.8. This covers the deterministic simulation as well. The sensitivity indices of the QoI are also plotted in the figure. This shows that the roughness parameter has an increased contribution in the front face. However, the effect of this parameter on the rear and side face is negligible.

Table 8.4 : Total Sobol' indices for wind effects on CAARC building responses.

Uncertain parameters	Fx	My	dx	ax
Mean velocity	0.808	0.813	0.875	0.941
RMS velocity	0.607	0.609	0.736	0.871
Roughness length	0.143	0.160	0.114	0.114
Frequency	0.0441	0.0446	0.049	0.452
Damping	0.264	0.259	0.177	0.197

Note: dx and ax refer to the displacement and acceleration at the top of the building.

8.6 Numerical study 5B

Here, focus is given to the numerical study with wind uncertainties of both the mean parameters as well as the fluctuations considered. Since this is a high-dimensional problem, the standard MC method is used for uncertainty quantification. The quantities of interest are similar to the previous study. To reduce the redundancy with Numerical study 5A focus is not on the base forces and moments. Instead, the focus is on the top-floor acceleration for the serviceability of the structure. This example demonstrates the CVaR as a risk measure for acceleration at the top for performance-based design selection.

8.6.1 Response of uncertain structure under natural wind condition

It is common knowledge that wind is intrinsically stochastic. Here a natural wind scenario is considered, where the uncertainties arising from the mean wind parameters, as well as that of the fluctuating component, are considered. The uncertainties of the fluctuating part are modeled with the Mann model as elaborated in Section 3.2. The uncertainties considered in this study are tabulated in Table 8.5. The uncertainties are considered from the code book [63]. Since the Mann model has a large number of uncertain variables, it is not possible to use PC as in Numerical example

5A. The Reynolds number is of the order of 10^8. The standards MC method is used as elaborated in Section 2.3 for uncertainty quantification. The convergence of the MC algorithm is evaluated by assessing the statistical error. The QoI is the time-averaged drag force, and other quantities like the pressure, top displacement, top acceleration, etc., are also computed. The conditional value of risk of the acceleration is also computed. To demonstrate the engineering application of the CVaR as a performance measure, two designs of the structure are compared. The structural parameters of both designs are tabulated in Table 8.5. The same wind scenarios are applied and computed against these two designs, and the structural QoI is evaluated.

Table 8.5 : Details of two designs demonstrating the selection based on CVaR of acceleration

Design option	1st mode frequency	$\mu+3\sigma$	CVaR
Design 1	0.18	0.09306	0.07816
Design 2	0.25	0.09570	0.07608

Results and discussions

It is known that the accelerations at the top of a tall building may make the occupants uncomfortable due to their high values. Hence the design codes [1] try to have some specific criteria on this performance matrix. The various criteria are generally RMS or standard deviation [123]. The RMS for both designs are evaluated and shown in the figure in relation to the design criteria. It may be observed that both these designs follow the regulatory design criteria. Now as a designer, if one needs to choose between these two designs, we propose to use CVaR as a risk measure to compare the performance of the two designs.

CVaR as a performance measure for servicibility

We propose to use CVaR as a performance measure for evaluating the serviceability of occupant comfort in a tall building. It is safe to have the acceleration go higher than the prescribed values for a structure as long

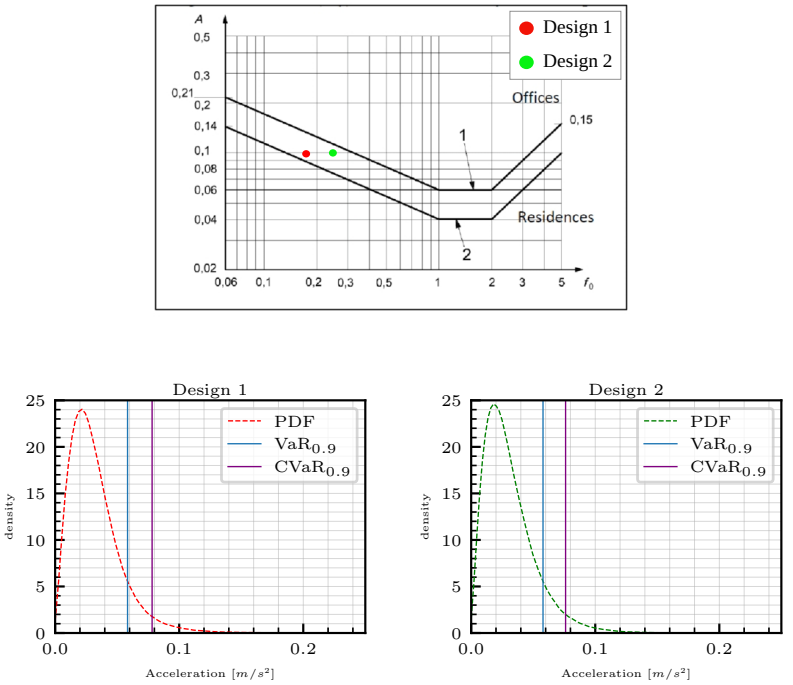

Figure 8.10 : Performance comparison of two designs: based on the code criteria (top); PDF and CVaR of top floor acceleration in design 1 (left bottom); in design 2 (right bottom).

as the safety criteria are met. However, the occupants do not feel safe in those cases. By choosing the CVaR as a performance measure, we are choosing a design that, in the worst case, tries to reduce the expectation of those exceeded values rather than simply reducing the amount of those exceedance as in VaR.

Acceleration limits in code books are a function of the frequency of the vibration. The widely used upper limits for residential and office buildings are shown in Figure 8.10. We also plot the two designs we used in this study in the plot. Assuming we have an office building, both designs are under acceptable limits. Peak acceleration limits are used in these reference plots. The peak acceleration is computed as the mean and 3 times the standard

deviation here. We demonstrate this in Table 8.5 and Figure 8.10. It can be seen that even though both design 1 and design 2 are similarly performing, as a designer, it is useful to use Design 1 as a favorable choice since it has a lower CvaR of the accelerations.

8.7 Concluding remarks on the UQ application for wind effects on structures

We demonstrated the use of a PC for a low-dimensional simplified wind problem. However, when the fluctuations of the wind need to be considered, standard MC is used since the dimensions are larger. Various QoIs are quantified, and the use of UQ for wind engineering problems is demonstrated. We also propose to use CVaR as a performance measure for the serviceability of designs, and the CVaR-based design selection of tall buildings is demonstrated. A similar CFD setup and MC and uncertainties of the mean and fluctuations are used for the OUU example in Chapter 9. The uncertainties in the wind direction are also considered there.

" Uncertainty is an uncomfortable position. But certainty is an absurd one. "

Voltaire

CHAPTER 9

OPTIMIZATION OF TALL BUILDING UNDER UNCERTAIN WIND

The wind load on a structure can be reduced by optimizing the shape of the building. However, this optimization procedure becomes challenging when some input parameters are uncertain. Here in this chapter, the results of the OUU procedure presented in Chapter 4 for a wind engineering application at a high Reynolds number flow are presented. The uncertainties of the incoming wind at the specific location of consideration are considered. The location-specific design of the building with uncertainties specific to the location results in a more suitable design with reduced loads. This, in turn, will result in a design with reduced cost of construction and hence reduced carbon footprint. The two OUU problems, mean optimization and risk-averse CVaR optimization, are presented in this chapter for two design scenarios, one with only the twist as design parameters and the second with a twist and tapering as design parameters. The results show the superiority in the performance of CVaR optimization against

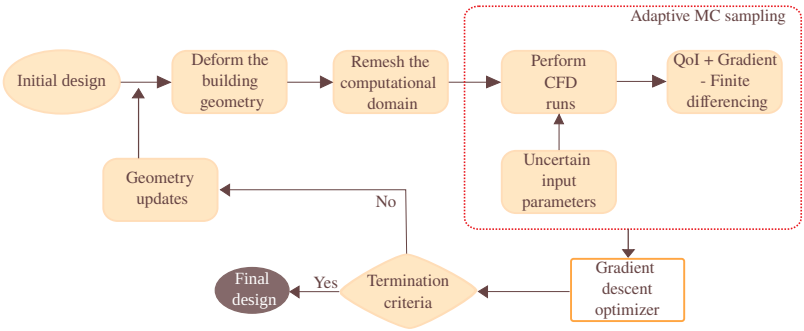

Figure 9.1 : Adopted workflow for shape optimization under uncertainty for tall buildings.

mean value optimization. The contents of this chapter are similar to the publication [67].

9.1 Optimization under uncertainty workflow

The developed stochastic optimization workflow based on finite difference sensitivities and adaptive sampling is detailed here. The optimization workflow tries to minimize the observables of the selected QoI by searching for the best combination of design parameters while taking into account the uncertainties present in the incoming wind.

A flow chart of the optimization workflow is presented in Figure 9.1. The workflow begins by defining the objective function J, design parameters $\mathcal{Z}$, and uncertain variables ξ. The objective function J is based on the base moment $M_{\mathcal{Z}}$ and is defined to be either the expected value $J(Z) = E[M_Z]$ (Problem 1) or the conditional value at risk at confidence level $\beta = 0.90$, $J(\mathcal{Z}) = \text{CVaR}_{0.90}(M_{\mathcal{Z}})$ (Problem 2) as defined earlier. The objective function $J(\mathcal{Z})$ depends on the geometry of the building (Figure 9.2), which in turn depends on the design parameters - $\mathcal{Z}$.

Whenever the CAD building geometry or incidence angle (θ) is altered, the background CFD mesh is remeshed to capture the new geometry

and/or the new wind incidence angle. In cases where the incidence angle (θ) of the wind is also an uncertain input parameter, each uncertainty quantification sample within an optimization iteration requires re-meshing of the domain.

Samples of the objective function, $J_i(\mathcal{Z}_k)$, are obtained by simulating the wind flow around the building in Kratos multiphysics [124]. These 3D CFD simulations are computationally expensive. Hence, an adaptive sampling strategy (i.e., Algorithm 3) is implemented to minimize the number of samples required as much as possible.

A finite-difference approach estimates the gradients $\nabla J_i(\mathcal{Z}_k)$. As the number of design parameters is low, the extra effort required to estimate these gradients is manageable. Once $\nabla J_i(\mathcal{Z}_k)$ is computed, it is used to update the building geometry via the stochastic gradient descent update rule(Eq. 4.8). Multiple iterations are required for the optimization algorithm to converge to the final design. A relative tolerance of 0.01 is chosen to evaluate the convergence of the algorithm.

9.2 Details of building designs and CFD

Since they are complex, detailed and accurate modeling and analysis of tall buildings are required for wind loads. The geometric features of the building greatly influence the flow around it. For this reason, high-fidelity computational fluid dynamics (CFD) are typically required to predict the effects of wind flow around tall buildings accurately. The OUU example is implemented in Kratos Multiphysics [124, 125] and the MMG domain meshing tool [126].

9.2.1 Modeling and simulating complex geometries

Wind flow around a tall building is modeled by the incompressible Navier-Stokes equations and solved in Kratos Multiphysics as elaborated in Section 8.1. The specific LES formulation used is the variational multiscale (VMS) formulation described in [118].

The corresponding boundary conditions and domain D are the same as that we used in the validation study in Section 7.2. One significant difference from the benchmark case is the use of a fluctuating inlet in the study. This additional complexity is taken care of by a time-varying

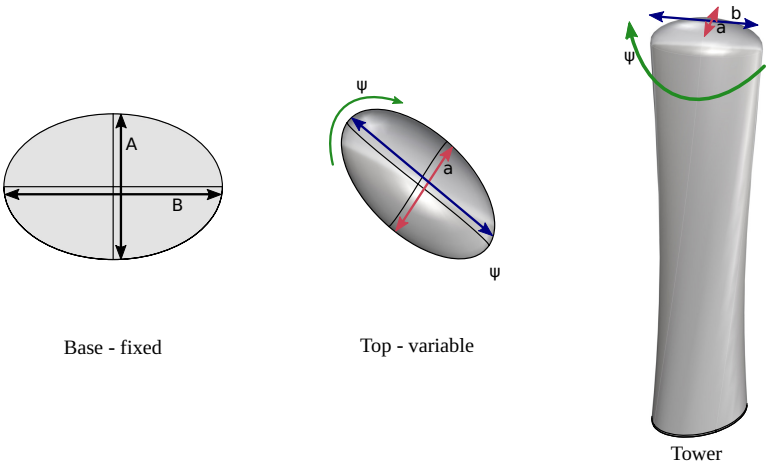

Figure 9.2 : Parameterized geometry of the tall building.

boundary condition at the inlet from the wind snapshots generated as elaborated in Section 3.2. The length scale is the same as the height of the building. The flow domain is chosen in such a way that the inflow region develops the flow from the inlet, and a sufficiently large outflow is available to capture the development and dissipation of vortices. A blockage ratio of approximately 0.8% is maintained in the current domain.

The design parameters in the optimization workflow are incorporated into the geometry of the tall building through the parameterization of the tall building. The base geometry of the tall building is an elliptical cross-section with a dome at the top. The geometry is inspired by real-world tall buildings as elaborated in Section 1.2. The two design parameters considered for the tower are the tapering and twisting of the elliptical cross-section along the height. The building is constructed based on these two parameters. In cases where the angle of the incident wind is also an uncertain parameter, the tall building is rotated to match this parameter.

The details of the computational mesh are shown in Figure 9.3. The domain is meshed with tetrahedral elements. More elements are present in the inner refinement zones close to the building to capture the flow characteristics better. The total number of elements is around 7×10^5. The

Table 9.1 : Fluid and flow domain details.

Parameter	Value	Unit
Density	1.225	kg/m^3
Viscosity	1.507×10^{-5}	m^2/s
Dynamic viscosity (ν)	1.846×10^{-5}	Ns/m^2
Reynolds number (Re)	2.9×10^7	
Height of the building (H)	180	m
Time window	[50, 200]	s

inlet boundary condition is time-varying and is a superposition of the mean profile $\overline{u}$ and the fluctuating component u' described in Section 3.2. Since the incidence angle of the wind is also considered uncertain in this study, the building is rotated inside the domain for each wind direction θ. The domain is then locally remeshed, ensuring the inflow is at the intended angle θ. A remeshing is also needed when the geometry is updated at the beginning of each optimization step. The air and flow domain parameter values used in the simulations are tabulated in 9.1.

The high Reynolds number of the problem makes it very turbulent. The fluid domain is modeled with a fractional step element with a second-order backward differentiation formula (BDF) for time integration. The time step used for the simulation is chosen such that the Courant-Friedrichs-Lewy (CFL) number remains less than 1 in the smallest element near the building domain, where the largest velocity is also expected.

As the geometry changes at each optimization iteration, the meshing process is automated. A mesh moving strategy similar to the one used in Section 5.1.3 may not be optimal here since the geometry updates are large enough to cause distortion of fluid elements and produce meaningless results. Hence, a re-meshing approach is explored here to generate body-fitted fluid meshes. MMG remesher [126] is used for this purpose. The geometry is remeshed with multiple refinement zones as shown in Figure 9.3. However, the remeshing is only done in the inner zones, preserving the overall mesh structure across simulations. The remeshing is also required for each of the uncertain wind direction θ samples. The whole fluid domain is initialized with a zero velocity initial condition.

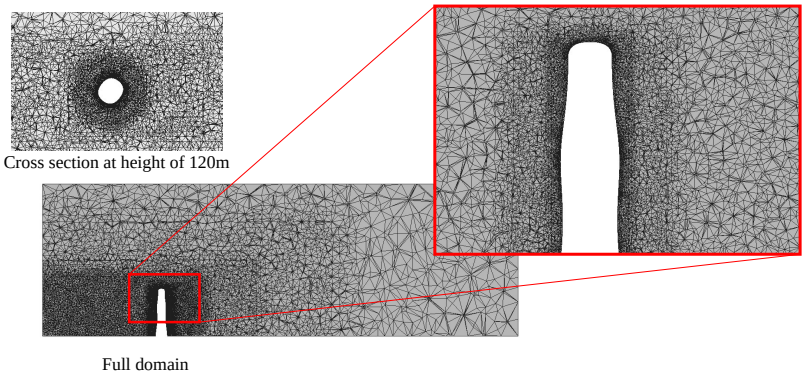

Figure 9.3 : Details of the adopted mesh for the base simulation used for refinement to result in each direction samples in each optimization step.

The total time of the simulation is 200 seconds. This is such that to capture 10-15 cycles of vortex shedding. Even though a 10-minute (600s) simulation is an industry practice, this reduced time window is found to be enough to capture interesting phenomena (vortex shedding) accurately. The inlet velocity is ramped up gradually in time by rescaling it by $t/10$ between $t = 0$ and $t = 10$. The results and flow field to estimate the QoI are used only for $t \in [50, 200]$ to filter out the transient effects of the flow development.

9.2.2 Details of the QoI

There are two main criteria that need to be considered in the design of tall buildings: the strength criteria and the serviceability criteria. The strength criteria deal with the strength of the structure and guarantee that the building will not fail under the maximum design load. The serviceability criteria deals with the comfort of the occupants in the building.

The quantity of interest considered here is the norm of the base moment, which associates with the strength criteria as elaborated in Section 7.2 and in Equation 3.10. This quantity is of specific interest to us because it decides the amount and type of foundation and structural system required for the building and amounts to a significant fraction of the

Table 9.2 : Details of the random variables in the velocity field model, $u = \overline{u} + u'$.

Random variable	Distribution	Parameters
Friction velocity (u_*)	Weibull	See 3.2.2.
Wind direction (θ)	von Mises	See 3.2.2.
Roughness length (z_0)	Uniform	$z_L = 0.01$, $z_U = 0.1$.
Random seed for turbulence fluctuations (r)	Uniform	$r_L = 0$, $r_U = 1$.

total cost. Hence, minimizing this quantity could lead to a direct cost saving in the project.

9.3 Details of the uncertain inputs

The uncertainties are associated with the incoming wind. All the uncertainties are considered in this demonstrator OUU example. The uncertainties of both the mean profile u and the fluctuations u' are modeled. Also, the uncertainties arising from the incidence angle, as elaborated in Section 3.2 are also accounted for. The various uncertainties considered in the OUU examples are tabulated in Table 9.2.

9.4 Results of Numerical study

The optimization algorithm developed and presented in Section 4.4 is applied in two numerical investigations here. Numerical study 6A employs only one design parameter, the angle of twist of the building $\mathcal{Z} = \psi$. Numerical study 6B employs two design parameters, the twist and minor axis length of the top cross-section of the building geometry $\mathcal{Z} = (\psi, a)$. The top area is kept constant and is added as a constraint $\pi a\, b/4 = c$, for some fixed constant $c > 0$. This is closer to reality since the client would not be happy to reduce the usable floor area of the building. The multi-todo challenge introduced in Chapter 3 is addressed by using the task scheduler Compass [127–129]. The computations were run on the Karolina supercomputer of the IT4Innovations cluster located in Ostrava, Czech Republic. The entire optimization under uncertainty run is expensive. To present

Table 9.3 : Numerical study 6A and 6B - details of initial building design.

	Study 6A	Study 6B
Angle of twist (ψ_0)	160°	295°
Major diameter at top (a_0)	35m	30m
Minor diameter at top (b_0)	20m	30m

a scale of the computational cost, the CVaR optimization required more than 4.36×10^5 CPU hours in the cluster. This expense is justified for practical design scenarios since the tall buildings are one-time builds and the savings in material and repair expenditures from the superior performance of the OUU final design.

9.4.1 Numerical study 6A

The first numerical study is a single parameter optimization under uncertainty. The uncertain parameters elaborated in Table 9.2 are considered. The only design parameter in this example is the twist of the building $\mathcal{Z} = \psi$. The major and minor diameters, a and b, are fixed in all the optimization steps. For this configuration, the optimization problems Problem 1, Problem 2, and Problem 3 are solved. The results are presented in Figure 9.4. As explained in Section 4.3 Problem 3 is a deterministic optimization with $\xi = \xi_{\text{PWD}}$, which corresponds to the predominant wind direction $\theta = \theta_{\text{PWD}}$ with all other wind field parameters fixed at their mean values, $u_* = E[u_*]$ and $z_0 = E[z_0]$, and for a specified random seed $r = r_{\text{PWD}}$.

$$\xi_{\text{PWD}} = (E[u_*], \theta_{\text{PWD}}, E[z_0], r_{\text{PWD}}). \tag{9.1}$$

Here, as in Table 9.2, $\theta_{\text{PWD}} = 260°$, $E[z_0] = 0.05$, and $E[u_*] = 10$m/s. The random seed r_{PWD} was specified arbitrarily.

Table 9.4 and Figure 9.4 present the optimization logs for the three optimization problems. It can be observed that the final geometry of the PWD design differs significantly from the mean and CVaR designs. The PWD optimization was essentially a deterministic one and did not consider the uncertain wind (direction, magnitude, and fluctuations). This optimization problem, hence, misses much important information about the physical

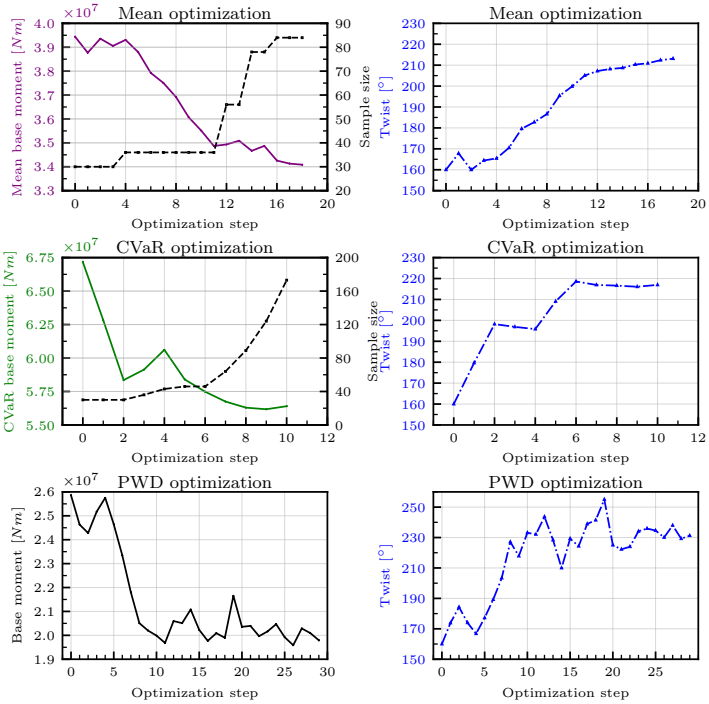

Figure 9.4 : Numerical study 6A- optimization records for the risk-neutral (Problem 1), risk-averse (Problem 2), and PWD (Problem 3) problems.

environment where the build resides. Problem 1 and Problem 2 do take these uncertainties into consideration and return a more robust design against variability in input parameters. In Table 9.4, the respective objective function for optimization are presented, and it can be seen that each of the optimizations has minimized respective objective functions. In the last column, the objective function for the deterministic problem is presented for comparison for the other two problems Problem 1 and Problem 2. For one specific wind direction (PWD), the final designs of the stochastic optimization problem perform worse compared to Problem 3. However, it

Table 9.4 : Numerical study 6A - details of the final building designs.

Optimization type	J_{Final}	$1-\frac{J_{\text{Final}}}{J_{\text{Initial}}}$	Twist (ψ)	$J_{\text{Final},\xi=\xi_{\text{PWD}}}$
Risk-neutral Problem 1	34.09×10^6Nm	13.6%	214.08°	37.36×10^6Nm
Risk-averse Problem 2	56.40×10^6Nm	16.0%	216.97°	58.49×10^6Nm
PWD Problem 3	19.79×10^6Nm	23.4%	231.24°	19.79×10^6Nm

is interesting to note that when uncertainties are considered, the PWD is not sufficient.

The time series and PDFs of the base moments for each optimization problem are shown in Figure 9.5. For both the stochastic optimization problems, the time series for mean and CVaR solutions have shifted towards a lower base moment distribution. To check the performance of the final PWD design under the uncertain wind, the time series and PDF are plotted similarly. The mean and CVaR are evaluated and shown in the figure. It may be observed that these stochastic objective functions have not improved much from the initial design for the case of the PWD design. This demonstrates the need for stochastic design for tall buildings under the uncertain wind.

The final building designs are collected together for further comparison in Figure 9.7. Figure 9.6 shows the shape evolution of all three problems as observed from the top. Both the stochastic optimization Problem 1 and Problem 2 produce practically the same building design. This is potentially due to the fact that there is only one design parameter. This low-dimensional nature of the design space forces both the optimization to proceed in the same direction.

Hence, a two-parameter optimization under an uncertainty problem is explored in Numerical study 6B, where the final designs of mean and CVaR optimization significantly differ.

9.4.2 Numerical study 6B

In this example, the stochastic optimization for a twisted tapered building with a fixed roof area is elaborated. The design parameters are $\mathcal{Z}=(\psi,a,b)$ with $\pi ab/4=c$. The two optimizations under uncertainty problem are

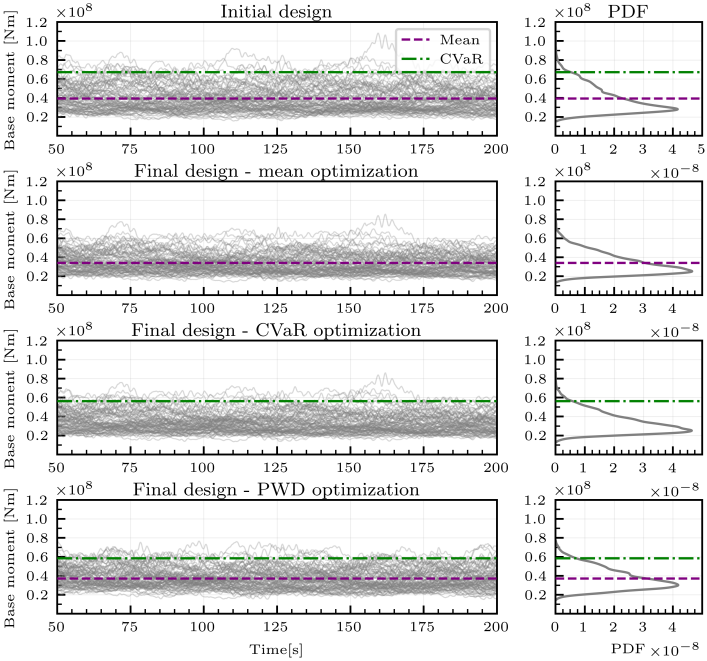

Figure 9.5 : Numerical study 6A- time series and PDFs of the base moment for the risk-neutral (Problem 1), risk-averse (Problem 2), and PWD (Problem 3) problems.

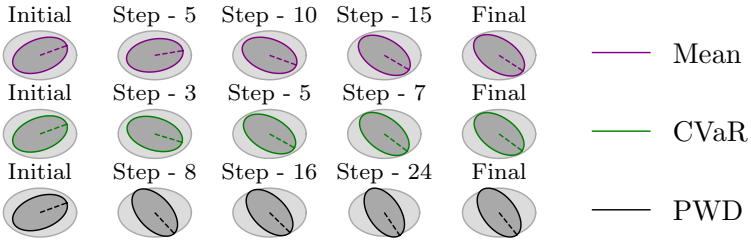

Figure 9.6 : Numerical study 6A- progress of optimization for the risk-neutral (Problem 1), risk-averse (Problem 2), and PWD (Problem 3) problems viewed from the top.

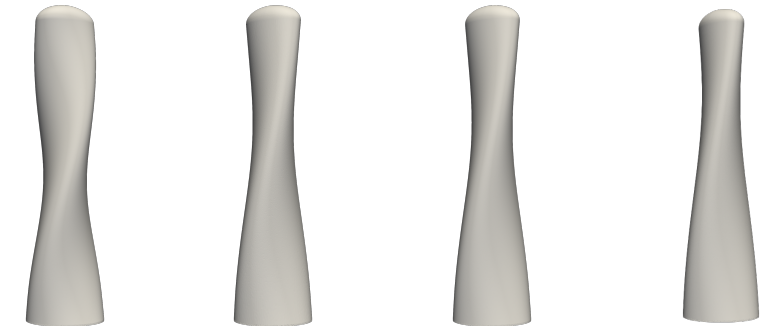

Figure 9.7 : Numerical study 6A: initial and final building designs.

Table 9.5 : Numerical study 6B - details of the final building designs.

Optimization type	J_{Final}	$1-\frac{J_{\text{Final}}}{J_{\text{Initial}}}$	Twist (ψ)	Minor axis (a)
Risk-neutral Problem 1	46.36×10^6Nm	5.811%	298.019°	24.383m
Risk-averse Problem 2	69.55×10^6Nm	17.084%	307.675°	21.904m

presented, namely the risk-neutral optimization Problem 1 and the risk-averse optimization Problem 2. In both cases, the QoI is the base moment, similar to Numerical study 6A. The stochastic gradient descent with adaptive sampling (Algorithm 3) is employed in this example as well, and it converges around ~ 25 iterations in both cases. The improvement in the objective function is illustrated in Figure 9.8 and 9.9. It can be seen from 9.5 that the objective function improves by $\sim 6\%$ for the mean optimization problem. The plot also showcases the number of samples required for each optimization step. The performance of the adaptive sampling strategy is illustrated here. As we approach the optima, an accurate estimate of the objective function is made, and the number of samples increases, showing the effectiveness of the adaptive algorithm adopted. The evolution of the two design parameters considered for the optimization is also shown in the figure.

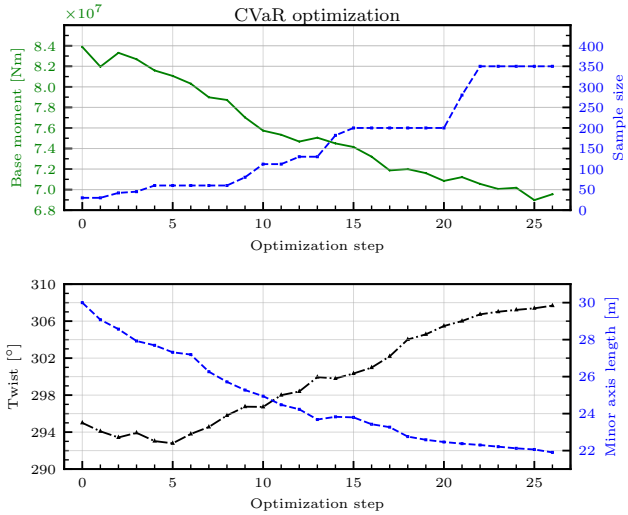

Figure 9.8 : Numerical study 6B: optimization record of risk-averse (Problem 2) optimization.

Although the objective function does not improve significantly, the sequence of designs in Figure 9.12 clearly illustrates the most critical shape changes. Indeed, the top cross-section becomes more tapered, and the twist aligns close to the PWD to reduce the wind effects on the building. The tapering of the cross-section is found to reduce wind loading. Interestingly, the twisting is less prominent than the tapering in the final building design.

The optimization log of the risk-averse design optimization is given in Figure 9.8. An $\sim 17\%$ improvement in the objective function $J(\mathcal{Z})$ was observed. The progress of the design parameters with optimization iteration is also shown in Figure 9.8. We observe that the number of samples required increases as the design converges to the optimum, similar to the mean optimization, showing the effectiveness of the adaptive sampling algorithm employed. The adaptive sampling approach is found to be 62.8% cheaper compared to the cost of performing each iteration with the highest number of samples without an adaptive sampling approach.

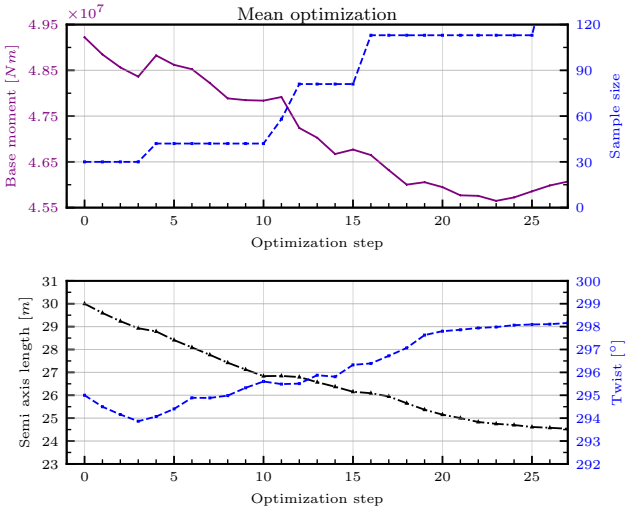

Figure 9.9 : Numerical study 6B: optimization record for mean problem Problem 1.

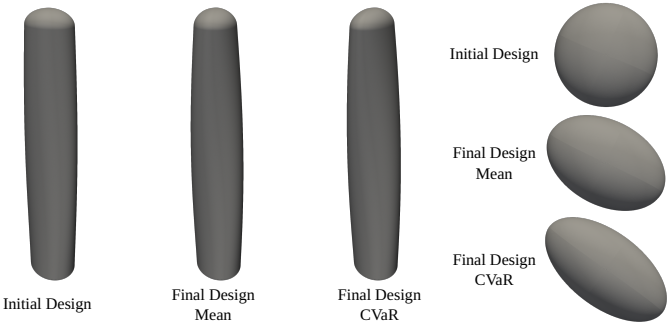

Figure 9.10 : Numerical study 6B: initial and final building designs.

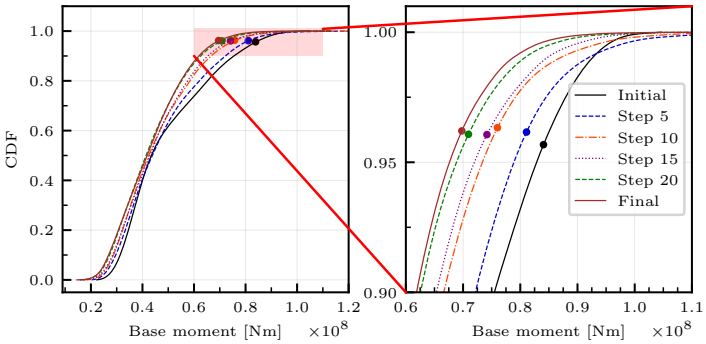

Figure 9.11 : Numerical study 6B: CDF of the base moment at various optimization iterations. $\text{CVaR}_{0.90}(M_{\mathcal{Z}})$ is represented as a dot in right plot.

Compared to the mean problem earlier, the number of samples is almost three times higher for the risk-averse problem. This is reasonable since more samples are required to estimate the tails accurately in the risk-averse problem. The shape change in the risk-averse problem is more than the mean problem. Figure 9.12 depicts the evolution of the geometry through the optimization steps, and Figure 9.11 shows the respective evolution of the CDF. Interestingly, the mean optimization has fewer shape changes than CVaR. Both the 3D view and a plan view of the building are shown in Figure 9.10. Similar to the mean optimization problem here also, tapering is very prominent, as seen in Figure 9.12. As before, this parameter may be the major contributing factor to the reduction in the objective function. The initial top cross-section is circular and then changes to a strongly elliptical cross-section as the optimization progresses. The different steps of this process are shown in Figure 9.12.

The time series and PDFs of the base moments are shown in Figure 9.13 for both problems. Additional samples and time series are computed so that all three comparisons have a similar number of samples. The statistics are recomputed with the same number of samples for the initial and the two final designs. For the CVaR optimization, it can be seen that the PDF is shrunk to reduce the CVaR of the QoI compared to the initial design. Since the PDF is non-symmetric, a mean-plus-standard-deviation type of risk

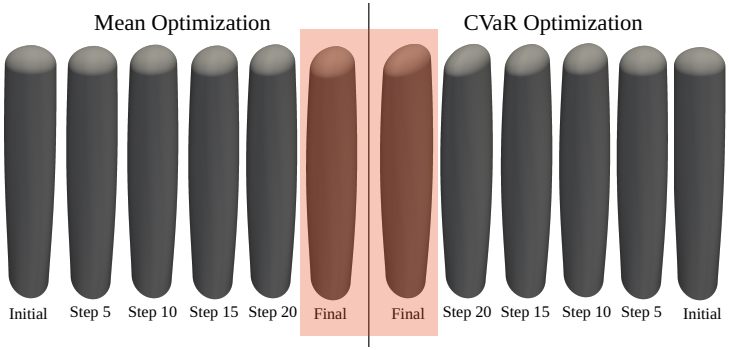

Figure 9.12 : Numerical study 6B: shape change for risk-neutral and risk-averse base moment optimization.

measure will not be ideal for this problem, as seen in Figure 3.4. Hence, it is demonstrated that a non-symmetric measure like CVaR is more optimal for the objective function for these kinds of problems. As in Numerical study 6A, the base moment distribution is improved. The final building designs of both risk-neutral and risk-averse optimization are collected together in Figure 9.10. The shape changes in optimization steps are depicted in Figure 9.14.

9.4.3 Conclusions

The optimization under uncertainty using the developed OUU framework was carried out to design the building under uncertain winds. The adaptive sampling algorithm adopted is effective and reduces the large computational cost required for the OUU. The effectiveness of the adaptive algorithm is demonstrated through the two numerical examples. It was observed that the deterministic optimization (PWD) performs worse than the stochastic designs when the uncertainties in the wind parameters are considered. This emphasizes the need for OUU, especially for problems with the presence of uncertainty, such as the wind flows around a building. The risk-averse and risk-neutral optimization leads to different designs when the number of design parameters is more. Risk-averse optimization is found to be more suitable for the kind of problems where the PDF is non-symmetric.

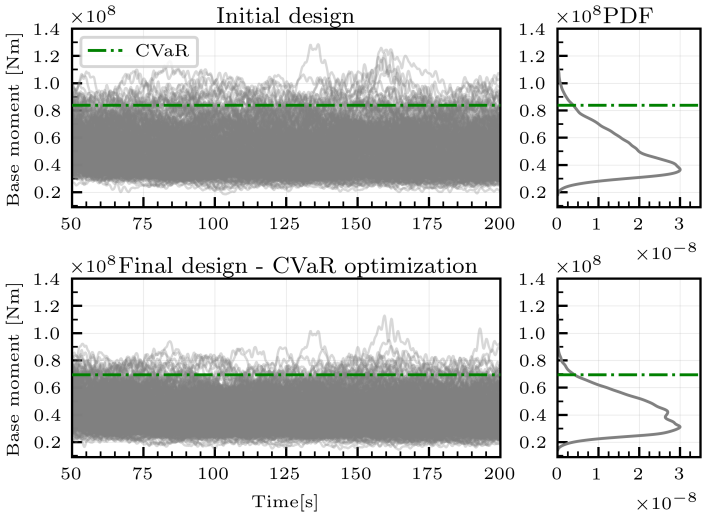

Figure 9.13 : Numerical study 6B: time series and PDFs of the base moment for Problem 2.

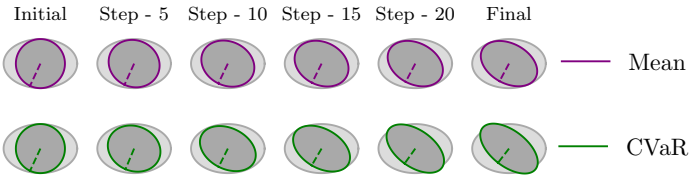

Figure 9.14 : Numerical study 6B: Optimization steps as observed from the top.

CHAPTER 10

CONCLUSION

This thesis presents high-fidelity modeling and simulation for uncertainty quantification in wind effects on structures. A novel risk-averse optimization framework for shape optimization of tall buildings under uncertain wind is also presented in the thesis. Our findings contribute to more efficient and effective methods for UQ and OUU in structural wind engineering. The novel contributions and conclusions are categorized into the following three subsections.

10.1 Contributions

10.1.1 Uncertainty quantification for wind effects on structures

A systematic review of UQ methods for uncertainty quantification is carried out with a clear focus on SCWE application. A comparative study of Monte Carlo, Multi-level Monte Carlo, polynomial chaos, and Neural network in uncertainty quantification for the coupled problem of wind-structure interaction is carried out. The efficacies of these methods for the

benchmark cases are systematically presented and discussed. It is found that for high Reynolds number flows, MC and PC can be used depending on the dimensionality of the problem.

MLMC is found to be effective compared to standard Monte Carlo for coupled problems, and a computational saving by a factor of 8-10 is observed for the numerical example. However, the method is not applicable for high Reynolds flows since the variance reduction is not observed due to the chaotic nature of the flow.

A two-step framework that uses adjoint sensitivity information for uncertainty quantification in polynomial chaos is presented. A two-step surrogate approach that reduces the computational efforts using this is presented for geometric uncertainty in flow problems. The method is found to be effective in creating surrogates at a fraction of the computational cost compared to PC and Monte Carlo methods. However, the method is not applicable for high Reynold flows due to the lack of accurate sensitivities for Navier-Stokes at high Reynolds numbers.

The effect of uncertainties on a benchmark CAARC building B under uncertain wind load is studied using the polynomial chaos approach. PC surrogate is found to be efficient at UQ for SCWE applications. The effects of uncertainties of various parameters for wind effects on structure are quantified using global sensitivity analysis. The load parameters are found to be more sensitive compared to system parameters. Combining this observation with increased uncertainties of the loads, it is critical to quantify uncertainties of the wind in practical applications.

10.1.2 Risk-averse design selection of tall buildings

Conditional value at risk is proposed as a measure for the performance evaluation of a time-varying quantity of interest for a complex phenomenon like wind flow around a tall building. The applicability in wind engineering is demonstrated for benchmark CAARC building under uncertain wind conditions. A significance testing based on the conditional value at risk between structural design options is proposed for the performance-based design selection of structures. The proposed performance measure is demonstrated for serviceability criteria.

10.1.3 Optimization under uncertainty

A novel workflow with risk-averse optimization based on conditional value at risk for optimization under uncertainty is presented. The proposed OUU workflow is applied for the shape optimization of buildings under location-specific uncertain wind loads. It is shown that the risk-averse strategy results in better-performing building shapes, indicating the significance of the proposed OUU workflow.

10.2 Outlook

A few possible extensions for future research that may follow this thesis are described.

The computational efforts required for high-fidelity wind simulation with uncertainty quantification are still large for wide industrial adoption. OUU for day-to-day civil engineering applications is still a long way to go for practicing engineers due to a lack of resources and expertise. This thesis is one of the first works in this direction. Complex and accurate wind models with quantified uncertainties and a risk-averse design philosophy make structures safer and offer additional protection to the society they serve.

A typical practice in wind engineering is to estimate the wind velocity at a location from historical measurements. However, variations in flow patterns resulting from the effects of climate change may result in larger uncertainties in these wind load parameters. This falls in the fourth box in the matrix of knowledge presented in Figure 1.3. Since structures are built for a design life of 50-100 years, quantifying this uncertainty is both critical and challenging.

The roughness length and direction are assumed independent in the OUU example presented in Chapter 9. However, it would be possible to create a copula that takes these correlations into account when data is available on this aspect. Including this correlation will improve inlet wind uncertainty modeling. More complex wind models may also be used for the wind fluctuations in place of the Mann model in Section 3.2, providing a better representation of the physics.

An embedded approach may be used for the CFD for the directionality and optimization in place of the body-fitted mesh creation adopted in this

thesis. This makes it easier to generate and change the geometries and the direction of wind flow.

The finite difference approach used for OUU is prohibitive for large design spaces. Adjoint-based approaches can be solved and used for high Reynolds flow using stabilization methods. This is an interesting development in wind engineering and can also be used for the two-step approach and gradient enhanced surrogate from Chapter 6.

The physics-informed neural network hinted in Chapter 5 has great potential since the NN surrogate can be enhanced by the physics of the problem. This class of methods is promising and has enormous potential in the future. However, specific challenges regarding the performance of training for large degrees of freedom system needs to be tackled for their adaptation to practical problems.

Instead of multi-level Monte Carlo for UQ for wind engineering, Multi-fidelity Monte Carlo is a better alternative for UQ for high Reynolds number flows due to the lower correlation between the levels.

These above-proposed extensions of the current thesis have the potential to open up new opportunities in stochastic computational wind engineering. We hope this thesis provides a foundation for research in uncertainty quantification for structural wind engineering and results in exciting new developments.

List of Figures

List of Tables

List of Algorithms

BIBLIOGRAPHY

[1] *EN 1991-1-4 Actions on structures - Wind*. Vol. 4. 2005. 2011.

[2] Bazilescu, *Tacoma Narrows Bridge Collapse*. [Online; accessed 16-February-2023]. 1940.

[3] J Lowery Lee, *Hyatt Regency walkway collapse*. [Online; accessed 18-February-2023]. 1981.

[4] L Rimmer. Tweet. 2022.

[5] AS Teran, S Agrawal, H Naderian, JK Wong, J Song, O Mercan, PJ Kushner, J Mardukhi, and X Zhang, "Towards a computational workflow for studying the effects of climate change on wind loads on high-rise buildings in urban areas." In: *Atmosphere-Ocean* 60.2 (2022), pp. 124–140. DOI: 10.1080/07055900.2022.2061412.

[6] B Blocken, "50 years of computational wind engineering: Past, present and future." In: *Journal of Wind Engineering and Industrial Aerodynamics* 129 (2014), pp. 69–102. ISSN: 01676105. DOI: 10.1016/j.jweia.2014.03.008.

[7] S Murakami, "Comparison of various turbulence models applied to a bluff body." In: *Journal of Wind Engineering and Industrial Aerodynamics* 46-47 (1993). Proceedings of the 1st International on Computational Wind Engineering, pp. 21–36. ISSN: 0167-6105. DOI: 10.1016/0167-6105(93)90112-2.

[8] S Murakami, A Mochida, and K Hibi, "Three-dimensional numerical simulation of air flow around a cubic model by means of large eddy simulation." In: *Journal of Wind Engineering and Industrial Aerodynamics* 25.3 (1987), pp. 291–305. ISSN: 0167-6105. DOI: 10.1016/0167-6105(87)90023-7.

[9] S Murakami and A Mochida, "3-D numerical simulation of airflow around a cubic model by means of the k-ϵ model." In: *Journal of Wind Engineering and Industrial Aerodynamics* 31.2 (1988), pp. 283–303. ISSN: 0167-6105. DOI: 10.1016/0167-6105(88)90009-8.

[10] S Murakami, "Current status and future trends in computational wind engineering." In: *Journal of Wind Engineering and Industrial Aerodynamics* 67-68 (1997). Computational Wind Engineering, pp. 3–34. ISSN: 0167-6105. DOI: 10.1016/S0167-6105(97)00230-4.

[11] M Nicholls, R Pielke, and R Meroney, "Large eddy simulation of microburst winds flowing around a building." In: *Journal of Wind Engineering and Industrial Aerodynamics* 46-47 (1993). Proceedings of the 1st International on Computational Wind Engineering, pp. 229–237. ISSN: 0167-6105. DOI: 10.1016/0167-6105(93)90288-Y.

[12] M Pentek, A Winterstein (geb. Mini), M Vogl, P Kupás, KU Bletzinger, and R Wüchner, "A multiply-partitioned methodology for fully-coupled computational wind-structure interaction simulation considering the inclusion of arbitrary added mass dampers." en. In: *Journal of Wind Engineering and Industrial Aerodynamics* 177 (2018), pp. 117–135. DOI: 10.1016/j.jweia.2018.03.010.

[13] M Andre, M Pentek, KU Bletzinger, and R Wuechner, "Aeroelastic simulation of the wind-excited torsional vibration of a parabolic trough solar collector." In: *Journal of Wind Engineering and Industrial Aerodynamics* 165 (2017), pp. 67–78. DOI: 10.1016/j.jweia.2017.03.005.

[14] M Andre, M Mier-Torrecilla, and R Wüchner, "Numerical simulation of wind loads on a parabolic trough solar collector using lattice Boltzmann and finite element methods." In: *Journal of Wind Engineering and Industrial Aerodynamics* 146 (2015), pp. 185–194. ISSN: 01676105. DOI: 10.1016/j.jweia.2015.08.010.

[15] F Baetke, H Werner, and H Wengle, "Numerical simulation of turbulent flow over surface-mounted obstacles with sharp edges and corners." In: *Journal of Wind Engineering and Industrial Aerodynamics* 35 (1990), pp. 129–147. ISSN: 0167-6105. DOI: 10.1016/0167-6105(90)90213-V.

[16] GN Lygidakis, SS Sarakinos, and IK Nikolos, "Simulation of the flow over the CAARC standard tall building using different LES turbulence models." In: ASME International Mechanical Engineering Congress and Exposition Volume 1: Advances in Aerospace Technology (Nov. 2016), V001T03A025. DOI: 10.1115/IMECE2016-66399.

[17] A Elshaer, H Aboshosha, G Bitsuamlak, A El Damatty, and A Dagnew, "LES evaluation of wind-induced responses for an isolated and a surrounded tall building." In: *Engineering Structures* 115.May (2016), pp. 179–195. ISSN: 18737323. DOI: 10.1016/j.engstruct.2016.02.026.

[18] PJ Richards, RP Hoxey, BD Connell, and DP Lander, "Wind-tunnel modelling of the Silsoe Cube." In: *Journal of Wind Engineering and Industrial Aerodynamics* 95.9-11 (2007), pp. 1384–1399. ISSN: 01676105. DOI: 10.1016/j.jweia.2007.02.005.

[19] P Richards and S Norris, "LES modelling of unsteady flow around the Silsoe cube." In: *Journal of Wind Engineering and Industrial Aerodynamics* 144 (2015), pp. 70–78. ISSN: 01676105. DOI: 10.1016/j.jweia.2015.03.018.

[20] DA Köse and E Dick, "Prediction of the pressure distribution on a cubical building with implicit LES." In: *Journal of Wind Engineering and Industrial Aerodynamics* 98.10-11 (2010), pp. 628–649. ISSN: 01676105. DOI: 10.1016/j.jweia.2010.06.004.

[21] JD Holmes and TK Tse, "International high-frequency base balance benchmark study." In: *Wind and Structures, An International Journal* 18.4 (2014), pp. 457–471. ISSN: 12266116. DOI: 10.12989/was.2014.18.4.457.

[22] AL Braun and AM Awruch, "Aerodynamic and aeroelastic analyses on the CAARC standard tall building model using numerical simulation." In: *Computers and Structures* 87.9-10 (2009), pp. 564–581. ISSN: 00457949. DOI: 10.1016/j.compstruc.2009.02.002.

[23] AK Dagnew and GT Bitsuamlak, "LES evaluation of wind pressures on a standard tall building with and without a neighboring building." In: *The Fifth International Symosium on Computational - Wind Engineering (CWE2010) Chapel Hill, North Carolina, USA* 2007 (2010).

[24] MF Huang, IW Lau, CM Chan, KC Kwok, and G Li, "A hybrid RANS and kinematic simulation of wind load effects on full-scale tall buildings." In: *Journal of Wind Engineering and Industrial Aerodynamics* 99.11 (2011), pp. 1126–1138. ISSN: 01676105. DOI: 10.1016/j.jweia.2011.09.003.

[25] W Hu, KK Choi, and H Cho, "Reliability-based design optimization of wind turbine blades for fatigue life under dynamic wind load uncertainty." In: *Structural and Multidisciplinary Optimization* 54.4 (2016), pp. 953–970. ISSN: 16151488. DOI: 10.1007/s00158-016-1462-x.

[26] M Lackner, a.L. Rogers, and J Manwell, "Uncertainty analysis in wind resource assessment and wind energy production estimation." In: *45th AIAA Aerospace Sciences Meeting and Exhibit* (2007), pp. 1–16. DOI: doi:10.2514/6.2007-1222.

[27] LM Van Den Bos, B Sanderse, L Blonk, WA Bierbooms, and GJ Van Bussel, "Efficient ultimate load estimation for offshore wind turbines using interpolating surrogate models." In: *Journal of Physics: Conference Series* 1037.6 (2018). ISSN: 17426596. DOI: 10.1088/1742-6596/1037/6/062017.

[28] B Blocken and T Stathopoulos, "CFD simulation of pedestrian-level wind conditions around buildings: Past achievements and prospects." In: *Journal of Wind Engineering and Industrial Aerodynamics* 121 (2013), pp. 138–145. ISSN: 0167-6105. DOI: 10.1016/j.jweia.2013.08.008.

[29] B Blocken, W Janssen, and T van Hooff, "CFD simulation for pedestrian wind comfort and wind safety in urban areas: General decision framework and case study for the Eindhoven University campus." In: *Environmental Modelling Software* 30 (2012), pp. 15–34. ISSN: 1364-8152. DOI: 10.1016/j.envsoft.2011.11.009.

[30] E García-Portugués, RM Crujeiras, and W González-Manteiga, "Exploring wind direction and SO_2 concentration by circular–linear density estimation." In: *Stochastic Environmental Research and Risk Assessment* 27.5 (2013), pp. 1055–1067.

[31] C García-Sánchez, DA Philips, and C Gorlé, "Quantifying inflow uncertainties for CFD simulations of the flow in downtown Oklahoma City." In: *Building and Environment* 78.2014 (2014), pp. 118–129. ISSN: 03601323. DOI: 10.1016/j.buildenv.2014.04.013.

[32] A Kareem, "Numerical simulation of wind effects: A probabilistic perspective." In: *Journal of Wind Engineering and Industrial Aerodynamics* 96.10-11 (2008), pp. 1472–1497. ISSN: 01676105. DOI: 10.1016/j.jweia.2008.02.048.

[33] W Dettmer and D Perić, "A computational framework for fluid–structure interaction: Finite element formulation and applications." In: *Computer Methods in Applied Mechanics and Engineering* 195.41 (2006). John H. Argyris Memorial Issue. Part II, pp. 5754–5779. ISSN: 0045-7825. DOI: 10.1016/j.cma.2005.10.019.

[34] M Ángel Fernández and M Moubachir, "A Newton method using exact jacobians for solving fluid–structure coupling." In: *Computers Structures* 83.2 (2005). Advances in Analysis of Fluid Structure Interaction, pp. 127–142. ISSN: 0045-7949. DOI: 10.1016/j.compstruc.2004.04.021.

[35] RC Smith, *Uncertainty quantification: theory, implementation, and applications*. USA: Society for Industrial and Applied Mathematics, 2013. ISBN: 161197321X.

[36] F Montomoli, M Carnevale, M Massini, A D'Ammaro, and S Salvadori, *Uncertainty quantification in computational fluid dynamics and aircraft engines*. Apr. 2015. ISBN: 978-3319146805. DOI: 10.1007/978-3-319-92943-9.

[37] J Mueller and S Siltanen, eds., *Linear and nonlinear inverse problems with practical applications*. English. Vol. 10. Computational Science amp; Engineering. United States: Society for Industrial and Applied Mathematics, 2012. ISBN: 978-1-61197-233-7. DOI: 10.1137/1.9781611972344.

[38] DG Cacuci, *Sensitivity and uncertainty analysis, Volume 1: Theory*. Boca Raton, FL: Chapman Hall/CRC, 2003.

[39] A Paudel, S Gupta, M Thapa, SB Mulani, and RW Walters, "Higher-order Taylor series expansion for uncertainty quantification with efficient local sensitivity." In: *Aerospace Science and Technology* 126 (2022), p. 107574. ISSN: 1270-9638. DOI: 10.1016/j.ast.2022.107574.

[40] A Chaudhuri and S Chakraborty, "Reliability of linear structures with parameter uncertainty under non-stationary earthquake." In: *Structural Safety* 28.3 (2006), pp. 231–246. ISSN: 0167-4730. DOI: 10.1016/j.strusafe.2005.07.001.

[41] N Metropolis and S Ulam, "The Monte Carlo Method." In: *Journal of the American Statistical Association* 44.247 (1949), pp. 335–341. ISSN: 01621459.

[42] RE Caflisch, "Monte Carlo and quasi-Monte Carlo methods." In: *Acta Numerica* 7 (1998), 1–49. DOI: 10.1017/S0962492900002804.

[43] WL Loh, "On Latin Hypercube Sampling." In: *The Annals of Statistics* 24.5 (1996), pp. 2058–2080. ISSN: 00905364.

[44] MB Giles, "Multilevel Monte Carlo Path Simulation." In: *Oper. Res.* 56.3 (2008), pp. 607–617. ISSN: 0030-364X. DOI: 10.1287/opre.1070.0496.

[45] MB Giles, "Multilevel Monte Carlo methods." In: *Acta Numer.* 24. May (2015), pp. 259–328. ISSN: 14740508 . DOI: 10.1017/S096249291500001X.

[46] S Gupta and C Manohar, "An improved response surface method for the determination of failure probability and importance measures." In: *Structural Safety* 26.2 (2004), pp. 123–139. ISSN: 0167-4730. DOI: 10.1016/S0167-4730(03)00021-3.

[47] PDS Roger G. Ghanem, *Stochastic Finite Elements: A Spectral Approach*. Springer New York, NY, 1991.

[48] N Wiener, "The Homogeneous Chaos." In: *American Journal of Mathematics* 60.4 (1938), pp. 897–936. ISSN: 00029327, 10806377.

[49] K Cliffe, M Giles, R Scheichl, and A Teckentrup, "Multilevel Monte Carlo methods and applications to elliptic PDEs with random coefficients." In: *Computing and Visualization in Science* 14 (Dec. 2010). DOI: 10.1007/s00791-011-0160-x.

[50] K Sepahvand, S Marburg, and HJ Hardtke, "Uncertainty quantification in stochastic systems using polynomial chaos expansion." In: *International Journal of Applied Mechanics* 02.02 (2010), pp. 305–353. DOI: 10.1142/S1758825110000524.

[51] A Kodakkal, P Jagtap, and V Matsagar, "Chapter 16 - Stochastic response of primary–secondary coupled systems under uncertain ground excitation using generalized polynomial chaos method." In: *Handbook of Probabilistic Models*. Ed. by P Samui, D Tien Bui, S Chakraborty, and RC Deo. Butterworth-Heinemann, 2020, pp. 383–435. ISBN: 978-0-12-816514-0
. DOI: 10.1016/B978-0-12-816514-0.00016-3.

[52] B Sudret, "Global sensitivity analysis using polynomial chaos expansions." In: *Reliability Engineering System Safety* 93.7 (2008). Bayesian Networks in Dependability, pp. 964–979. ISSN: 0951-8320. DOI: 10.1016/j.ress.2007.04.002.

[53] G Blatman and B Sudret, "Adaptive sparse polynomial chaos expansion based on least angle regression." In: *Journal of Computational Physics* 230 (Mar. 2011), pp. 2345–2367. DOI: 10.1016/j.jcp.2010.12.021.

[54] A Kodakkal, SK Saha, K Sepahvand, VA Matsagar, F Duddeck, and S Marburg, "Uncertainties in dynamic response of buildings with non-linear base-isolators." In: *Engineering Structures* 197 (2019), p. 109423. ISSN: 0141-0296. DOI: 10.1016/j.engstruct.2019.109423.

[55] M Raissi, P Perdikaris, and G Karniadakis, "Physics-informed neural networks: A deep learning framework for solving forward and inverse problems involving nonlinear partial differential equations." In: *Journal of Computational Physics* 378 (2019), pp. 686–707. ISSN: 0021-9991. DOI: 10.1016/j.jcp.2018.10.045.

[56] A Kodakkal, RE Meethal, B Obst, and R Wüchner, "A Finite Element Method-Informed Neural Network For Uncertainty Quantification." In: *14th WCCM-ECCOMAS Congress 2020*. Vol. 800. 2021.

[57] M Breuer, G De Nayer, M Münsch, T Gallinger, and R Wüchner, "Fluid–structure interaction using a partitioned semi-implicit predictor–corrector coupling scheme for the application of large-eddy simulation." In: *Journal of Fluids and Structures* 29 (2012), pp. 107–

130. ISSN: 0889-9746. DOI: 10.1016/j.jfluidstructs.2011.09.003.

[58] A Kareem and A Tamura, *Advanced structural wind engineering*. Springer, 2015.

[59] JC Kaimal and JJ Finnigan, *Atmospheric boundary layer flows: their structure and measurement*. Oxford university press, 1994.

[60] J Mann, "Wind field simulation." In: *Probabilistic engineering mechanics* 13.4 (1998), pp. 269–282.

[61] CW Kent, "Surface roughness parameters in cities: Improvements and implications for windspeed estimation." PhD thesis. University of Reading, 2018.

[62] CW Kent, K Lee, HC Ward, JW Hong, J Hong, D Gatey, and S Grimmond, "Aerodynamic roughness variation with vegetation: Analysis in a suburban neighbourhood and a city park." In: *Urban ecosystems* 21.2 (2018), pp. 227–243.

[63] J JCSS, "Probabilistic model code." In: *Joint Committee on Structural Safety* (2001).

[64] JA Carnicero, MC Ausín, and MP Wiper, "Non-parametric copulas for circular–linear and circular–circular data: an application to wind directions." In: *Stochastic environmental research and risk assessment* 27.8 (2013), pp. 1991–2002.

[65] M Sklar, "Fonctions de repartition a n dimensions et leurs marges." In: *Publ. inst. statist. univ. Paris* 8 (1959), pp. 229–231.

[66] RB Nelsen, *An introduction to copulas*. Springer Science Business Media, 2007.

[67] A Kodakkal, B Keith, U Khristenko, A Apostolatos, KU Bletzinger, B Wohlmuth, and R Wüchner, "Risk-averse design of tall buildings for uncertain wind conditions." In: *Computer Methods in Applied Mechanics and Engineering* (2022), p. 115371. ISSN: 0045-7825. DOI: 10.1016/j.cma.2022.115371.

[68] GR Tabor and M Baba-Ahmadi, "Inlet conditions for large eddy simulation: A review." In: *Computers Fluids* 39.4 (2010), pp. 553–567.

[69] B Sanderse, S Van der Pijl, and B Koren, "Review of computational fluid dynamics for wind turbine wake aerodynamics." In: *Wind energy* 14.7 (2011), pp. 799–819.

[70] X Wu, "Inflow turbulence generation methods." In: *Annual Review of Fluid Mechanics* 49 (2017), pp. 23–49.

[71] B Keith, U Khristenko, and B Wohlmuth, "Learning the structure of wind: A data-driven nonlocal turbulence model for the atmospheric boundary layer." In: *Physics of Fluids* 33.9 (2021), p. 095110.

[72] J Mann, "The spatial structure of neutral atmospheric surface-layer turbulence." In: *Journal of fluid mechanics* 273 (1994), pp. 141–168.

[73] IEC, "Wind turbines–Part 1: Design requirements." In: *International Electrotechnical Commission, Geneva* (61400-1:2005).

[74] A Michalski, PD Kermel, E Haug, R Löhner, R Wüchner, and KU Bletzinger, "Validation of the computational fluid-structure interaction simulation at real-scale tests of a flexible 29m umbrella in natural wind flow." In: *Journal of Wind Engineering and Industrial Aerodynamics* 99.4 (2011), pp. 400–413. ISSN: 01676105. DOI: 10.1016/j.jweia.2010.12.010.

[75] L Dong, WH Lio, and E Simley, "On turbulence models and lidar measurements for wind turbine control." In: *Wind Energy Science* 6.6 (2021), pp. 1491–1500.

[76] C Gumbert, P Newman, and G Hou, "Effect of random geometric uncertainty on the computational design of a 3D flexible wing." In: *20th AIAA Applied Aerodynamics Conference*. DOI: 10.2514/6.2002-2806.

[77] AB Liel, CB Haselton, GG Deierlein, and JW Baker, "Incorporating modeling uncertainties in the assessment of seismic collapse risk of buildings." In: *Structural Safety* 31.2 (2009). Risk Acceptance and Risk Communication, pp. 197–211. ISSN: 0167-4730. DOI: 10.1016/j.strusafe.2008.06.002.

[78] J Cheng, C Cai, R cheng Xiao, and S Chen, "Flutter reliability analysis of suspension bridges." In: *Journal of Wind Engineering and Industrial Aerodynamics* 93.10 (2005), pp. 757–775. ISSN: 0167-6105. DOI: 10.1016/j.jweia.2005.08.003.

[79] S Chakraborty and SS Dey, "Stochastic finite element simulation of random structure on uncertain foundation under random loading." In: *International Journal of Mechanical Sciences* 38.11 (1996), pp. 1209–1218. ISSN: 0020-7403. DOI: 10.1016/0020-7403(96)00005-7.

[80] F Sadek and E Simiu, "Peak Non-Gaussian Wind Effects for Database-Assisted Low-Rise Building Design." In: *Journal of Engineering Mechanics* 128.5 (2002), pp. 530–539. DOI: 10.1061/(ASCE)0733-9399(2002)128:5(530).

[81] RT Rockafellar, S Uryasev, et al., "Optimization of conditional value-at-risk." In: *Journal of risk* 2 (2000), pp. 21–42.

[82] RT Rockafellar and JO Royset, "Engineering decisions under risk averseness." In: *ASCE-ASME Journal of Risk and Uncertainty in Engineering Systems, Part A: Civil Engineering* 1.2 (2015), p. 04015003.

[83] DP Kouri and TM Surowiec, "Risk-averse PDE-constrained optimization using the conditional value-at-risk." In: *SIAM Journal on Optimization* 26.1 (2016), pp. 365–396.

[84] DP Kouri and A Shapiro, "Optimization of PDEs with Uncertain Inputs." In: *Frontiers in PDE-Constrained Optimization*. Springer, 2018, pp. 41–81.

[85] M Hairer and JC Mattingly, "Ergodicity of the 2D Navier–Stokes equations with degenerate stochastic forcing." In: *Annals of Mathematics* (2006), pp. 993–1032.

[86] AG Davenport, "Past, present and future of wind engineering." In: *Journal of Wind Engineering and Industrial Aerodynamics* 90.12-15 (2002), pp. 1371–1380. ISSN: 01676105. DOI: 10.1016/S0167-6105(02)00383-5.

[87] PA Irwin, "Wind engineering challenges of the new generation of super-tall buildings." In: *Journal of Wind Engineering and Industrial Aerodynamics* 97.7-8 (2009), pp. 328–334. ISSN: 01676105. DOI: 10.1016/j.jweia.2009.05.001.

[88] S Bahga, *Absolute towers mississauga. South-west view.* [Online; accessed December 30, 2021]. 2018.

[89] MRD Ortiz), *F F Tower Panama.* [Online; accessed March 03, 2022]. 2013.

[90] A Guichard, *30 St. Mary Axe tower*. [Online; accessed March 03, 2022]. 2010.

[91] A Elshaer, G Bitsuamlak, and A El Damatty, "Enhancing wind performance of tall buildings using corner aerodynamic optimization." In: *Engineering Structures* 136.April (2017), pp. 133–148. ISSN: 18737323. DOI: 10.1016/j.engstruct.2017.01.019.

[92] F Beiser, B Keith, S Urbainczyk, and B Wohlmuth, "Adaptive sampling strategies for risk-averse stochastic optimization with constraints." In: *arXiv preprint arXiv:2012.03844* (2020).

[93] RT Rockafellar and JO Royset, "On buffered failure probability in design and optimization of structures." In: *Reliability engineering system safety* 95.5 (2010), pp. 499–510.

[94] RT Rockafellar and S Uryasev, "The fundamental risk quadrangle in risk management, optimization and statistical estimation." In: *Surveys in Operations Research and Management Science* 18.1-2 (2013), pp. 33–53.

[95] S Wright and B Recht, *Optimization for Data Analysis*. Cambridge University Press, 2022.

[96] RH Byrd, GM Chin, J Nocedal, and Y Wu, "Sample size selection in optimization methods for machine learning." In: *Mathematical programming* 134.1 (2012), pp. 127–155.

[97] R Bollapragada, R Byrd, and J Nocedal, "Adaptive sampling strategies for stochastic optimization." In: *SIAM Journal on Optimization* 28.4 (2018), pp. 3312–3343.

[98] Y Xie, R Bollapragada, R Byrd, and J Nocedal, "Constrained and composite optimization via adaptive sampling methods." In: *arXiv preprint arXiv:2012.15411* (2020).

[99] DJ Lea, MR Allen, and TW Haine, "Sensitivity analysis of the climate of a chaotic system." In: *Tellus A: Dynamic Meteorology and Oceanography* 52.5 (2000), pp. 523–532.

[100] M Schäfer, S Turek, F Durst, E Krause, and R Rannacher, "Benchmark computations of laminar flow around a cylinder." In: *Flow Simulation with High-Performance Computers II: DFG Priority Research Programme Results 1993–1995*. Ed. by EH Hirschel. Wiesbaden: Vieweg+Teubner Verlag, 1996, pp. 547–566. ISBN: 978-3-322-89849-4. DOI: 10.1007/978-3-322-89849-4_39.

[101] A Kodakkal, R Wüchner, and KU Bletzinger, "Multilevel Monte Carlo method for stochastic analysis of fluid-structure interaction." In: *PAMM* 18.1 (2018), e201800148. DOI: 10.1002/pamm.201800148.

[102] MA Bouhlel and J Martins, "Gradient-enhanced kriging for high-dimensional problems." In: *Engineering with Computers* 35 (Jan. 2019). DOI: 10.1007/s00366-018-0590-x.

[103] J Laurenceau and P Sagaut, "Building efficient response surfaces of aerodynamic functions with kriging and cokriging." In: *Aiaa Journal - AIAA J* 46 (Feb. 2008), pp. 498–507. DOI: 10.2514/1.32308.

[104] J Rijpkema, L Etman, and A Schoofs, "Use of design sensitivity information in response surface and kriging metamodels." In: *Optimization and Engineering* 2 (Dec. 2001), pp. 469–484. DOI: 10.1023/A:1016098623669.

[105] Y Li, M Anitescu, O Roderick, and F Hickernell, "Orthogonal Bases For Polynomial Regression With Derivative Information In Uncertainty Quantification." In: *International Journal for Uncertainty Quantification* 1.4 (2011), pp. 297–320. ISSN: 2152-5080.

[106] L Guo, A Narayan, and T Zhou, "A gradient enhanced l1-minimization for sparse approximation of polynomial chaos expansions." In: *Journal of Computational Physics* 367 (2018), pp. 49–64. ISSN: 0021-9991. DOI: 10.1016/j.jcp.2018.04.026.

[107] "Guide for the verification and validation of computational fluid dynamics simulations (AIAA G-077-1998(2002))." In: *Guide: Guide for the Verification and Validation of Computational Fluid Dynamics Simulations (AIAA G-077-1998(2002))*. DOI: 10.2514/4.472855.001. eprint: https://arc.aiaa.org/doi/pdf/10.2514/4.472855.001.

[108] PJ Roache, *Verification and validation in computational science and engineering*. Vol. 895. Hermosa Albuquerque, NM, 1998.

[109] A Abodonya, "Verification methodology for computational wind engineering prediction of wind loads on structures." Dissertation. München: Technische Universität München, 2020.

[110] WL Oberkampf, TG Trucano, and C Hirsch, "Verification, validation, and predictive capability in computational engineering and physics." In: *Appl. Mech. Rev.* 57.5 (2004), pp. 345–384.

[111] WL Oberkampf and CJ Roy, *Verification and validation in scientific computing*. Cambridge University Press, 2010. DOI: 10.1017/CBO9780511760396.

[112] F Stern, R Wilson, H Coleman, and E Paterson, "Comprehensive approach to verification and validation of CFD simulations—Part 1: Methodology and procedures." In: *Journal of Fluids Engineering* 123 (Dec. 2001), p. 792. DOI: 10.1115/1.1412235.

[113] WL Oberkampf and MF Barone, "Measures of agreement between computation and experiment: validation metrics." In: *Journal of Computational Physics* 217.1 (2006), pp. 5–36.

[114] M Barone, W Oberkampf, and F Blottner, "Validation case study: prediction of compressible turbulent mixing layer growth rate." In: *AIAA journal* 44.7 (2006), pp. 1488–1497.

[115] S Ferson, WL Oberkampf, and L Ginzburg, "Model validation and predictive capability for the thermal challenge problem." In: *Computer Methods in Applied Mechanics and Engineering* 197.29-32 (2008), pp. 2408–2430.

[116] R Schöbi and B Sudret, "Propagation of uncertainties modelled by parametric p-boxes using sparse polynomial chaos expansions." In: *12th Int. Conf. on Applications of Statistics and Probability in Civil Engineering (ICASP12)*. 2015.

[117] T Oden, R Moser, and O Ghattas, "Computer predictions with quantified uncertainty, part I." In: *SIAM News* 43.9 (2010), pp. 1–3.

[118] J Cotela-Dalmau, R Rossi, and E Oñate, "Applications of turbulence modeling in civil engineering." PhD thesis. 2016. DOI: 10.1016/j.cma.2016.11.020.

[119] E Obasaju, "Measurement of forces and base overturning moments on the CAARC tall building model in a simulated atmospheric boundary layer." In: *Journal of Wind Engineering and Industrial Aerodynamics - J WIND ENG IND AERODYN* 40 (June 1992), pp. 103–126. DOI: 10.1016/0167-6105(92)90361-D.

[120] S Huang, Q Li, and S Xu, "Numerical evaluation of wind effects on a tall steel building by CFD." In: *Journal of Constructional Steel Research* 63 (May 2007), pp. 612–627. DOI: 10.1016/j.jcsr.2006.06.033.

[121] mpentek, *ParOptBeam*. 2023.

[122] R Rahgozar, Z Mahmoudzadeh, M Malekinejad, and P Rahgozar, "Dynamic analysis of combined system of framed tube and shear walls by Galerkin method using B-spline functions." In: *The Structural Design of Tall and Special Buildings* 24.8 (2015), pp. 591–606. DOI: 10.1002/tal.1201.

[123] D Boggs and C Petersen, "Acceleration indexes for human comfort in tall buildings—peak or RMS?" In: (Jan. 1995).

[124] P Dadvand, R Rossi, and E Oñate, "An object-oriented environment for developing finite element codes for multi-disciplinary applications." In: *Archives of Computational Methods in Engineering* 17.3 (2010), pp. 253–297. ISSN: 11343060. DOI: 10.1007/s11831-010-9045-2.

[125] P Dadvand, R Rossi, M Gil, X Martorell, J Cotela, E Juanpere, SR Idelsohn, and E Oñate, "Migration of a generic multi-physics framework to HPC environments." In: *Computers and Fluids* 80.1 (2013), pp. 301–309. ISSN: 00457930. DOI: 10.1016/j.compfluid.2012.02.004.

[126] C Dapogny, C Dobrzynski, P Frey, and A Froehly, "MMG version 5.6.0." In: 5.6.0.1 (2021). DOI: https://github.com/MmgTools/mmg.

[127] RM Badia, J Conejero, C Diaz, J Ejarque, D Lezzi, F Lordan, C Ramon-Cortes, and R Sirvent, "{COMP} Superscalar, an interoperable programming framework." In: *SoftwareX* 3–4 (2015). DOI: 10.1016/j.softx.2015.10.004.

[128] F Lordan, E Tejedor, J Ejarque, R Rafanell, J Álvarez, F Marozzo, D Lezzi, R Sirvent, D Talia, and RM Badia, "ServiceSs: An Interoperable Programming Framework for the Cloud." In: *Journal of Grid Computing* 12.1 (Sept. 2013), pp. 67–91. DOI: 10.1007/s10723-013-9272-5.

[129] E Tejedor, Y Becerra, G Alomar, A Queralt, RM Badia, J Torres, T Cortes, and J Labarta, "PyCOMPSs: Parallel computational workflows in Python." In: *International Journal of High Performance Computing Applications* 31.1 (2017), pp. 66–82. DOI: 10.1177/1094342015594678.

Bisherige Titel der Schriftenreihe

Band	Titel
1	Frank Koschnick, *Geometrische Lockingeffekte bei Finiten Elementen und ein allgemeines Konzept zu ihrer Vermeidung*, 2004.
2	Natalia Camprubi, *Design and Analysis in Shape Optimization of Shells*, 2004.
3	Bernhard Thomee, *Physikalisch nichtlineare Berechnung von Stahlfaserbetonkonstruktionen*, 2005.
4	Fernaß Daoud, *Formoptimierung von Freiformschalen - Mathematische Algorithmen und Filtertechniken*, 2005.
5	Manfred Bischoff, *Models and Finite Elements for Thin-walled Structures*, 2005.
6	Alexander Hörmann, *Ermittlung optimierter Stabwerkmodelle auf Basis des Kraftflusses als Anwendung plattformunabhängiger Prozesskopplung*, 2006.
7	Roland Wüchner, *Mechanik und Numerik der Formfindung und Fluid-Struktur-Interaktion von Membrantragwerken*, 2006.
8	Florian Jurecka, *Robust Design Optimization Based on Metamodeling Techniques*, 2007.
9	Johannes Linhard, *Numerisch-mechanische Betrachtung des Entwurfsprozesses von Membrantragwerken*, 2009.

Band Titel

10 Alexander Kupzok, *Modeling the Interaction of Wind and Membrane Structures by Numerical Simulation*, 2009.

11 Bin Yang, *Modified Particle Swarm Optimizers and their Application to Robust Design and Structural Optimization*, 2009.

12 Michael Fleischer, *Absicherung der virtuellen Prozesskette für Folgeoperationen in der Umformtechnik*, 2009.

13 Amphon Jrusjrungkiat, *Nonlinear Analysis of Pneumatic Membranes - From Subgrid to Interface*, 2009.

14 Alexander Michalski, *Simulation leichter Flächentragwerke in einer numerisch generierten atmosphärischen Grenzschicht*, 2010.

15 Matthias Firl, *Optimal Shape Design of Shell Structures*, 2010.

16 Thomas Gallinger, *Effiziente Algorithmen zur partitionierten Lösung stark gekoppelter Probleme der Fluid-Struktur-Wechselwirkung*, 2011.

17 Josef Kiendl, *Isogeometric Analysis and Shape Optimal Design of Shell Structures*, 2011.

18 Joseph Jordan, *Effiziente Simulation großer Mauerwerksstrukturen mit diskreten Rissmodellen*, 2011.

19 Albrecht von Boetticher, *Flexible Hangmurenbarrieren: Eine numerische Modellierung des Tragwerks, der Hangmure und der Fluid-Struktur-Interaktion*, 2012.

20 Robert Schmidt, *Trimming, Mapping, and Optimization in Isogeometric Analysis of Shell Structures*, 2013.

21 Michael Fischer, *Finite Element Based Simulation, Design and Control of Piezoelectric and Lightweight Smart Structures*, 2013.

22 Falko Hartmut Dieringer, *Numerical Methods for the Design and Analysis for Tensile Structures*, 2014.

Band Titel

23 Rupert Fisch, *Code Verification of Partitioned FSI Environments for Lightweight Structures*, 2014.

24 Stefan Sicklinger, *Stabilized Co-Simulation of Coupled Problems Including Fields and Signals*, 2014.

25 Madjid Hojjat, *Node-based parametrization for shape optimal design*, 2015.

26 Ute Israel, *Optimierung in der Fluid-Struktur-Interaktion - Sensitivitätsanalyse für die Formoptimierung auf Grundlage des partitionierten Verfahrens*, 2015.

27 Electra Stavropoulou, *Sensitivity analysis and regularization for shape optimization of coupled problems*, 2015.

28 Daniel Markus, *Numerical and Experimental Modeling for Shape Optimization of Offshore Structures*, 2015.

29 Pablo Suárez, *Design Process for the Shape Optimization of Pressurized Bulkheads as Components of Aircraft Structures*, 2015.

30 Armin Widhammer, *Variation of Reference Strategy - Generation of Optimized Cutting Patterns for Textile Fabrics*, 2015.

31 Helmut Masching, *Parameter Free Optimization of Shape Adaptive Shell Structures*, 2016.

32 Hao Zhang, *A General Approach for Solving Inverse Problems in Geophysical Systems by Applying Finite Element Method and Metamodel Techniques*, 2016.

33 Tianyang Wang, *Development of Co-Simulation Environment and Mapping Algorithms*, 2016.

34 Michael Breitenberger, *CAD-integrated Design and Analysis of Shell Structures*, 2016.

Band Titel

35 Önay Can, *Functional Adaptation with Hyperkinematics using Natural Element Method: Application for Articular Cartilage*, 2016.

36 Benedikt Philipp, *Methodological Treatment of Non-linear Structural Behavior in the Design, Analysis and Verification of Lightweight Structures*, 2017.

37 Michael Andre, *Aeroelastic Modeling and Simulation for the Assessment of Wind Effects on a Parabolic Trough Solar Collector*, 2018.

38 Andreas Apostolatos, *Isogeometric Analysis of Thin-Walled Structures on Multipatch Surfaces in Fluid-Structure Interaction*, 2018.

39 Altuğ Emiroğlu, *Multiphysics Simulation and CAD-Integrated Shape Optimization in Fluid-Structure Interaction*, 2019.

40 Mehran Saeedi, *Multi-Fidelity Aeroelastic Analysis of Flexible Membrane Wind Turbine Blades*, 2017.

41 Reza Najian Asl, *Shape optimization and sensitivity analysis of fluids, structures, and their interaction using Vertex Morphing Parametrization*, 2019.

42 Ahmed Abodonya, *Verification Methodology for Computational Wind Engineering Prediction of Wind Loads on Structures*, 2020.

43 Anna Maria Bauer, *CAD-integrated Isogeometric Analysis and Design of Lightweight Structures*, 2020.

44 Andreas Winterstein, *Modeling and Simulation of Wind Structure Interaction of Slender Civil Engineering Structures Including Vibration Systems*, 2020.

45 Franz-Josef Ertl, *Vertex Morphing for Constrained Shape Optimization of Three-dimensional Solid Structures*, 2020.

Band Titel

46 Daniel Baumgärtner, *On the Grid-based Shape Optimization of Structures with Internal Flow and the Feedback of Shape Changes into a CAD Model*, 2020.

47 Mohamed Khalil, *Combining Physics-based models and machine learning for an Enhanced Structural Health Monitoring*,2021.

48 Long Chen, *Gradient Descent Akin Method*, 2021.

49 Aditya Ghantasala, *Coupling Procedures for Fluid-Fluid and Fluid-Structure Interaction Problems Based on Domain Decomposition Methods*, 2021.

50 Ann-Kathrin Goldbach, *The Cad-Integrated Design Cycle for Structural Membranes*, 2022.

51 Iñigo Pablo López Canalejo„ *A Finite-Element Transonic Potential Flow Solver with an Embedded Wake Approach for Aircraft Conceptual Design*, 2022.

52 Mayu Sakuma, *An Application of Multi-Fidelity Uncertainty Quantification for Computational Wind Engineering*, 2022.

53 Suneth Warnakulasuriya, *Development of methods for Finite Element-based sensitivity analysis and goal-directed mesh refinement using the adjoint approach for steady and transient flows*, 2022.

54 Klaus Bernd Sautter, *Modeling and Simulation of Flexible Protective Structures by Coupling Particle and Finite Element Methods*, 2022.

55 Efthymios Papoutsis, *On the incorporation of industrial constraints in node-based optimization for car body design*, 2023.

56 Thomas Josef Oberbichler, *A modular and efficient implementation of isogeometric analysis for the interactive CAD-integrated design of lightweight structures*, 2023.

Band Titel

57 Tobias Christoph Teschemacher, *CAD-integrated constitutive modelling, analysis, and design of masonry structures*, 2023.

58 Shahrokh Shayegan, *Enhanced Algorithms for Fluid-Structure Interaction Simulations – Accurate Temporal Discretization and Robust Convergence Acceleration*, 2023.

59 Ihar Antonau, *Enhanced computational design methods for large industrial node-based shape optimization problems*, 2023.

60 Rishith Ellath Meethal, *Hybrid modelling and simulation approaches for the solution of forward and inverse problems in engineering by combining finite element methods and neural networks*, 2023.

61 Máté Péntek, *Method Development for the Numerical Wind Tunnel in Applied Structural Engineering*, 2023.